UNIVERSITY OF OKLAHOMA

GRADUATE COLLEGE

MOLECULAR BEAM EPITAXY OF INAS, GASB, ALSB STRUCTURES FOR INTERBAND CASCADE DEVICES

A DISSERTATION

SUBMITTED TO THE GRADUATE FACULTY

in partial fulfillment of the requirements for the

Degree of

DOCTOR OF PHILOSOPHY

By

HAO YE
Norman, Oklahoma
2016

MOLECULAR BEAM EPITAXY OF INAS, GASB, ALSB STRUCTURES FOR INTERBAND CASCADE DEVICES

A DISSERTATION APPROVED FOR THE
SCHOOL OF ELECTRICAL AND COMPUTER ENGINEERING

BY

____
Dr. Rui Q. Yang, Chair

____
Dr. Michael B. Santos, Co-Chair

____
Dr. Sheena Q. Murphy

____
Dr. Jessica E. Ruyle

____
Dr. Matthew B. Johnson

____
Dr. Zhisheng Shi

© Copyright by HAO YE 2016
All Rights Reserved.

Acknowledgements

I would like to thank the financial support during my graduate career from the National Science Foundation (ECCS-1002202 and ECCS-1202318), the DoE EPSCoR program (DE- SC0004523), AFOSR (FA9550-12-1-0260 and FA9550-15-1-0067), and C-SPIN, the Oklahoma/Arkansas MRSEC (NSF Award Number DMR-0520550).

I am especially grateful to my advisor, Prof. Rui Q. Yang, for offering me the opportunity to conduct research that suited my personality. His enthusiasm, dedication, vision, as well as his trust, inspired and motivated me to go the extra mile in every aspect. His guidance has made this journey thoughtful and rewarding. I am also grateful to my co-advisor, Prof. Michael B. Santos, for guiding me throughout my research with unconditional support. I will remember and be forever grateful for his patience and insight in our long discussions. I thank Prof. Matthew Johnson, who has equipped me with the material characterization skills and experimental senses. My research has been built on successful collaborations among the three of them.

I would like to thank the other committee members: Prof. Zhisheng Shi, Prof. Jessica Ruyle, and Prof. Sheena Murphy for taking the time to review my dissertation and providing constructive comments.

I owe my deepest gratitude to Dr. Lu Li, who has taught me MBE growth, given suggestions on my research, and supported me selflessly. Special thanks go to Dr. Joel Keay, who made me believe that I was never alone and could achieve anything I wanted. I am grateful for the chance to work with both of them. They have taught me the true patience, diligence, and unselfishness of life.

I would like to thank the present and former members of the III-V MBE group, especially Tetsuya, Mukul, Chomani, Sangeetha, Kaushini. They have shared the experience in MBE growth and maintenance in the lab and stood side by side with me in good and bad times. I also want to extend heartfelt thanks to present and former members of the quantum device laboratory, especially Zhaobing, Bobby, Yuchao, Zuowei, Lihua, Hossein, Rassel, and Lin, for giving me feedback from device performances, sharing innovative ideas, and being supportive research partners. Many thanks to Ernest and Preston for teaching me AFM and SEM. Together with my other colleagues, thank you all for being there for me and making the impossible possible.

Thanks to my after-work friends for making my life colorful and enjoyable. Special thanks to Yuchao and Zhaojing, who have motivated and accompanied me for marathon runs.

Last but not least, I would like to thank my parents for allowing their only child to be so far away from them, and having always been there for me with their unconditional love. Thanks to my beloved husband, Fan. His love and support have empowered me and made this work possible.

Table of Contents

Acknowledgements iv

List of Tables ix

List of Figure x

Abstract xvii

Chapter 1 Introduction 1

1.1 Interband Cascade Lasers 2

1.2 Interband Cascade Photodetector and Photovoltaic Structures with InAs/GaSb Superlattices 7

1.2.1 Operating Principle of Interband Cascade Photodetector Device 7

1.2.2 Operating Principle of Interband Cascade Photovoltaic Device 10

1.3 Dissertation Introduction 13

Chapter 2 Molecular Beam Epitaxy Growth 17

2.1 Introduction 17

2.2 The Control of Growth Conditions 21

2.2.1 Substrate Temperature Measurement 21

2.2.2 Flux Control 26

2.2.3 Growth Rate Calibration 31

2.3 MBE Facilities 37

Chapter 3 Material Characterization 39

3.1 X-ray Diffraction 39
3.1.1 Diffraction Condition and Reciprocal Lattice 39
3.1.2 Crystalline Quality and X-ray Scans 43
3.1.3 Experimental Procedures in XRD Scans 48
3.1.4 Strain Calculation 51
3.1.5 XRD Measurement of IC Structures 53
3.2 Atomic Force Microscopy 64
3.2.1 Principle and Microscope Architecture 64
3.2.2 AFM of Surface Morphology 68
3.3 Scanning Electron Microscopy 72
3.3.1 Principle and Microscope Architecture 72
3.3.2 SEM of Surface Morphology 75
3.3.3 SEM of Devices after Fabrication 78
Chapter 4 MBE Growth of InAs-Based Interband Cascade Laser Structures 86
4.1 InAs (001) Homoepitaxy 86
4.1.1 n-type Doping of InAs Layer with Si and GaTe 87
4.1.2 Surface Roughness of Homoepitaxial InAs 93
4.1.3 Oval Hillock Defect on Homoepitaxial InAs Layers 98
4.2 MBE Growth and Material Characterization of InAs-based IC Laser Structures 104
4.3 Device Performance 109
Chapter 5 MBE Growth of ICPD and ICPV Structures 115
5.1 Structures with InAs/GaSb Superlattices 115

5.2 Device Performance of the Two and Three-stage ICPV Devices 120
5.3 MBE Growth of InAs/GaSb Superlattice Absorbers with Different Interface Arrangements 124
5.3.1 Interface of InAs/GaSb Superlattice.. 124
5.3.2 ICPD Structures with Different Interface Arrangements 126
5.3.3 Material Characterization 129
5.3.4 Device Characterization 132
Chapter 6 Conclusion and Future Work 140
References 146
Appendix: Publication List... 159

List of Tables

Table 2.1: Growth parameters of 27 growths in 2013 in the GEN II. 35

Table 3.1: X-ray diffraction data for two ω-2θ scans of R089 at the area of high and low defect density. 48

Table 3.2: X-ray diffraction data of R120 for five ω-2θ scans of R120 at ϕ*, ϕ*+90°, ϕ*+180°, ϕ*+270° (ϕ-90°), and ϕ* with different alignments. 55

Table 3.3: X-ray diffraction data for ω-2θ scans of R089 at different regions, ϕ angles, and alignments. 57

Table 3.4: Matthews-Blakeslee critical thickness of mismatched layers. The mismatch is deduced by assuming a satellite peak close to the substrate peak is the zero order peak in R088. 63

Table 4.1: Growth conditions and fitting parameters of spectral reflectance measurement in InAs epitaxial layers. 92

Table 4.2: Parameters of wafer structures and pulsed performance of broad-area lasers. 112

Table 4.3: Surface morphology as assessed by the DIC microscopy and superlattice parameters as determined by XRD. 114

Table 5.1: XRD information from the experimental data, including the deduced superlattice period, the period error compared with the designed period of 62 Å, the perpendicular mismatch of the average superlattice lattice constant in the growth direction compared with the GaSb substrate, the intensity and the FWHM of the first satellite peak on the left (-1st), zero order satellite peak in the center (0th), the first satellite peak on the right (1st), and the substrate peak (sub). The intensity of all peaks is normalized to their substrate peak [162]. 132

List of Figure

Figure 1.1: Illustration of the interband cascade process [17].. 2

Figure 1.2: Calculated band-edge diagram of one cascade stage. The layer thickness (in units of Å) of each layer in one IC stage beginning at the barrier separating the electron injector and the active region is 26, 22, 29, 20, 12, 32, 12, 48, 21, 43, 12, 33, 12, 27, 12, 24, 12, and 23. The structure was designed for an InAs-based ICL to lase at a wavelength of 4.6 μm at room temperature [20]. 3

Figure 1.3: General schematic for an ICPD device under zero bias. Each stage is composed of a superlattice absorber sandwiched between electron and hole barriers. E_e and E_h denote the energy for electron (thick line) and hole (thin line) minibands, respectively. The energy difference (E_e - E_h) corresponds to the bandgap (E_g) of the SL. Arrows represent the flow direction of electrons and holes, which are generated in the SL absorber and recombine at the electron and hole barrier interfaces (dash lines) through interband tunneling.................................... 8

Figure 1.4: General schematic for an ICPV device under a forward bias. Each stage is composed of a superlattice absorber sandwiched between electron and hole barriers. E_e and E_h denote the energy for electron (thick line) and hole (thin line) minibands, respectively. The energy difference (E_e - E_h) corresponds to the bandgap (E_g) of the SL. Arrows represent the flow direction of electrons and holes, which are generated in the SL absorber and recombine at the electron and hole barrier interfaces (dash lines) through interband tunneling.................................. 12

Figure 2.1: Schematic diagram of a typical MBE growth chamber with a vertical design. 18

Figure 2.2: (a) Schematics of an electron beam striking the wafer along [-110] and being reflected and diffracted onto a RHEED screen. The wafer has an orientation flat (major flat) in (0-1-1) plane following the SEMI-EJ standard. (b) 3× RHEED pattern during the GaSb growth, where the incident beam is along the [-110] azimuths.. 20

Figure 2.3: The RHEED patterns at the [-110] azimuths on a GaSb surface at a thermocouple temperature of (a) 470°C (3×) and (b) 330°C (5×). 24

Figure 2.4: Temperature as a function of time during growth of ICPD. The dashed line represents thermocouple data and the solid line represents pyrometer temperature with an emissivity of 0.65 and a calibration factor of 0.8288 by BASF EX11984 pyrometer. The inset shows the data around 25000 second marked by the rectangular. 25

Figure 2.5: The temperature, output power percentage, and the BFM reading during shutter cycling in a single zone Al cell with a cone shape crucible. (a) A measurement that has a normal PID control. (b) A measurement where power control is shifted to a manual mode output a few seconds before the shutter opens and returns back to PID control when the shutter closes....................................... 28

Figure 2.6: The temperature, output power percentage, and the BFM reading during shutter cycling for a sumo crucible in a dual-filament cell. (a) PID values were 50, 57.75, and 9.62 for the tip, and were 100, 19.75, and 3.2 for the base zone. (b) Default PID values were 250, 75, and 5 for both tip and base zones. 29

Figure 2.7: RHEED oscillations of during GaAs growth. 32

Figure 2.8: (a) Gallium growth rates (left side, squares) and beam equivalent pressures (right side, circles) versus base cell temperatures in the GENxplor. (b) Gallium growth rates versus beam equivalent pressures. 33

Figure 2.9: (a) Two indium cells' growth rates (left side, squares) and beam equivalent pressures (right side, circles) versus base cell temperatures in the GENxplor. (b) Indium growth rates versus beam equivalent pressures for two cells. 33

Figure 2.10: Cell temperatures for 27 growths in 2013 in the GEN II. Black squares are period errors calculated from x-ray diffraction measurement, suggesting thickness differences between the designed structures and the grown structures. 34

Figure 3.1: Diffraction of a wave off atoms in a crystalline material obeys Bragg's law, $n\lambda=2d_{hkl}\sin\theta$. d_{hkl} is the spacing between diffracting planes, θ is the incident angle, n is an integer, and λ is the wavelength of the x-ray. 40

Figure 3.2: X-rays are incident on the sample and scatter back with wavevectors k_{in} and k_{out}, respectively. G is a reciprocal lattice vector. 40

Figure 3.3: The scattering vector and Ewald sphere in the reciprocal lattice. The points are reciprocal lattice points of the crystal, and each point (hkl) in reciprocal space represents a plane (hkl) in real space. Reciprocal lattice points that lie on the surface of the Ewald sphere satisfy the diffraction condition. 43

Figure 3.4: Material characterization of IC lasers structures R087 and R088 by XRD and AFM. (a) X-ray diffraction data for ω-2θ scans around the 004 reflection of R087 (lower) and R088 (upper). The inset shows the scan data near the substrate peak. (b) The schematic laser sequence of R087 and R088. (c), (d) AFM images taken from the surfaces of R087 and R088 over a 5 μm × 5 μm area, respectively. 45

Figure 3.5: Material characterization of different areas on IC laser structure R089 by XRD and DIC microscopy. (a) X-ray diffraction data for ω-2θ scans around the 004 reflection of R089 at areas of high (lower) and low (upper) defect density. The inset shows the scan data near the substrate peak. (b) A schematic of the quarter of the 2-inch wafer, where the dashed line indicates the boundary between high and low defect areas. The long rectangular spots indicate the regions intersecting the x-ray beam for the two scans. Numbers in parentheses are the coordinate on the wafer. (c), (d) DIC microscopy images taken from the area of the low and high defect density on the surface of R089, respectively. 47

Figure 3.6: A schematic diagram of the XRD unit in (a) a side view and (b) a plan view. 49

Figure 3.7: Change of the epilayer unit cell with relaxation in (001) wafers................. 53

Figure 3.8: (a) X-ray diffraction data for R120 for ω-2θ scans around the 004 reflection at ϕ* and (b) the scan comparison of scans at ϕ*, ϕ*+90°, ϕ*+180°, and ϕ*+270° (ϕ-90°). 55

Figure 3.9: X-ray diffraction data for ω-2θ scans around the 004 reflection at ϕ*, ϕ*+90°, ϕ*+180° for a high defect region of R089, and at ϕ* in two alignments for a low defect region. 57

Figure 3.10: X-ray diffraction data (upper) and a corresponding simulation (lower) for an ω-2θ scan around the 004 reflection of R088. The inset shows the FWHMs of satellite peaks around the substrate peak..................... 59

Figure 3.11: Simplified schematics of an AFM system [106]..................... 65

Figure 3.12: Interatomic force verses distance (tip to sample) curve. The operating regimes of the different scanning modes are shown. 67

Figure 3.13: AFM scans on ICPD structure R120 over a 2 μm × 2 μm area in (a) height trace, (b) height retrace, (c) amplitude, (d) phase, and (e) ZSensor channels. 69

Figure 3.14: (a) AFM scans on ICPD structure R120 over a 2 μm × 2 μm area in height trace. The red line indicates the position of the line profile shown in (b). (b) The profile of 20 pixels crossing ~50 atomic steps. 70

Figure 3.15: AFM scans on ICPD structure R120 over a 10 μm ×10 μm area in height trace. 71

Figure 3.16: Different types of signal originate from different volumes of interaction [111]. 73

Figure 3.17: Detailed morphology of the same defects in an InAs homoepitaxial layer in images using: (a) the in-lens detector with 5 keV accelerating voltage, (b) the in-lens detector with 10 keV accelerating voltage, (c) the BSD detector with 10 keV accelerating voltage. Insets to (a) and (c) are the same top-left defects in a higher magnification..................... 76

Figure 3.18: (a) DIC microscopy image of IC laser structure R099. (b-e) BSD SEM images of defects appearing in image (a) (labeled squares) taken at 10 keV......... 77

Figure 3.19: (a-c) SEM images of InAs homoepitaxial layers over a 2 μm ×2 μm area taken by the BSD with a 10 keV accelerating voltage at a working distance of 4.2 mm; (d-f) AFM images of the same samples. 78

Figure 3.20: Schematics of a broad-area laser with the SiO_2 insulation layer and Ti/Au contact layer..................... 80

Figure 3.21: SEM images of the laser facets on different lasers. Full size view images of front and back side facets were taken under the same magnification. The front side facet images which were taken in cross-sectional view at 90° and at a ~3 mm working distance. The back side facet images were taken at a long working distance of 15 mm and a tilted angle of 50° to 60°. 82

Figure 3.22: SEM and EDS analyses on IC laser R096BA-2 of the bonding-delamination problem. (a, b) SEM images of devices with failed bonding craters and delaminated contact layers. Dashed squares indicate the positions at which the images were taken. (c, d) SEM images of delaminated contact layers using the BSD and SE detectors. (e) The EDS line scans on the laser ridge. (f) The line scan sum spectrum and the weight percent of the elements in the line scan. (g) The EDS spots on the backside of the delaminated contact layers. (h) Representative point scan spectra and the weight percent of the elements. 84

Figure 4.1: Electrical concentration at 300 K versus Si cell temperature for of InAs layer grown on GaAs substrate.. 89

Figure 4.2: Electrical concentration versus GaTe cell temperature based on Hall measurement of 0.5 μm InAs layers grown on GaAs substrates at 0.44 ML/s. Black circles represent layers grown after a 550°C outgassing, while red squares represent layers grown after a 630°C outgassing. 90

Figure 4.3: DIC microscopy images of InAs epitaxial layers on InAs (001) substrates, (a) T889, (b) T890, (c) T899, (d) T900 with higher and lower defect area. 91

Figure 4.4: The relation between the surface defect density and growth conditions for InAs homoepitaxial layers. A larger circle size shows that the corresponding InAs layer has a smaller defect density. The gray area indicates a transition region that separates regions where 2×4 or 4×2 reconstructions were observed during growth. The transition region was experimentally determined by decreasing the As flux for a brief time during some of the layer growths. Based on the RHEED patterns, all the structures were grown in the As-stabilized (2×4) region except T10 [92]. 95

Figure 4.5: SEM images (a, b, c) captured by an annular backscattered electron detector and 2 μm × 2 μm AFM area scans (d, e, f) of the homoepitaxial structures grown at different conditions. The color scale is 2 nm in the AFM images. The substrate temperature (T), As_2/In flux ratio (V/III), RMS surface roughness (RMS) and peak to valley height (P-V) are as follows: (a, d) Structure T2, T= 405˚C, V/III=11:1, RMS = 0.22 nm, and P-V = ~1.3 nm; (b, e) Structure T6, T= 427˚C, V/III=14:1, RMS = 0.19 nm, and P-V = ~0.8 nm; (c, f) Structure T11 grown at 0.22 ML/s, T= 400˚C, V/III=8:1, RMS = 0.13 nm, and P-V = ~0.8 nm [92]................................ 96

Figure 4.6: Detailed morphology of the same defect in images by SEM and AFM. (a ,b, c) are images of the same defect at the same scale; (a) and (b) are plan-view SEM images captured by an annular backscattered electron detector and the in-lens secondary electron detector, respectively. (c) is a 3 μm × 3 μm AFM scan of the defect. The dashed white line indicates the position of the line profile shown in (d).

(d) is the profile crossing the center of the pit which shows that the oval defect rises about 25 nm from the surface and a pit depth of ≥ 250 nm (tip geometry limited). (e) is a vertical height corrected oblique-view SEM image of the defect's cross section obtained by FIB milling at 200 pA with 20 nm steps. A dark feature 540 nm from the surface of the hillock is present in 5 sequential frames and highlighted by a white circle [92]. 100

Figure 4.7: SEM and TEM images of an oval hillock defect and the specimen prepared by a focused ion beam (FIB) unit. (a) and (b) are plan-view SEM images captured by an annular backscattered electron detector and the in-lens SE detector, respectively. (c) The tilted SEM image showing removal of the TEM thin section with the micromanipulator. (d) The tilted SEM image showing the placement of the TEM thin section onto a specialized TEM grid. (e) High resolution TEM image of the oval hillock. 102

Figure 4.8: (a) 2 μm × 2 μm and (b) 10 μm × 10 μm AFM images of the InAs substrate after oxide desorption. 103

Figure 4.9: Structure of a long-wavelength IC laser, R110. 106

Figure 4.10: A DIC microscopy image of R110. 107

Figure 4.11: AFM images for the IC laser structure in (a) 2 μm × 2 μm and (b) 10 μm × 10 μm area scans. 107

Figure 4.12: (Top) Experimental XRD curve from an ω-2θ scan around the InAs (004) reflection for the IC laser structure. (Bottom) Corresponding simulated XRD curve calculated for the designed structure. The inset shows the data around the substrate. 108

Figure 4.13: Current-voltage-light characteristics for a 150-μm-wide device in cw operation. The insets are its cw lasing spectra at heat-sink temperatures of 80 K to 97 K, and emission spectra at 80 K with several injection currents before threshold [26]. 109

Figure 4.14: Light-current curve for a broad-area IC laser in pulsed mode at temperatures of 80 K to 130 K. The arrows point to threshold currents where spectra were taken. The inset shows the pulsed spectra at several temperatures [26]. 110

Figure 4.15: Calculated optical modal profiles of IC lasers without (thin lines) and with intermediate superlattice cladding layers (thick lines) [20]. 111

Figure 4.16: Experimental XRD curves from an ω-2θ scan around the InAs (004) reflection for the IC laser structures R125, R143, R136, and R144 (from top to bottom). The inset shows the scans data around the substrate. 114

Figure 5.1: Experimental XRD scans from an ω-2θ scan around the GaSb (004) reflection for IC laser structures (Y010D, Y011D, and Y012D). Corresponding

simulated XRD scan calculated for the designed structure (bottom curve). The inset shows the scans data near the substrate peak. 117

Figure 5.2: (a) The two-stage ICPV structure R103, grown on a GaSb (001) substrate. (b) X-ray diffraction data (black) and a corresponding simulation (red) for an ω-2θ scan around the 004 reflection. The inset shows the experimental data near the substrate peak and the zero order peak [58]. 118

Figure 5.3: AFM image taken from the surface of the two-stage ICPV structure over (a) a 2 μm × 2 μm and (b) a 5 μm × 5 μm areas. 119

Figure 5.4: Quantum efficiency for two- and three-stage ICPV devices measured at T=300 K and 350 K. The inset shows the bandgap corresponding to a cutoff wavelength at different temperatures for both devices [58]. 121

Figure 5.5: Current density versus voltage at T=300 K and 340 K for both two- and three-stage devices. An IC laser with an emission wavelength of 4.3 μm was used for illumination [58]. 122

Figure 5.6: Short circuit current density J_{sc} and open circuit voltage V_{oc} for two- and three-stage devices at different temperatures. An IC laser with the same output power was used for these measurements [58]. 123

Figure 5.7: Schematic diagram of a two-stage ICPD [162]. 127

Figure 5.8: InAs/GaSb superlattice structure (one period) with different interface arrangements. 128

Figure 5.9: Shutter sequences of structure I-1. 128

Figure 5.10: DIC microscopy images of wafer (a) I-2 and (b) I-1. AFM images taken of the surface of (c) I-2 (RMS=2 Å) and (d) I-1 (RMS=1 Å). The lateral scale is 2 μm ×2 μm and the gray scale is 3 nm [162]. 130

Figure 5.11: X-ray diffraction data for wafers I-2 (top) and I-1 (middle) and a corresponding simulation (bottom) of an ω-2θ scan around the 004 reflection with the interfacial InSb layers. The scans are offset for clarity. The inset shows the experimental data near the substrate peak and the zero order peak [162]. 131

Figure 5.12: Dark current density versus voltage for detectors made from I-2 (dash lines) and I-1 (solid lines) at temperatures from 78 K up to 200 K. The device sizes for I-2 and I-1 are 1×1 mm^2 and 0.4×0.4 mm^2, respectively [162]. 133

Figure 5.13: Responsivity spectra for detectors made from wafers I-2 (dash line) and I-1 (solid line) at temperatures from 78 K to 220 K. The device sizes for I-2 and I-1 are 0.4×0.4 mm^2. The inset table shows the reverse bias applied to the device during the measurement. The inset figure shows the spectra of I-2 (red line) and I-1 (blue line) at 250 K [162]. 135

Figure 5.14: Detectivity D^* for detectors made from I-2 (dash lines) and I-1 (solid lines) at temperatures from 78 K up to 220 K. The device sizes for I-2 and I-1 are 0.4×0.4 mm^2. The inset table shows the reverse bias applied to the device during the measurement [162]. 137

Abstract

The interband cascade (IC) family of devices has been extended beyond mid-infrared lasers to include photovoltaic (PV) and photodetector (PD) devices. These devices utilize the transition between conduction and valence bands for photon emission or absorption in the infrared region. The cascade structure recycles electrons to generate or collect multiple photons per electron. Epitaxial growths of the device structures are challenging because they consist of hundreds of quantum wells and require atomic layer precision in thickness control. Molecular beam epitaxy (MBE) was used to grow these structures with InAs, GaSb, AlSb, and their alloys on InAs or GaSb substrates.

IC laser structures with InAs plasmon cladding layers were grown on InAs substrates for wavelengths greater than 3 μm. To provide a smooth initial surface for the cascade region, the optimal conditions for growth of homoepitaxial InAs layers were investigated over a wide range of substrate temperatures and As_2/In flux ratios at a growth rate of 0.66 monolayer/s (ML/s). Material quality was investigated using differential interference contrast microscopy, scanning electron microscopy, and atomic force microscopy. The geometry of oval hillock defects on the InAs layers suggested that these defects originated at the substrate surface. The InAs-based IC lasers had emission wavelengths out to 11 μm, which is the longest wavelength among interband lasers based on III–V materials. By introducing intermediate superlattice (SL) cladding layers to enhance optical confinement and reduce internal absorption loss, the first continuous wave operation of InAs-based IC lasers at room temperature was demonstrated. The threshold current density of 247 A/cm^2 for emission near 4.6 μm is

the lowest ever reported among semiconductor mid-infrared lasers at similar wavelengths.

ICPV and ICPD devices were developed based on the architecture of IC lasers. They both consist of multiple discrete InAs/GaSb SL absorbers sandwiched between electron and hole barriers. ICPV devices can be used in thermophotovoltaic systems that convert radiant energy from a heat source into electricity. Strain-balanced InAs/GaSb SL structures were achieved by adjusting the group-V overpressure during MBE growth. Two- and three-stage ICPV devices operated at room temperature with substantial open-circuit voltages at a cutoff wavelength of 5.3 μm, the longest ever reported for room-temperature PV devices.

The interfaces of InAs/GaSb SLs were studied with the goal of improving the PDs designed for the long-wavelength infrared region. Two ICPD structures with different SL interfaces were grown by MBE, one with a ~1.2 ML-thick InSb layer inserted intentionally only at the GaSb-on-InAs interfaces and another with a ~0.6 ML-thick InSb layer inserted at both InAs-on-GaSb and GaSb-on-InAs interfaces. The material quality of the PD structures was similar according to differential interference contrast microscopy, atomic force microscopy, and x-ray diffraction measurements. The device performances were not substantially different with a detectivity of 3.7×10^{10} Jones for 78 K at 8 μm and both operated up to 250K. This good performance implies that the interface quality was reasonably controlled for both interface arrangements. The arrangement of dividing a thick continuous InSb layer at the GaSb-on-InAs interface into thinner InSb layers at both interfaces can be used to achieve strain balance in SL detectors for even longer wavelengths.

Chapter 1 Introduction

III-V semiconductor materials are composed of one element from column III (mainly Al, Ga, In) and one from column V (mainly N, P, As, Sb) of the periodic table. Except the nitride family of materials, common III-V semiconductor materials usually crystallize in zinc-blende lattice, which consists of two interpenetrating face-centered-cubic lattices, one having a group-III element atom and the other a group-V element atom. Among them, InAs, GaSb, AlSb, and their related alloys have lattice constants near 6.1 Angstrom (Å), so they are also called "6.1 Å" materials. Since they are nearly lattice-matched, these materials can be grown on GaSb and InAs substrates by molecular beam epitaxy (MBE) to form high-quality heterostructures with a low density of defects and dislocations. Similar to the widely used GaAs and InP, InAs and GaSb have a direct-bandgap and a light electron mass, which made them unique and useful for optoelectronics and high-speed electronics. Additionally, InAs and GaSb have narrower bandgaps and lighter electron masses than GaAs and InP and therefore have the advantages over the conventional GaAs- or InP- based devices for high-frequency operation with low power consumption and for mid-infrared optoelectronic devices [1].

6.1 Å materials have a broad range of band gaps from 0.36 to 2.2 eV at room temperature as well as different band-edge relationships including type-I, type-II, and type-II broken-gap. These properties fulfill the needs of band structure engineering for sophisticated devices, which include high electron mobility transistors [2], resonant tunneling diodes [3, 4], infrared lasers [5, 6], and infrared photodetectors [7] to name a few. Moreover, 6.1 Å materials have also been used in some novel research topics

recently; for example, the two-dimensional topological insulator state in InAs/GaSb quantum wells [8, 9]. This dissertation focuses on interband cascade structures including interband cascade lasers (ICLs), photovoltaic (PV) devices, and photodetector (PD) devices.

1.1 Interband Cascade Lasers

The concept of the interband cascade laser was initially proposed in 1994 [6, 10] and was first demonstrated in 1997 [11]. Since then, remarkable achievements have been made by several groups [12-18] in the infrared (IR) region, including mid-wave IR (MWIR at 3–5 μm) and long-wave IR (LWIR at 8–12 μm). The ICL works in the infrared range where numerous "fingerprint" spectral lines exist, and thus can be used to sense gas molecules such as methane, carbon dioxide, carbon monoxide, hydrochloric acid, and formaldehyde. A single-mode distributed feedback (DFB) ICL has been deployed for methane detection on the NASA Mars Curiosity Mission [19]. Other important applications include industrial process control, environmental monitoring, clinical breath analysis, and free-space optical communications.

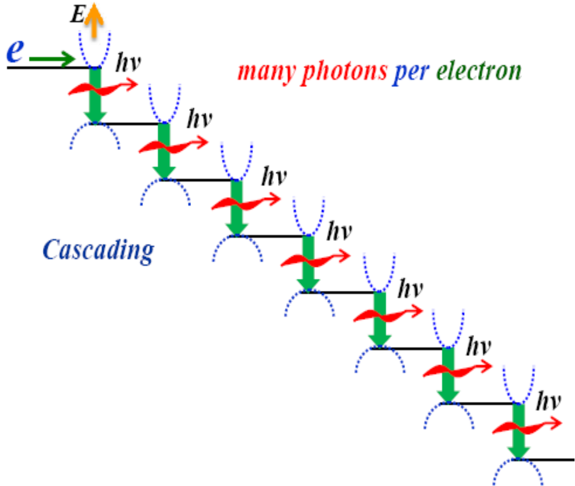

Figure 1.1: Illustration of the interband cascade process [17].

ICLs utilize a cascade structure where multiple stages are connected in series, as shown in Figure 1.1. In each stage, electrons emit photons by transitioning from the conduction band to the valence band. The transitioned electrons are then transported to the next stage via interband tunneling facilitated by a type-II broken-gap alignment. Therefore, each electron is recycled in multiple stages and generates multiple photons. An example of a detailed layer sequence for one cascade stage is illustrated in Figure 1.2 by the calculated band-edge diagram [20]. The active region is composed of InAs/InGaSb quantum wells; the hole and electron injector regions consist of GaSb/AlSb and InAs/AlSb quantum wells, respectively. IC lasers and their emission wavelengths can be tailored in a wide wavelength range by changing the layer thicknesses, in principle from the mid-IR (as short as 2.5 μm) to the far-IR [17].

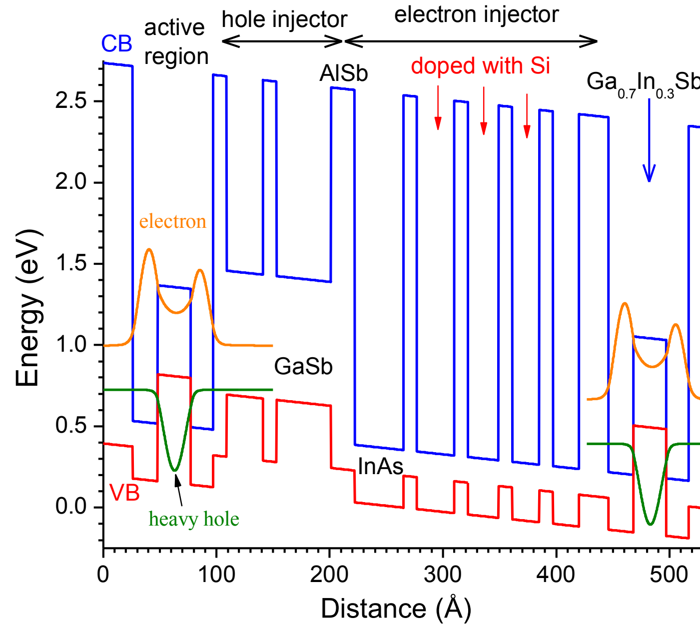

Figure 1.2: Calculated band-edge diagram of one cascade stage. The layer thickness (in units of Å) of each layer in one IC stage beginning at the barrier separating the electron injector and the active region is 26, 22, 29, 20, 12, 32, 12, 48, 21, 43, 12, 33, 12, 27, 12, 24, 12, and 23. The structure was designed for an InAs-based ICL to lase at a wavelength of 4.6 μm at room temperature [20].

Compared to the conventional diode laser, the ICL has a high quantum efficiency, *i.e.* the number of photons generated per electron is larger than one. To generate the same number of photons, the required current is much less than for a conventional laser diode. However, the threshold voltage is higher, since it is proportional to the number of the stages when the stages are connected in series. Because the ICL trades higher threshold voltage for lower threshold current, the ohmic power loss (I^2R_s) is reduced and less power is wasted on the parasitic resistance (R_s). Consequently, the cascade structure improves the power conversion efficiency, especially when operating in a high-power situation.

There are also attractive advantages compared with quantum cascade lasers (QCLs), which produce light via intersubband transitions within the conduction band. Fast phonon scattering is inherent to intersubband transitions and occurs at a much faster rate (>3 orders of magnitude) than the non-radiative transition of interband devices. Therefore, the threshold current density has to be significantly higher than in ICLs to establish a population inversion. With an optimized structure, ICLs were reported to have a minimum input power almost two orders of magnitude lower than that of an ordinary QCL [21]. Therefore, IC lasers will be a better option for compact, portable, low cost, and low-power-budget applications.

This work was carried out on InAs-based ICLs, which are grown on InAs substrates with highly n-type doped InAs layers as plasmon outer cladding layers in the waveguide. The plasmon waveguide structure was first implemented in QCLs by Sirtori *et al*. [22, 23] and was first applied to ICLs by our group at the University of Oklahoma [24]. There are several advantages of using the InAs cladding layer rather

than the InAs/AlSb SL cladding layers in the GaSb-based ICL structures. First, a highly doped InAs layer has a higher thermal conductivity (~0.3 instead of ~0.03 W/cm·K). This improves the thermal dissipation of ICLs, especially in longer wavelength cases where a thicker cladding layer is required to compensate for the longer optical wave decay length. Second, the MBE growth of highly-doped InAs cladding layers is less demanding compared with the InAs/AlSb SL where strain balancing is essential. Third, InAs plasmon waveguide structures can suppress the wave penetration into the cladding region and thus reduce the optical loss, since the refractive index of InAs can be much lower than that of the cascade core region (3.0 verses 3.4) [25]. With the use of a plasmon waveguide structure, ICLs have been successfully demonstrated with emission wavelengths as long as 11 μm, which is the longest wavelength among interband lasers based on III–V semiconductor materials [26]. The growth details of the long wavelength InAs-based ICL will be discussed in Section 4.2.

Recently, an InAs/AlSb SL was introduced as an intermediate cladding layer to replace a portion of the undoped-InAs separate confinement layers [20]. Since the refractive index of an InAs/AlSb SL is smaller than that of the center active region, more of the optical wave is squeezed into the center active region. This leads to a lower optical loss, a lower threshold current density, and consequently a higher device performance [20]. The thickness of the InAs/AlSb SL is about 1 μm, which is still thinner than the cladding in GaSb-based ICLs (2~5 μm in the bottom cladding). Therefore, InAs-based ICLs still have a better thermal dissipation. The implementation resulted in a high device performance even with an inferior material

quality. The threshold current density was as low as 247 A/cm^2 at 300 K for emission near 4.6 μm, which is the lowest ever reported among semiconductor mid-infrared lasers at similar wavelengths [20]. More details are presented in Section 4.3.

1.2 Interband Cascade Photodetector and Photovoltaic Structures with InAs/GaSb Superlattices

A superlattice (SL) is a periodic heterostructure of two or more semiconductor materials. By creating a periodic atomic chain analogous to natural crystals, minibands are formed in the conduction and valence bands. The bands of the SL can be tailored by adjusting the periodicity in the growth direction. Smith and Mailhiot [7] proposed using a type-II InAs/GaInSb SL for infrared photodetection in 1987. The InAs/GaSb interface has a type-II broken-gap alignment, where the conduction band of InAs is located about 0.15 eV below the valence band of GaSb. The misaligned offset provides the type-II SL a great flexibility in bandgap engineering. Operating wavelengths covering 3 μm to 32 μm have been reported [27, 28]. If the period of the SL is made large enough so that the quantization effects are weakened, the bandgap can be adjusted to zero while making a transition from a narrow gap semiconductor to a semi-metal [29]. Therefore, InAs/GaSb SLs are attractive for use in the detection and emission of infrared light.

1.2.1 Operating Principle of Interband Cascade Photodetector Device

Since the proposal of using an InAs/GaSb SL in an infrared photodetector, great strides have been made to improve the materials quality and develop device designs to compete with mercury cadmium telluride (MCT) infrared detectors. The type-II SL detectors are predicted to have superior performance to the MCT detectors, especially in the long wavelength (>10 μm) [30-32]. To pursue the best device performance, considerable effort has been devoted to various type-II SL device structures, such as the interband cascade photodetector (ICPD) [33], W-structure photodiode [34], nBn detector [35, 36], p-π-m-n photodiode [37], and complementary

barrier infrared detector (CBIRD) [38]. This work studies the ICPDs (or interband cascade infrared photodetectors (ICIPs)), which is unique compared to the others mentioned above due to the use of a discrete absorber structure [33, 39-41].

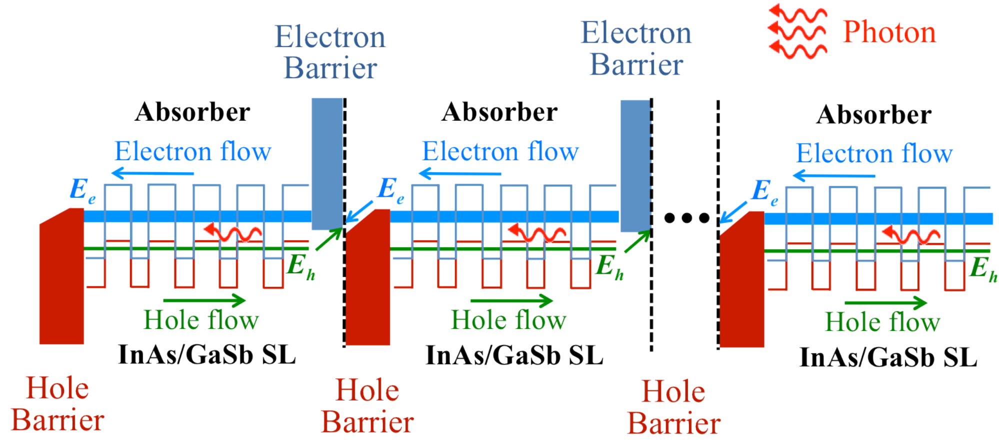

Figure 1.3: General schematic for an ICPD device under zero bias. Each stage is composed of a superlattice absorber sandwiched between electron and hole barriers. E_e and E_h denote the energy for electron (thick line) and hole (thin line) minibands, respectively. The energy difference (E_e - E_h) corresponds to the bandgap (E_g) of the SL. Arrows represent the flow direction of electrons and holes, which are generated in the SL absorber and recombine at the electron and hole barrier interfaces (dash lines) through interband tunneling.

ICPD devices were developed based on the architecture of ICLs. Instead of using the conventional *p-n* junction structure, ICPDs employ multiple discrete absorbers connected in series with wide-bandgap unipolar barriers. The unipolar barriers impose a preferred carrier flow direction and form recombination interfaces facilitated by type-II alignment, as shown in Figure 1.3 for an ICPD device. The electron barrier is designed with AlSb/GaSb quantum wells, and the hole barrier is a series of InSb/AlInSb quantum wells. Each absorber is composed of an InAs/GaSb SL with a bandgap that is tailored by adjusting the thickness of constituent InAs and GaSb layers. The type-II broken-gap alignment between the InAs and GaSb layers is depicted in Figure 1.3 for the absorber regions. The electron (thick blue line) and hole

(thin green line) minbands with energies of E_e and E_h are also shown. The energy difference (E_e - E_h) is the bandgap (E_g) of the SL.

In each absorber, photons are absorbed to generate electron and hole pairs. The photo-generated carriers flow away from their namesake barriers (electron barrier or hole barrier) to the adjacent stage and recombine through interband tunneling at the interface of the electron and hole barriers. The electron (hole) transport path and recombination interface are shown in Figure 1.3 with blue (green) arrows and black dash lines, respectively. The device contacts collect holes generated from the top stage of the stack and electrons generated from bottom stage of the stack. Due to the current continuity requirement in a series-connected structure, unequal carrier generation in different stages will result in the recombination of extra carriers in stages with a higher carrier generation. Therefore, current matching between different stages in multiple-stage PV devices is an important design consideration. Optically farther stages are designed to be thicker to attain equal absorption for all the stages, and the optimum thickness of each absorber layer is calculated based on the average absorption coefficient for InAs/GaSb SL absorbers.

ICPDs offer several advantages including high device resistance, reduced shot noise, feasibility to perform well at high temperatures and long wavelength, and high-speed operation without compromising sensitivity [33, 39-42]. First, the resistance for an ICPD is proportional to the number of stages (N_a) and therefore is much higher than a conventional photodiode. Second, similar to a quantum well infrared photodetectors (QWIPs), the signal-to-noise ratio due to the shot noise is proportional to $\sqrt{N_a}$ in ICPDs [39]. It is easy to understand when considering an additional stage as adding an

extra trial to the measurement. Since the noise that results from interband excitation is a random process, multiple stages are equivalent to multiple trials leading to a lower uncertainty and thus low noise [43].

Moreover, ICPDs have a great potential to achieve high detectivity at high temperatures in the long wavelength region, where the absorption coefficient and carrier lifetime decrease [39, 41]. In the conventional photodiode, the small absorption coefficient is compensated by a thick absorber, which leads to an insufficient collection of photogenerated carriers due to the short carrier lifetime (short diffusion length). The quantum efficiency of ICPDs is not limited by the problem since each absorber can be designed to be shorter while the total absorber thickness is longer than the diffusion length. It was experimentally demonstrated that multiple-stage ICPDs with short absorbers are able to operate at high temperatures over a wide infrared spectrum (2-16 μm) [44-47]. For the same reason, ICPDs allow a short transit time for photogenerated carriers to be collected at the interface of adjacent stages without sacrificing the total absorber thickness. Therefore, ICPDs can respond quickly to direct optical modulation at high frequencies while achieving a high sensitivity [42].

1.2.2 Operating Principle of Interband Cascade Photovoltaic Device

The ICPV device was proposed to be a component of a thermophotovoltaic (TPV) system [48]. It uses an InAs/GaSb SL as the absorber layers and is stacked with unipolar barriers to form tandem cells [48]. The type-II SL is a suitable absorber material because its bandgap can be tailored over a wide infrared range. TPV systems

convert radiant energy from a heat source into electricity. Low-temperature sources (500-2000 K) mainly radiate in the mid-infrared region of the electromagnetic spectrum. In contrast to a typical solar cell panel, a TPV system usually includes a filter and an emitter (or a selective emitter) between the heat source and TPV cell. This transforms the source spectrum to one that is better matched to the TPV cell's spectral response. By making efficient use of the spectra, TPV systems can have high conversion efficiencies. Because TPV systems are clean, compact, and portable, they are well suited for space nuclear power applications [49, 50], concentrated solar power systems [51], and fossil-fuel-burning power systems [52].

The bandgap of a TPV cell determines the lowest energy (the longest wavelength) of radiant photons that can be absorbed and used for generating electricity. Photons with energy lower than the bandgap are not utilized, leading to a reduction in TPV system efficiency. Because a high source temperature can cause problems for system operation and stability, and degrade the efficiency of the PV cell by overheating it, low-temperature heat sources are preferred for TPV systems. This is especially true when the cell is close to the emitter for obtaining a high power density or when a required cooling system would be too expensive or too large for the application [50, 52, 53]. Based on a detailed balance model [53], the optimum bandgap for blackbody-like heat sources with temperatures in the range of 1000 to 2000 K lies within an energy range of 0.2 to 0.4 eV. This is smaller than the bandgap of most materials (0.5-0.7 eV) proposed for TPV conversion [54-56]. A conventional PV *p*-*n* junction device with a narrower bandgap material (<0.5 eV) has a higher level of dark current and shorter carrier lifetimes, which result in lower efficiencies and a

lower open circuit voltage. Therefore, type-II SLs designed at 3 to 5 μm (0.41 to 0.23 eV) [57-60] were applied as absorbers in the ICPVs to serve the TPV systems. Utilizing absorbers with a different bandgap in each cascade stage will enable efficient conversion of photons at different energies from a broadband heat source, similar to the idea of a multijuction solar cell, while using multiple discrete absorbers with the same bandgap will improve the collection efficiency of photo-generated carriers and facilitate the current matching between different stages.

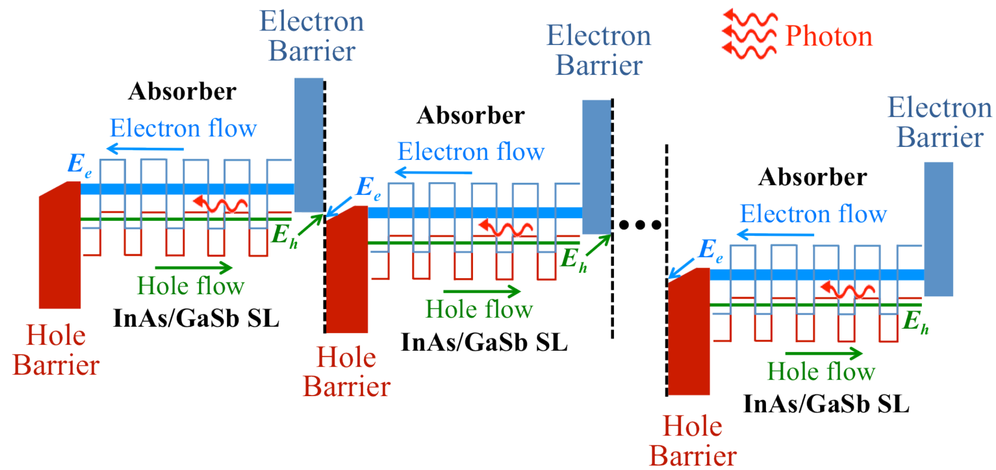

Figure 1.4: General schematic for an ICPV device under a forward bias. Each stage is composed of a superlattice absorber sandwiched between electron and hole barriers. E_e and E_h denote the energy for electron (thick line) and hole (thin line) minibands, respectively. The energy difference (E_e - E_h) corresponds to the bandgap (E_g) of the SL. Arrows represent the flow direction of electrons and holes, which are generated in the SL absorber and recombine at the electron and hole barrier interfaces (dash lines) through interband tunneling.

Figure 1.4 shows a general schematic for an ICPV device, which is almost the same with ICPD device shown in Figure 1.3 except working under a forward bias. Therefore, ICPV and ICPD share the same advantages in collecting the photogenerated carriers, which is the most crucial part of the radiation conversion. Similarly, each absorber thickness in an ICPV is kept shorter than a typical diffusion

length, so that ICPV devices are able to collect the photo-generated carriers with nearly 100% efficiency in each stage [59, 60]. Since the incident photon flux is partitioned amongst the various stages, the photocurrent is relatively low, but the photo-voltages from each stage add together to create a high overall open-circuit voltage. Therefore, the output power of an ICPV device remains high while the low current reduces the power loss across the contact resistance. This property could circumvent the high current density in a typical TPV system that results from a narrower bandgap than in solar cells. In addition, the ideal ICPV structure has no depletion region, which is unavoidable in conventional TPV cells, and this leads to a suppressed Shockley-Read-Hall recombination current [59]. With these features, ICPV devices are an attractive option for achieving efficient conversion of long-wavelength radiation. ICPVs with a bandgap of 0.23 eV will be discussed in Section 5.2.

1.3 Dissertation Introduction

The development of the high-quality heterostructures relies on the technology of MBE, which is the most suitable method for satisfying the stringent requirements of sophisticated structures. The growth of the SL and quantum wells using 6.1 Å materials began in the 1980s led by Chang *et al*. at IBM [61-64]. A summary of the early studies of properties and growth of InAs/GaSb quantum wells and InAs/AlSb SLs can be found in the review article [65]. In the past decades, studies became more systematic and in-depth with the use of various diagnostic tools for material characterizations, such as x-ray diffraction (XRD), photoluminescence (PL), transmission electron microscopy (TEM), scanning tunneling microscopy (STM), and

minority carrier lifetime measurements. The ultimate goal is to improve the structural, optical, and electrical properties of the SLs and quantum wells. This can be accomplished using growth conditions that may be different from the bulk material growth conditions because of the interface chemistry, strain-balancing requirements, and the compromise of growth conditions among various materials. Key aspects of past experimental studies include, but are not limited to, understanding the formation of interfaces [66-69], studying the effect of interface bond configuration [70-73], finding optimum growth methods for the interfaces [74-78], and investigating the optimum growth conditions [79-82].

With a contribution from improved material qualities, significant progress has been achieved in various devices. Take interband cascade lasers as an example. The first GaSb-based ICL operated at 3.8 μm up to a temperature of 170 K in pulsed mode with a threshold current density of 4.17 kA/cm^2 at 80 K in 1997 [11]. The device was damaged soon after the operation due to a non-optimized structure as well as the poor material quality. Less than 20 years later, the highest operation temperature for GaSb-based ICLs has been as high as 118°C (~391 K) with a threshold current density as low as 106 A/cm^2 at room temperature at around 3.8 μm in continuous wave (cw) mode [12]. InAs-based ICLs have a maximum operation temperature of 308 K in cw mode and a threshold current density as low as 247 A/cm^2 at room temperature in pulsed mode at around 4.6 μm [20]. Moreover, GaSb-based narrow-ridge ICLs were reported to operate at 90°C (~363 K) and at its maximum cw power for about 10,000 hours [83]. The data suggests a projected lifetime of more than 45 years and

demonstrates that 6.1 Å materials are highly reliable for inexpensive applications in even rigorous field environments.

While remarkable progress has been attained for MBE growth of high-quality heterostructures of 6.1 Å materials, there are still challenges. On one hand, device structures consist of hundreds of quantum wells and require atomic layer precision in thickness control. On the other hand, optimization criteria may not necessarily correlate to the same degree, *e.g.* the growth conditions that minimize the density of one type of defect (such as Shockley-Read centers) may not suppress some other defect (such as interlayer mixing), and the growth method that gives better structural properties (such as interface roughness) may not give superior optical properties (such as minority carrier lifetime). This work focused on the MBE growth optimization of IC devices based on the 6.1 Å materials including InAs-based ICLs, IC photovoltaic (PV) devices and IC photodetector (PD) devices. Material quality was investigated using differential interference contrast (DIC) microscopy, XRD, scanning electron microscopy (SEM), and atomic force microscopy (AFM). Electrical and optical properties of the devices were also used as guides in the growth.

The subsequent chapters of this dissertation present detailed research on the foundations of the MBE growth as well as the characterizations of the materials. Chapter 2 introduces the MBE growth technique including the control of growth conditions and the use of the GEN II and the GENxplor MBE systems. Details of how to achieve atomic layer precision are discussed, focusing on the control and calibration of substrate temperatures, cell stabilities, and growth rates. In Chapter 3, the primary material characterization methods (XRD, AFM, and SEM) are introduced in detail.

Operating principles and useful information on advantages and limitations are discussed. Chapter 4 starts with InAs (001) homoepitaxy where the defect morphology and origination are explored. The growth conditions for InAs-based ICLs are presented together with results from the device performances. Chapter 5 focuses on growth condition and characterizations of the ICPV and ICPD structures. The interfaces of InAs/GaSb SLs are studied with the goal of improving the ICPDs designed for the long-wavelength infrared region. The main conclusions and a discussion about future perspectives are presented in Chapter 6.

Chapter 2 Molecular Beam Epitaxy Growth

2.1 Introduction

Molecular Beam Epitaxy (MBE) is a powerful technique that is used for layer-by-layer growth of semiconductors, metals and insulators. Compared to other epitaxial growth techniques, such as physical vapor deposition (PVD), chemical vapor deposition (CVD), liquid phase epitaxy (LPE), and metal organic vapor phase epitaxy (MOVPE), MBE is more capable of growing sophisticated heterostructures due to its atomic dimensional precision of single crystal layers on crystalline substrates. The atomic precision is achieved through a precise control of molecular or atomic beams vaporized from high temperature sources onto a heated substrate in an ultra-high vacuum (UHV) environment.

Figure 2.1 shows a schematic diagram of a typical solid source MBE growth chamber with a vertical design as the cells are facing upward. The UHV environment ($<10^{-9}$ Torr) is achieved by the cryopanels cooled with liquid nitrogen and a pumping system. The UHV allows a large mean free path (longer than a mile) of the reactant molecules, which ensures a direct traveling path from the source to the substrate without scattering and minimizes the impurities being incorporated into an epitaxial layer. The cryopanels also help isolate the cells from each other to avoid temperature interference, or local overheating inside the chamber. The cells contain source material with a high purity (most of them >99.9999%) and each is heated individually to create molecular beams. By installing the cells facing toward the substrate, the beams impinge onto the substrate uniformly. Moreover, the substrate is rotated during the growth at a constant rate to ensure the uniformity. A shutter is installed in front of

each cell with an actuator and controlled by a computer to block a beam or let it to pass. This allows layers with different compositions to be grown in a sequential fashion.

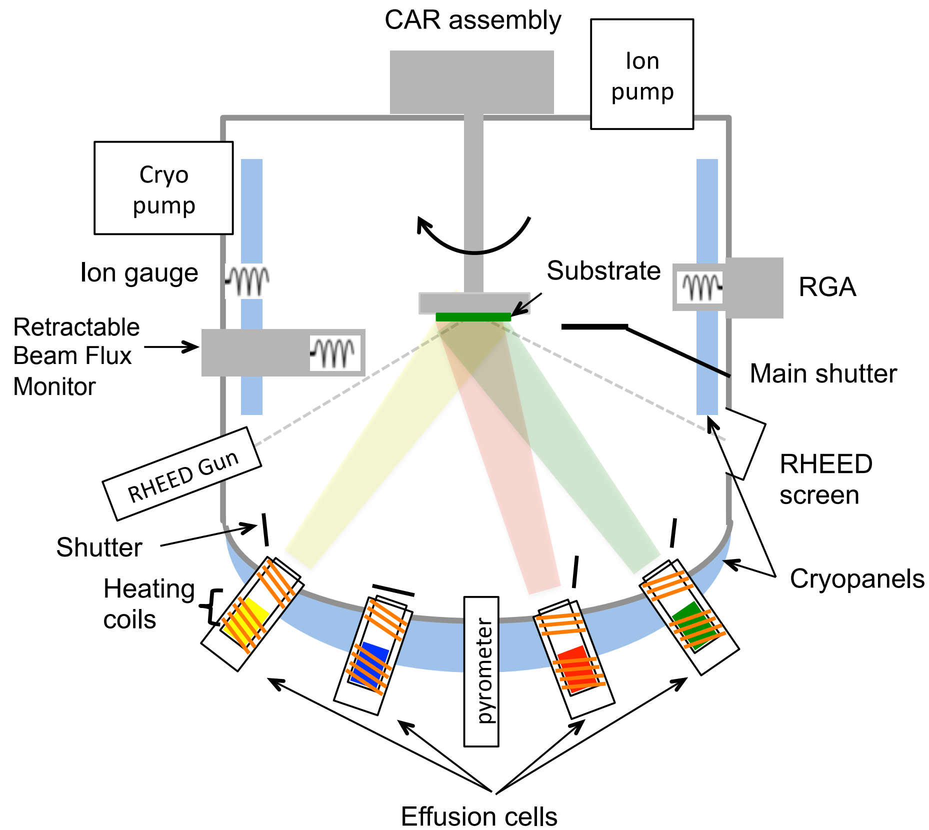

Figure 2.1: Schematic diagram of a typical MBE growth chamber with a vertical design.

Inside the growth chamber, an ion gauge is installed to monitor the vacuum. Moreover, another ion gauge, called a beam flux monitor (BFM), is installed to measure the flux coming from the sources, in forms of a beam equivalent pressure (BEP). It is designed to measure the flux at the same position (or approximately the same) as the substrate holder so that the BEP can be used as a reference for the growth rate calibration. A residual gas analyzer (RGA) that works as a mass spectrometer is

also installed to monitor contamination. By mounting the RGA in a cell port, it can potentially be used to study the grow dynamics, such as surface stoichiometry, sticking, and incorporation.

One technique that is critical to the successful growth by MBE is the *in-situ* characterization technique called reflection high-energy electron diffraction (RHEED). As shown in Figure 2.1, the RHEED system consists of an electron gun with accelerating energy of 10-15 KeV and a phosphorescent screen. A high energy electron beam strikes the sample at a shallow incidence angle (1-3°) and is reflected and diffracted onto the phosphorescent screen in the growth chamber, as shown in Figure 2.2 (a). The wavelength of the high-energy beam is similar to the lattice distance between the atoms and therefore the diffraction pattern is sensitive to the atomic arrangement. Since the beam strikes at a shallow angle, the diffraction pattern is dominated by the two-dimensional lattice of atoms on the top few atomic layers on the surface.

The diffraction of the lightly disordered two-dimensional surface forms streaks in the RHEED pattern, and the relative intensities of the streaks are determined by the surface reconstruction of atoms in surface layers. Figure 2.2 (b) shows an example of a 3× RHEED pattern during the GaSb growth, where the incident beam is along the [-110] azimuths. Figure 2.2 (a) demonstrates the orientation of the incident beam and the wafer, where the incident beam is along the [-110] azimuths and the wafer has an orientation flat (major flat) in (0-1-1) plane following the SEMI-EJ standard. In the RHEED pattern, the refraction of bulk atoms provides a stronger intensity (the spots marked by a arrow in Figure 2.2 (b)), and the reflection of the top few monolayer

atoms provides a weaker intensity. Due to the reconstruction on the surface, the periodicity of the surface atoms is three times of the bulk atoms in the real space. Therefore the space between the strong rods is separated into three parts by the two weak rods in the RHEED pattern, which is called 3×. The pattern is also sensitive to the surface morphology. The pattern is streaky and clear, which suggests a layer-by-layer growth mode. If the RHEED pattern is diffuse and spotty, then the surface is rough with islands forming on it. In addition, RHEED can also be used to determine the substrate temperature and calibrate the material growth rate by observing the changes of the RHEED pattern. More applications of RHEED will be discussed in Section 2.2.3.

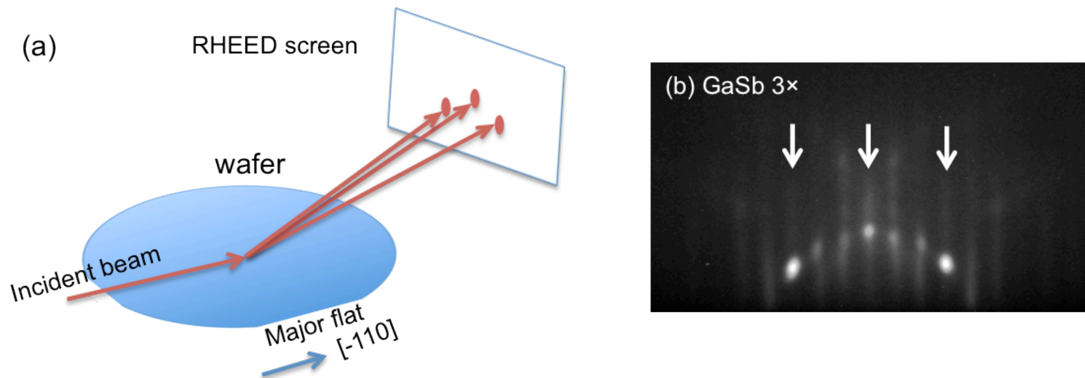

Figure 2.2: (a) Schematics of an electron beam striking the wafer along [-110] and being reflected and diffracted onto a RHEED screen. The wafer has an orientation flat (major flat) in (0-1-1) plane following the SEMI-EJ standard. (b) 3× RHEED pattern during the GaSb growth, where the incident beam is along the [-110] azimuths.

2.2 The Control of Growth Conditions

In order to achieve reproducible and precise growth of sophisticated structures, a reliable control over the growth conditions is essential. The growth processes involve atom/molecule absorption, incorporation, migration, diffusion, and desorption, which are mainly governed by the substrate temperature and the amount of group-III and group-V flux. Specifically, the group-III flux determines the growth rate and thus the layer thickness in the structure.

2.2.1 Substrate Temperature Measurement

The determination of the substrate temperature is more challenging than one might assume. The easiest approach is to use the thermocouple that is installed on the substrate heater to monitor the temperature. Due to the limitation in the position of the thermocouple, the measured temperature from the backside of the substrate holder differs from the actual substrate temperature. Furthermore, the reading can vary from machine to machine depending on the substrate holding mechanism and substrate heater configuration. For example, the oxide desorption temperature of the GaAs substrate is known to be around 580°C, but the thermocouple reading was ~720°C in our GENxplor system, and ~690°C in the GEN II system.

A pyrometer can be used to better monitor the substrate temperature. The technology is based on the infrared radiation from the substrate, which can be detected through the chamber window and focused onto a detector. The detector measures the emission intensity from the substrate in a narrow spectral range where its emissivity remains constant in an operating temperature interval [84]. According to Planck's law

for the emissivity of real bodies, the temperature can be deduced with a known spectral radiation and emissivity at a certain wavelength.

$$R_{\lambda,T} = \varepsilon(\lambda,T)\frac{2hc^2}{\lambda^5}\frac{1}{\exp\left(\frac{hc}{k_B\lambda T}\right)-1} \qquad (2.1)$$

Where h is the Planck constant, k_B is the Boltzmann constant, c is the speed of light in the medium, T is the actual temperature of a real body, and $\varepsilon(\lambda,T)$ is the emissivity of the real body.

Even though the emissivity of most of the III-V material is approximately known, a calibration of the emissivity is needed. The pyrometry allows the temperature measurement without physically touching the target. However, on other hand, the uncertainties arise in the optical path, *e.g.* the deposition of growth material on the pyrometer window changes the transmission coefficient of the infrared light. The pyrometer can be calibrated by using the oxide desorption temperature of GaAs substrate as a reference, which is well known and equals 580°C. The 2× RHEED pattern on the [-110] azimuths becomes brighter and clearer once the temperature reaches the oxide desorption temperature. In order to allow enough time to stabilize the temperature and observe the transition point, a ramp rate lower than 10°C/min is suggested.

Another calibration reference is the flux-temperature phase diagrams for the surface reconstruction transition. It is more widely used for low substrate temperature growth, since the phase transition occurs within or near typical substrate temperature ranges for growth of InAs, InSb, and GaSb [85]. A.S. Bracker *et al.* [85] published a practical paper on surface reconstruction phase diagrams for InAs, AlSb, and GaSb,

which has been recognized as a reference in the MBE growth community. For example, the pyrometer was calibrated in the GaSb growth by adjusting the emissivity for a reading of 413°C at the transition of the GaSb surface reconstruction between (1×3) and (2×5) with an Sb_2 growth rate of 1 ML/s in the GENxplor. Figure 2.3 shows the RHEED pattern at the [-110] azimuths on GaSb layers at a thermocouple temperature of 470°C and 330°C respectively for (a) and (b). The transition from 3× to 5× occurred at a thermocouple temperature of ~470°C. The center two streaks in Figure 2.3 (a) started to become diffuse compared to the one in Figure 2.2. Note that measurement of group-V growth rate or beam-equivalent pressure is required in this method, which will be discussed in the next section.

In the use of the pyrometer, the selection of the right operation wavelength is important. The detector's wavelengths have to be shorter than the corresponding minimum wavelength for transmission through the epilayer/substrate, $\lambda = hc/E_g$, where h is Planck's constant and c is the speed of light, and E_g is the bandgap of the epilayer/substrate. Heater radiation with a wavelength shorter than the substrate corresponding wavelength are mostly absorbed by the thick substrate, while the longer wavelengths will pass through the substrate directly. If the pyrometer detector works in the longer wavelength range, it will "see" the heater behind the wafer and result in a very high pyrometer reading [84]. For example, because the BASF EX11984 pyrometer operates at a wavelength of 1550 nm, it is suitable to measure growth on GaSb (0.73 eV, 1710 nm) and InAs (0.35 eV, 3540 nm) substrates, but would not be useful for GaAs (1.43 eV, 870 nm) substrates. Meanwhile, it would have difficulty

detecting a lower temperature (<350°C) since the radiation intensity is reduced and the peak intensity shifts to a longer wavelength.

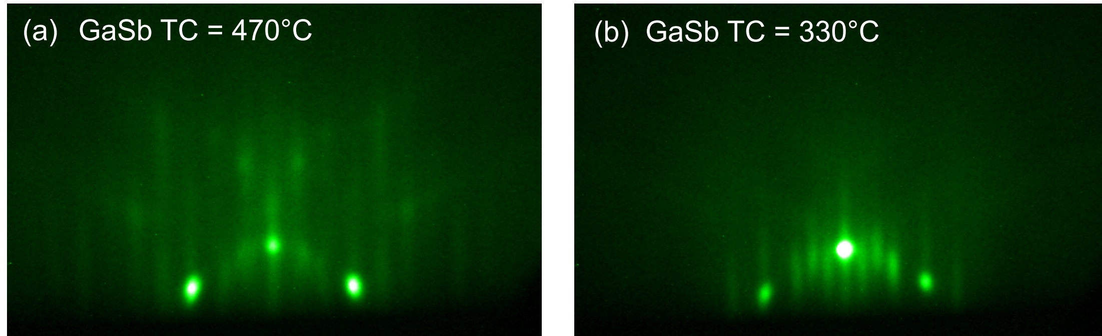

Figure 2.3: The RHEED patterns at the [-110] azimuths on a GaSb surface at a thermocouple temperature of (a) 470°C (3×) and (b) 330°C (5×).

Figure 2.4 shows an example of an ICPD growth with the GaSb oxide desorption and a change of substrate temperature during growth. The dashed line represents thermocouple data and the solid line represents the pyrometer temperature measured with an emissivity of 0.65 and a calibration factor of 0.8288 by the BASF EX11984 pyrometer. The difference between the thermocouple and pyrometer reading is not always constant at all temperature ranges. The spot size of the collection optics is about 6 mm with a 500 mm distance. It is possible that the optics detect light emitted from the edge of the half 2-inch-diameter wafer during rotation, and thus the reading can fluctuate due to the temperature difference over the wafer surface. Composition changes in the structure also result in the temperature fluctuations shown in the inset of Figure 2.4. The fluctuation period corresponds to the time needed to grow one period in the SL (~66 second). This is because the pyrometer reading is affected by light from the higher temperature object inside the chamber, *e.g.* a silicon doping cell operating at 1250°C. Therefore doping of the layers results in extra

radiation that increases the pyrometer reading. The fluctuations were not observed in the thermocouple reading.

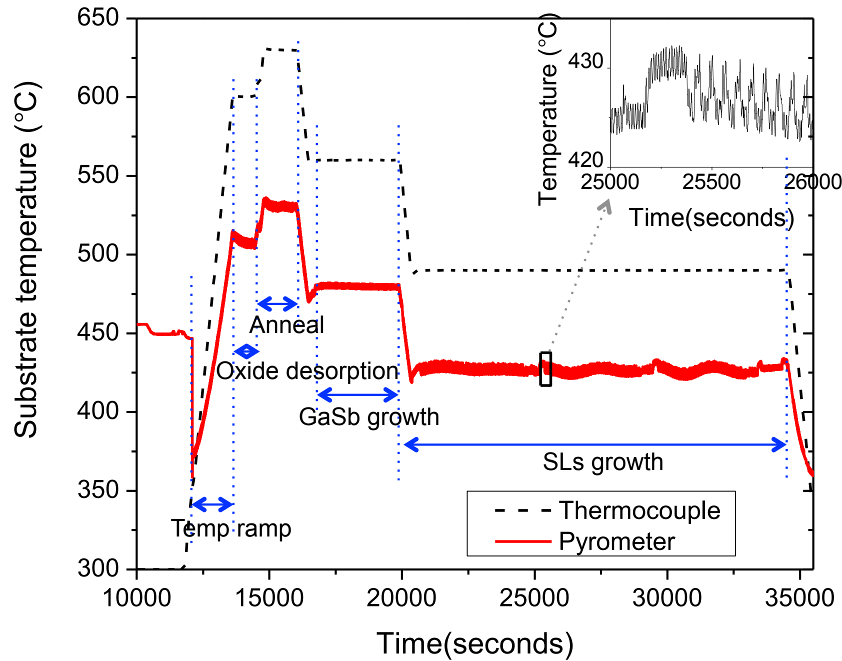

Figure 2.4: Temperature as a function of time during growth of ICPD. The dashed line represents thermocouple data and the solid line represents pyrometer temperature with an emissivity of 0.65 and a calibration factor of 0.8288 by BASF EX11984 pyrometer. The inset shows the data around 25000 second marked by the rectangular.

The third popular way to determine the substrate temperature is band edge thermometry. The method also measures the infrared light coming from the substrate, but monitors the wavelength at which the substrate changes from absorbing to transmitting light. Based on the fact that the band gap varies with temperature, the substrate temperature can be determined with the known database. Compared to pyrometry, band edge thermometry requires a better optical system and software, and can be affect by the dopant level, but it will not be affected by the coating on the

window and can monitor low temperatures. So far the most popular company in the field, kSA BandiT, uses an InGaAs array as the wavelength spectrometer aiming at 870-1670 nm. The wavelength range is the longest among their products, however, is still not suitable for InAs, GaSb, and InSb substrates.

2.2.2 Flux Control

The fluxes of group-III and group-V materials are very crucial parameters and greatly affect the agreement between the grown structure and the designed one, as well as the reproducibility between samples.

The flux and growth rate depend on cell temperatures. Therefore, first of all, good temperature control is essential, which is achieved by using a proportional-integral-derivative controller (PID controller). It is a control loop feedback mechanism based on present (proportional term), past (integral term) and possible future (derivative term) deviations between the desired setpoint and the measured temperature. The three correcting terms, PID values, have to be determined at the cell operation temperatures and summed to calculate the output of the PID controller. Automatic tunings are available in our Eurotherm PID controllers to calculate PID values. By turning on and off (or reducing and increasing) the output, an oscillation in the temperature will be induced. The PID values will be calculated based on the amplitude and period of the oscillation. If automatic tuning gives unsatisfactory results, one can tune the controller manually. There are a number of standard methods for manual tuning, and the Ziegler-Nichols method is recommended. A procedure can be found in the reference [86] for Eurotherm controllers.

Instead of using the automatic tuning results, one can adjust the PID values based on cell situations. For example, higher P values have a slower output response to the changes and thus are suitable for doping cells and group-V cells. Lower P values have a faster output response and thus suitable for situations in which a large temperature change is anticipated [87]. An example will be given in Figure 2.6 in later discussions.

In addition to the temperature control, the shutter transient and the material distribution inside the cell can also affect the stability of the flux. Figure 2.5 shows an example of the shutter transient in a single zone Al cell with a cone shaped crucible. The temperature had been stable for more than one hour before measurement. The temperature, output power, and the BFM reading were monitored when the recipe opened the shutter for 30 sec and waited for 15 minutes before opening again. The PID values were P=30.6; I=8.8; D=2.11 following a Ziegler-Nichols tuning procedure. Figure 2.5 (a) shows a BFM measurement with PID control. It is found that both the output power and the temperature responded to the shutter movement as the temperature fluctuated by ±0.4°C, and the BFM reading decreased from 9.26×10^{-8} Torr to 8.83×10^{-8} Torr during the 30 seconds (~5%). The cell's heat loss increases when the shutter is open because the shutter is at a higher temperature than the objects in the cells line of sight when the shutter is open. The thermocouple senses the temperature drop and leads to a rise in output power.

The effect is confirmed in the measurement showing in Figure 2.5 (b), where power control is shifted to a manual mode output a few seconds before the shutter opens and returns back to PID control when the shutter closes. Therefore an output

power response was intentionally disallowed when the shutter was open. In this case, the Al cell temperature dropped ~2.5°C until the PID control returned with an increased output power. The BFM reading decreases more significantly compared to (a) from 8.82×10^{-8} Torr to 8.00×10^{-8} Torr during the 30 seconds (~10%). Both the temperature and the BFM reading responded more dramatically to the shutter transient effect compared to a normal PID control. It also suggests that it takes more than 30 seconds to acquire a stable BFM reading for this cell.

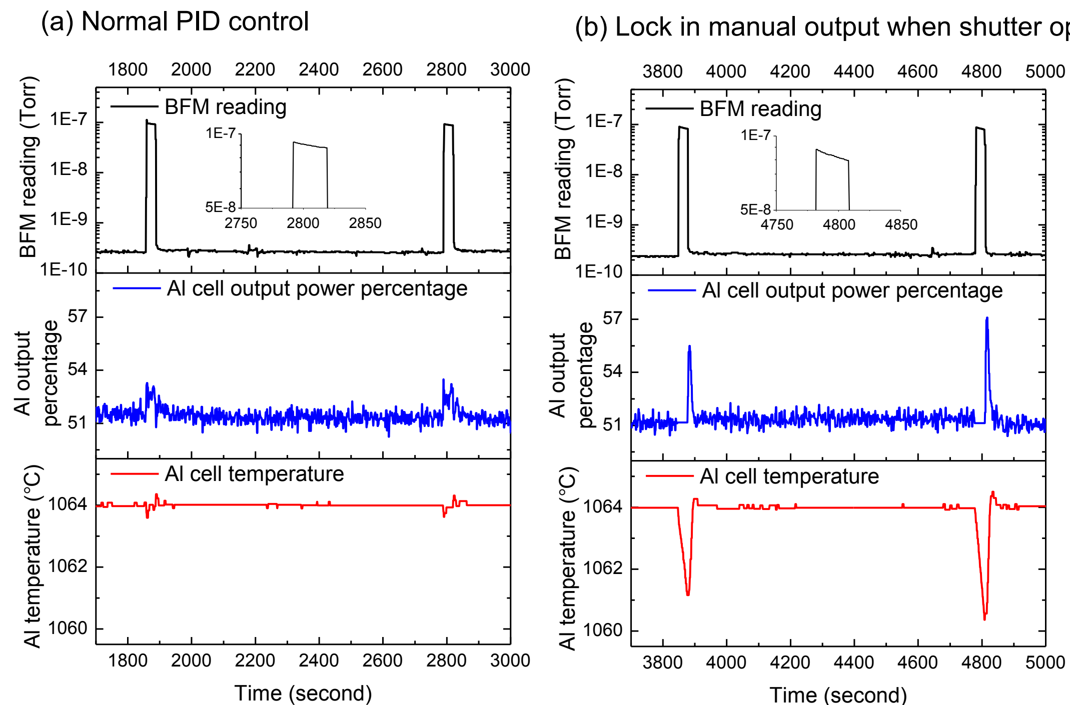

Figure 2.5: The temperature, output power percentage, and the BFM reading during shutter cycling in a single zone Al cell with a cone shape crucible. (a) A measurement that has a normal PID control. (b) A measurement where power control is shifted to a manual mode output a few seconds before the shutter opens and returns back to PID control when the shutter closes.

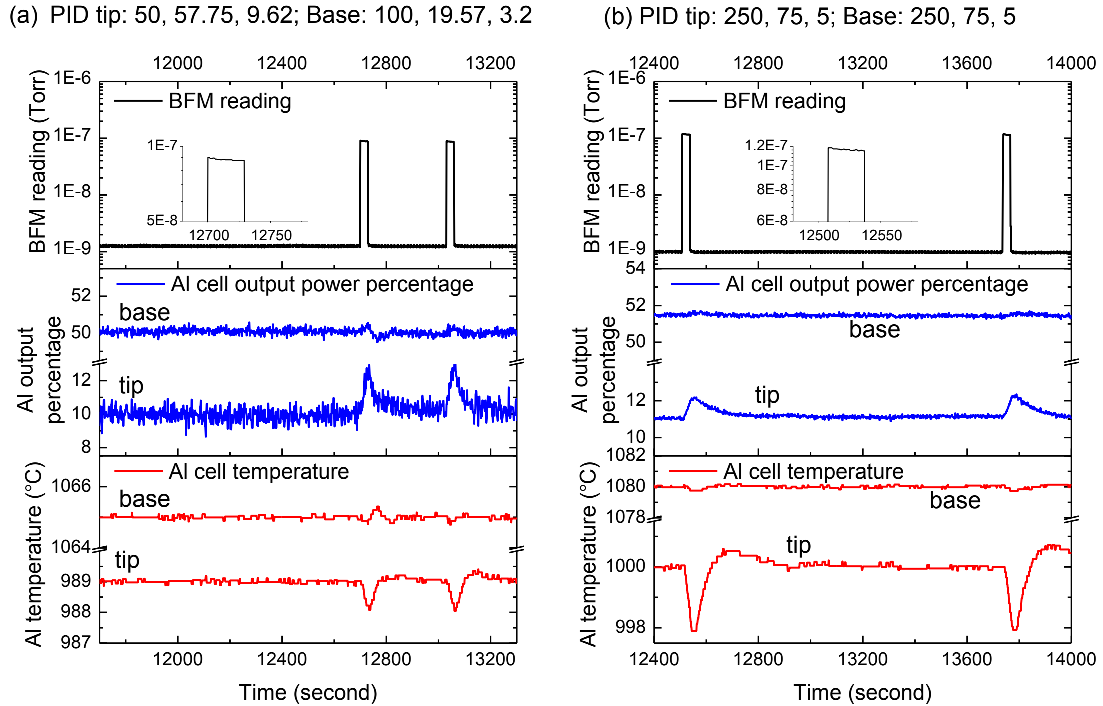

Figure 2.6: The temperature, output power percentage, and the BFM reading during shutter cycling for a sumo crucible in a dual-filament cell. (a) PID values were 50, 57.75, and 9.62 for the tip, and were 100, 19.75, and 3.2 for the base zone. (b) Default PID values were 250, 75, and 5 for both tip and base zones.

The shutter transient issue is reduced for a sumo crucible in a dual-filament cell that controls the tip and base separately. The small tapered orifice reduces the heat radiance loss inside the crucible. The base temperature is controlled individually and is less affected when the shutter moves. Therefore, the shutter transient issue is minimized since the base temperature contributes to the flux more than the tip. Figure 2.6 gives an example of the shutter transient effect for a sumo Al cell in a dual-filament cell in the GENxplor. In Figure 2.6 (a) the PID values for the tip and base were acquired from the automatic tuning by keeping the other heat zone stable at a manual mode. To adjust the power output response rate, the P value was set based on previous experience. The PID values were 50, 57.75, and 9.62 for the tip, and were 100, 19.75, and 3.2 for the base zone. Temperature and output power responses to the

shutter movements were still observed. The base temperature varied ±0.3°C, while the tip temperature decreased by 1°C during opening and closing. Even though the tip temperature changed more significantly compared to Figure 2.5 (a), the BFM reading was more stable. It decreased from 8.88×10^{-8} Torr to 8.71×10^{-8} Torr during 30 second (~2%) and took less than 20 seconds to become stable.

Figure 2.6 (b) shows a measurement conducted with default PID values of 250, 75, and 5 for both tip and base zones. The output power trace was smoother than in measurement (a). This is because the P value was much larger in (b) and thus the output power response was slower. As a result, the tip temperature dropped more (2°C instead of 1°C) as it took longer to launch a higher output power. However, since the base temperature was stable, the BFM reading had a small variance from 1.18×10^{-7} Torr to 1.15×10^{-7} Torr during 30 second (~2.6%). Therefore, despite the PID values, the sumo crucible and dual-filament cell help increase the cell stability and reduce the shutter transient problem.

For the Al dual-filament cell, the tip is heated to a lower temperature than the base to limit the creeping of Al out of the crucible. On other hand, the uniformity is also a function of the tip temperature since the aluminum creeps throughout the interior of the crucible and provides a portion of the flux [88]. Therefore, the tip temperature is set to be ~10°C higher than the unpowered tip temperature. The operation rules are different for a Ga and In dual-filament cells, where the tip is heated to a higher temperature (75-90% of the total power to the cell is to the tip [89]). The material will not condense at the crucible lip, which reduces the spitting problem.

2.2.3 Growth Rate Calibration

After achieving a stable temperature, a cell is capable of providing a stable flux, which has to be calibrated to a growth rate. The BFM reading is affected by elemental species, incidence angle, temperature, ionization potential, and the calibration of the ion gauge. Therefore it greatly depends on the MBE system. The group-III cell's flux can be calibrated from RHEED oscillations [90]. As a result, a beam equivalent pressure versus temperature, versus growth rate relationship can be established.

RHEED oscillations are mostly strongest for the specular reflection, which is intense and sharp for a smooth surface and is weak and broad for a rough surface. In a layer-by-layer growth mode, a minimum intensity appears when a half monolayer is deposited, and a maximum intensity corresponds to a maximum smoothness when a full monolayer is grown. Therefore, one oscillation period corresponds to the growth of one monolayer, and the growth rate in ML/s can be calibrated by counting the number of oscillations and averaging them over time. Figure 2.7 shows RHEED oscillations for GaAs growth on a GaAs substrate recorded by the software. The oscillations can also be recognized by eye. The oscillations dampen out since wide islands form gradually during the growth and eventually reach a steady state of surface roughness. The smoother the starting surface, the more oscillations can be acquired in one shutter opening. In our system, Ga (growth of GaAs) and Al (growth of AlAs) were routinely calibrated on a GaAs substrate at a substrate temperature of ~580°C with a 500 nm buffer layer. A 50~100 nm GaAs layer was grown after each AlAs calibration layer to smooth out the surface. Indium (growth of InAs) can also be calibrated on the GaAs substrate at a substrate temperature of ~430°C with a thicker

buffer layer (~1 μm), which provides a smoother surface and a nearly fully relaxed condition. Note that the optimum amount of arsenic overpressure is essential to obtain more oscillations, *i.e.* a moderate amount of arsenic (V/III BEP ratio of 5 in the GENxplor) provides more oscillations (> 7 clear peaks at 0.5 ML/s) than the calibration with a higher arsenic pressure.

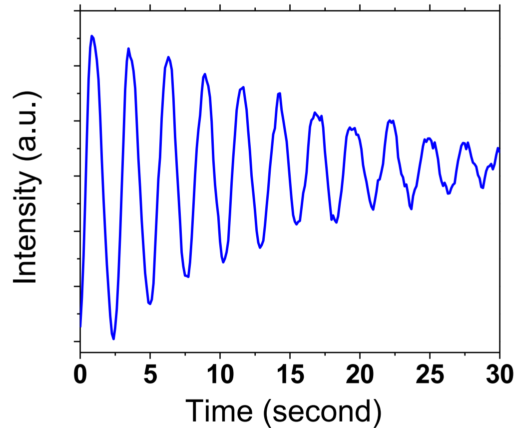

Figure 2.7: RHEED oscillations of during GaAs growth.

Figure 2.8 shows the calibrated relationship between temperature, flux (beam equivalent pressure) and growth rate for the gallium cell in the GENxplor. The relationship satisfies the Arrhenius equation, growth rate ≈ $B \times flux \approx A\ exp\ (-E_a/kT)$. A and B are variables, E_a is the activation energy of the element, k is the Boltzmann constant, T is the absolute temperature (in K). Therefore, log(flux) and log(growth rate) are proportional to 1/T, as shown in Figure 2.8 (a), and the flux and growth rate have a linear relationship, as shown in Figure 2.8 (b). The same relationships for two indium cells in the GENxplor are also plotted out in Figure 2.9. Even though the two indium cells have the same type of crucible and heater configurations, their calibrations are

very different from each other mainly due to the thermocouple contact, source material distribution, and the relative location of BFM ion gauge.

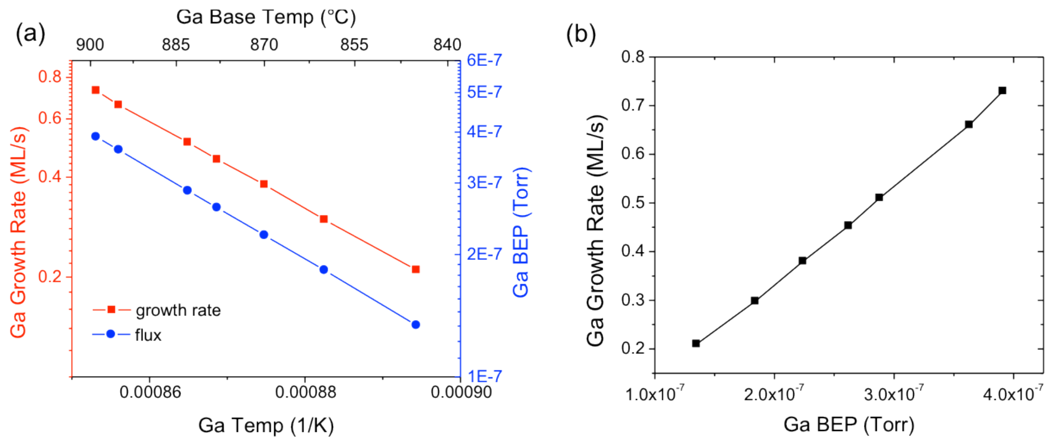

Figure 2.8: (a) Gallium growth rates (left side, squares) and beam equivalent pressures (right side, circles) versus base cell temperatures in the GENxplor. (b) Gallium growth rates versus beam equivalent pressures.

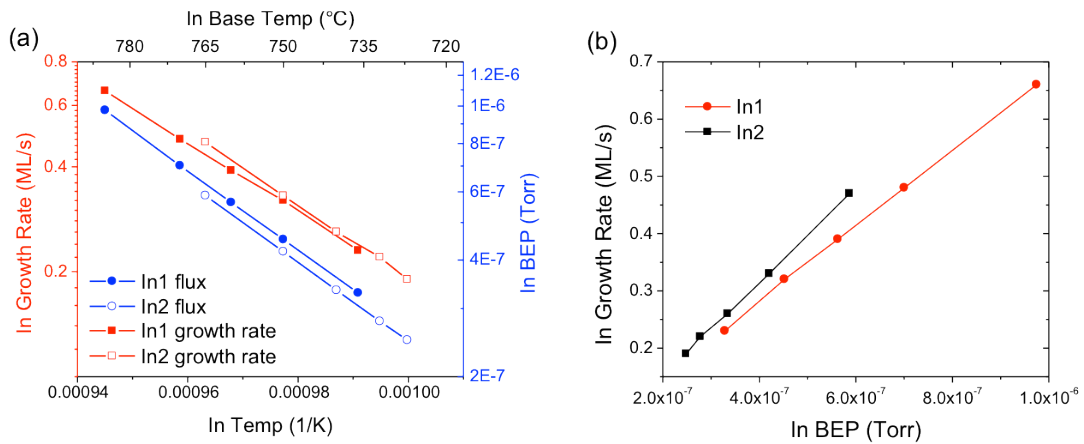

Figure 2.9: (a) Two indium cells' growth rates (left side, squares) and beam equivalent pressures (right side, circles) versus base cell temperatures in the GENxplor. (b) Indium growth rates versus beam equivalent pressures for two cells.

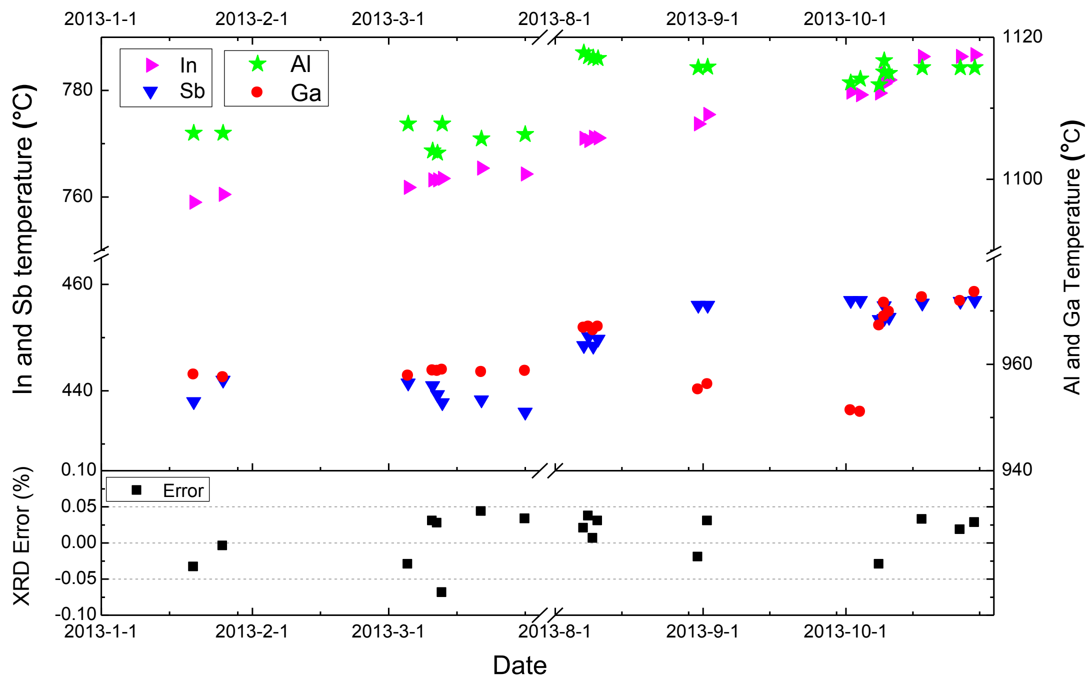

Figure 2.10: Cell temperatures for 27 growths in 2013 in the GEN II. Black squares are period errors calculated from x-ray diffraction measurement, suggesting thickness differences between the designed structures and the grown structures.

The flux at a certain temperature changes in everyday growth due to several reasons, such as the changing of the surface area due to the consumption of materials, redistribution of the material inside of the cell after a temperature cycle, and outgassing of materials. Fortunately the flux versus growth rate relation is relatively stable. Therefore a beam equivalent pressure from the BFM can be used as references and easily measured before the growth to achieve a repeatable growth rate. Figure 2.10 shows cell temperatures of 27 growths in 2013 in the GEN II during which growth statuses were stable. The growth parameters are listed in Table 2.1. Despite some growth rate adjustments for Ga and Sb based on structure changes or optimizations, the fluxes were kept mostly the same for the growths by adjusting the cell temperatures. The temperatures increased in a general trend as the materials were

consumed. However, they were not necessarily the same or in agreement with the increasing trend all the time in continued growths. For example, R107 was grown the next day after the growth of R106. However, Ga and Sb temperatures of R107 were 0.7°C and 2.2°C lower than that of R106, respectively.

Table 2.1: Growth parameters of 27 growths in 2013 in the GEN II.

Growth date	Structure	Design	Cell temperature (°C)				BEP (Torr)				XRD results (Å)		
			In	Al	Ga	Sb	In	Al	Ga	Sb	Designed	Deduced	Error (%)
1/20/13	R093	ICL	759	1106.5	958	438	1.28E-07	~9.94E-8	1.57E-07	~4.48E-7	478	461.9	-0.034
1/26/13	R094	ICL	760.5	1106.5	957.5	442	1.31E-07	~9.69E-8	1.59E-07	~4.58E-7	648	645	-0.0046
3/10/13	R095	ICL	763.2	1104	958.8	441	1.31E-07	~9.65E-8	1.59E-07	~4.58E-7	478	492	0.03
3/5/13	R096	ICL	761.8	1107.8	957.8	441.5	1.31E-07	~9.68E-8	1.59E-07	~4.58E-7	478	464	-0.03
3/11/13	R097	ICL	763.2	1103.7	958.7	439.3	1.31E-07	~9.65E-8	1.59E-07	~4.55E-7	478	491	0.027
3/12/13	R098	ICL	763.5	1107.8	958.9	437.8	1.31E-07	~9.68E-8	1.60E-07	~4.50E-7	509	474	-0.069
3/20/13	R099	ICL	765.4	1105.7	958.5	438.3	1.31E-07	~9.68E-8	1.60E-07	~4.50E-7	509	531	0.043
3/29/13	R100	ICIP	764.3	1106.3	958.7	436	1.31E-07	~9.64E-8	1.59E-07	~4.11E-7	48	49.6	0.033
4/2/13	R101	ICIP	764.6	1106.4	958.6	437.8	1.31E-07	~9.64E-8	1.59E-07	~4.11E-7	48	49.5	0.032
4/2/13	R102	ICIP	764.6	1106.6	958.5	437.5	1.31E-07	~9.62E-8	1.59E-07	~4.10E-7	48/2265	49.8/2320	0.038
4/11/13	R103	ICIP	765.4	1107.7	959.4	437.2	1.30E-07	~9.58E-8	1.57E-07	~4.10E-7	48	48.6	0.012
4/12/13	R104	ICIP	765.5	1107.7	959.3	437.3	1.30E-07	~9.62E-8	1.58E-07	~4.10E-7	48	49.1	0.022
8/7/13	R105	ICL	771	1117.8	966.8	448.5	1.31E-07	~9.64E-8	1.59E-07	~4.57E-7	480	489	0.02
8/8/13	R106	ICL	770.6	1117.3	967	450.2	1.31E-07	~9.61E-8	1.59E-07	~4.52E-7	480	498	0.037
8/9/13	R107	ICL	771.2	1117.1	966.3	448.4	1.31E-07	~9.62E-8	1.59E-07	~4.53E-7	480	483	0.006
8/10/13	R108	ICL	771.1	1117	967	449.7	1.31E-07	~9.60E-8	1.59E-07	~4.55E-7	480	494	0.03
8/31/13	R109	ICL	773.7	1115.7	955.2	456.1	1.31E-07	~9.60E-8	1.26E-07	~4.55E-7	468	460	-0.02
9/2/13	R110	ICL	775.5	1115.8	956.2	456.1	1.31E-07	~9.60E-8	1.26E-07	~4.55E-7	462	475	0.03
10/2/13	R111	ICL	779.7	1113.6	951.3	457	1.31E-07	~9.65E-8	1.12E-07	~4.55E-7			
10/4/13	R112	ICL	779.2	1114.1	951	457	1.31E-07	~9.65E-8	1.12E-07	~4.55E-7			
10/8/13	R113	ICIP	779.5	1113.3	967.2	453.4	1.31E-07	~9.64E-8	1.60E-07	~4.10E-7	48	46.5	-0.03
10/9/13	R114	ICIP	781.3	1115.1	968.9	453.6	1.31E-07	~9.64E-8	1.60E-07	~4.10E-7			
10/9/13	R115	ICIP	783.3	1116.7	971.5	456	1.31E-07	~9.62E-8	1.60E-07	~4.10E-7			
10/10/13	R116	ICIP	782	1114.9	969.8	453.8	1.31E-07	~9.64E-8	1.60E-07	~4.10E-7			
10/25/13	R117	ICIP	786.4	1115.7	971.8	456.8	1.31E-07	~9.62E-8	1.60E-07	~4.10E-7	71	72.3	0.018
10/17/13	R118	ICIP	786.4	1115.7	972.5	456.5	1.31E-07	~9.63E-8	1.60E-07	~4.22E-7	71	73.3	0.032
10/28/13	R119	ICIP	786.7	1115.7	973.5	457	1.31E-07	~9.65E-8	1.60E-07	~4.21E-7	71	73	0.028

The period errors from x-ray diffraction measurements are also plotted in Figure 2.10, indicating the thickness difference between the designed period and the grown one (more details about XRD can be found in Chapter 3.1). Since the structure contains multiple layers of InAs, GaSb, AlSb, or InSb, it is difficult to trace the true

growth rate of each group-III element. But the XRD result suggests that the growth rates are well controlled using the discussed calibration method, as the errors are less than 0.5% for most of the structures. The operation wavelengths are not listed in the table, since the designs were tuned each time and were not comparable with each other. However, they generally lay in the targeted area within 0.5 μm error.

2.3 MBE Facilities

There are two MBE systems used in the group for IC structure growth. The first one is an Intevac Gen II, which was operated from 1994 and is perhaps the most popular MBE system with over 220 sold since the 1980's according to the manufacturer. The system has a horizontal reactor with 8 ports plus a pyrometry port. Our system is equipped with an antimony cracker, a valved arsenic cracker, an indium dual zone effusion cell, a gallium effusion cell, an aluminum effusion cell, a silicon doping cell, and a beryllium doping cell.

In 2015, we started to run a new MBE system, a Veeco GENxplor, which has a lot of enhanced features. The system has a vertical reactor with 10 ports, which gives us more flexibility in choosing source materials compared to the GEN II system. All the group-III cells are dual-filament sumo cells, which can provide more stable flux as discussed in Section 2.2.2. Two indium cells are installed in the system so that two growth rates can be used in the growth structure without adjusting the cell temperatures. It will help save growth time in the IC laser growth, where a low growth rate is required for the SL layers but is not necessarily needed for thick InAs waveguide layers. The valved crack antimony cell provides more flexibility, since the valve controls the amount of flux that can be changed freely during the growth for different optimized growth conditions at the same cell temperatures.

In addition, tellurium (Te) doping is available in the GENxplor with GaTe source material loaded in the dual doping cell with a silicon source. In the GEN II, beryllium and silicon are used as p and n type dopants, respectively. However, n type doping for GaSb and AlSb is not possible, because silicon is an amphoteric dopant

that acts as a donor in the arsenides and an acceptor in most antimonides [91]. The new doping source, tellurium, is a group-VI element and can act as a donor in both antimonides and arsenides. Therefore it opens opportunities for antimony-based structures by making the n-type doping possible.

The vertical reactor geometry of the GENxplor makes use of the bottom space and the chamber volume. With a similar pumping system, a cryo pump and an ion pump, it takes less time to regain a good vacuum after the use of a high arsenic overpressure. The load/lock chamber as well as the buffer chamber are also designed to be smaller to allow for reduced pumping time. However, one major concern for the vertical system is the dropping of material or flakes onto cells and/or the base flange where the band-edge thermometry/pyrometry ports are located. Special chevron shaped shutters, shields, and containers are designed to solve this issue, but more maintenance is still needed compared to horizontal systems.

Both systems have a liquid nitrogen (LN_2) cryo shroud around the substrate for the cooling. Instead of having a single cryo shroud for alcohol cooling to thermally isolate the cells, the GENxplor system's LN_2 shroud is extended between cells to realize the same purpose. As there are increasing demands of LN_2 cooling, the GENxplor uses ~200 L/system/day while the GEN II uses ~160 L/system/day in a normal growth status. The cooling water circuit is utilized in each effusion cell as well as the main chamber loop for regulation and stability in the GENxplor. In comparison, the cooling water circuit is only used for group-V source and the substrate heater in the GEN II. As a result, a total flow of 2.5 to 3.5 GPM is required in the GENxplor, which is more than a ~2 GPM requirement for the GEN II.

Chapter 3 Material Characterization

3.1 X-ray Diffraction

X-ray diffraction (XRD) is one of the most convenient and effective characterization methods for semiconductor materials. It provides useful information about layer thickness, alloy composition, crystalline and interface quality, strain, SL period, and structural defects. X-ray diffraction measurements are nondestructive and do not require device fabrication, yet they can be sensitive to structural deviations of near atomic thickness. The reflectivity of the x-rays is small, enabling x-rays to penetrate deep into the solid materials. Therefore, XRD serves as a bulk probe technique.

3.1.1 Diffraction Condition and Reciprocal Lattice

When radiation strikes a material, scattering and absorption take place. The mechanism for XRD is based on the scattering of x-rays by a crystal material, shown in Figure 3.1. The wavelength of the x-rays ($\lambda \approx 1.54$ Å) is comparable with the spacing of the scattering centers, the crystal's periodic arrangement of atoms (a few Å apart). Strong diffraction occurs when two waves interfere, and the phase difference between them is a multiple of 2π, or the optical path difference is an integer multiple of wavelength. Hence, Bragg's law dictates that diffraction maxima should occur when

$$n\lambda = 2d_{hkl}\sin\theta \qquad (3.1)$$

where d_{hkl} is the spacing between diffracting planes, θ is the incident angle, n is an integer, and λ is the wavelength of the x-rays. Therefore, one can determine the

distance between crystallographic planes based on the Bragg's law with a known incident angle.

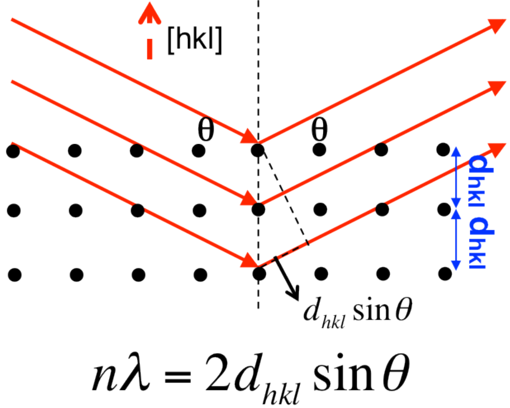

Figure 3.1: Diffraction of a wave off atoms in a crystalline material obeys Bragg's law, $n\lambda=2d_{hkl}\sin\theta$. d_{hkl} is the spacing between diffracting planes, θ is the incident angle, n is an integer, and λ is the wavelength of the x-ray.

In order to consider factors such as intensity and width of XRD peaks, we introduce the concept of a reciprocal lattice, which represents the Fourier transform of the spatial function of the original lattice in real space.

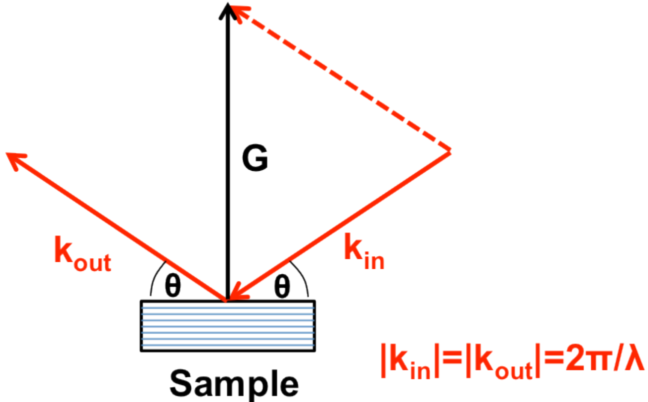

Figure 3.2: X-rays are incident on the sample and scatter back with wavevectors k_{in} and k_{out}, respectively. G is a reciprocal lattice vector.

Consider in the situation shown in Figure 3.2, where x-rays are incident on the sample and scatter back along the directions of $\hat{\mathbf{k}}_{\mathbf{in}}$ and $\hat{\mathbf{k}}_{\mathbf{out}}$, respectively. Because the

scattering is elastic, the magnitudes of wavevectors $\mathbf{k_{in}}$ and $\mathbf{k_{out}}$ are the same, $\boldsymbol{k}_{\mathbf{in}} = \frac{2\pi}{\lambda}\hat{\mathbf{k}}_{\mathbf{in}}, \boldsymbol{k}_{\mathbf{out}} = \frac{2\pi}{\lambda}\hat{\mathbf{k}}_{\mathbf{out}}$. **T** is a lattice vector, which is defined by the primitive vectors for the direct lattice, $\mathbf{a}_1$, $\mathbf{a}_2$, and $\mathbf{a}_3$.

$$\mathbf{T} = n_1\mathbf{a}_1 + n_2\mathbf{a}_2 + n_3\mathbf{a}_3 \qquad (3.2)$$

In order to satisfy Bragg's law and meet the condition of constructive interference, the path difference between the incident and scattered x-rays should be an integer number of wavelengths. That suggests that $(\hat{\mathbf{k}}_{\mathbf{out}} - \hat{\mathbf{k}}_{\mathbf{in}}) \cdot \mathbf{T} = \mathrm{n}\lambda$. By multiplying both sides of the equation above by $2\pi/\lambda$, the diffraction condition can be written as

$$(\mathbf{k_{out}} - \mathbf{k_{in}}) \cdot \mathbf{T} = 2\pi\mathrm{n} \qquad (3.3)$$

The scattering vector is defined as $\Delta\mathbf{k} = \mathbf{k_{out}} - \mathbf{k_{in}}$, and thus $\Delta\mathbf{k} \cdot \mathbf{T} = 2\pi\mathrm{n}$. The Laue conditions for the scattering vector are as follows:

$$\Delta\mathbf{k} \cdot \mathbf{a_1} = 2\pi\mathrm{n}_1 \qquad (3.4.a)$$

$$\Delta\mathbf{k} \cdot \mathbf{a_2} = 2\pi\mathrm{n}_2 \qquad (3.4.b)$$

$$\Delta\mathbf{k} \cdot \mathbf{a_3} = 2\pi\mathrm{n}_3 \qquad (3.4.c)$$

where n_1, n_2, n_3 are integers. This suggests that the scattering vector has to be oriented in a specific directon to meet the diffraction condition.

The real space diffraction conditions are built up from the above equations. To interpret the diffraction conditions in reciprocal lattice, a reciprocal lattice vector **G** is defined. It equals the scattering vector, $\mathbf{\Delta k} = \mathbf{G}$, and therefore satisfies $\mathbf{G} \cdot \mathbf{T} = 2\pi\mathrm{n}$. A reciprocal lattice is formed with the primitive vectors

$$\boldsymbol{b}_1 = 2\pi \frac{\boldsymbol{a}_2 \times \boldsymbol{a}_3}{\boldsymbol{a}_1 \cdot \boldsymbol{a}_2 \times \boldsymbol{a}_3};\ \boldsymbol{b}_2 = 2\pi \frac{\boldsymbol{a}_3 \times \boldsymbol{a}_1}{\boldsymbol{a}_1 \cdot \boldsymbol{a}_2 \times \boldsymbol{a}_3};\ \boldsymbol{b}_3 = 2\pi \frac{\boldsymbol{a}_1 \times \boldsymbol{a}_2}{\boldsymbol{a}_1 \cdot \boldsymbol{a}_2 \times \boldsymbol{a}_3} \qquad (3.5)$$

Points in the reciprocal lattice are mapped by this set of vectors.

$$\mathbf{G} = m_1\mathbf{b}_1 + m_2\mathbf{b}_2 + m_3\mathbf{b}_3 \qquad (3.6)$$

Multiply **G** and **T** from Equation 3.2 and 3.6, the reciprocal lattice vectors built above satisfy the diffraction condition.

$$\mathbf{G} \cdot \mathbf{T} = 2\pi\,(m_1\mathrm{n}_1 + m_2\mathrm{n}_2 + m_3\mathrm{n}_3) \qquad (3.7)$$

With a reciprocal lattice vector $\mathbf{G}_{hkl} = \mathrm{h}\mathbf{b}_1 + \mathrm{k}\mathbf{b}_2 + \mathrm{l}\mathbf{b}_3$, one can prove the following two points mathematically:

1. The reciprocal vector $\mathbf{G}_{\mathbf{hkl}}$ is perpendicular to the real plane (hkl) in the direct lattice.

2. The distance between two adjacent parallel planes in the direct lattice is $d_{hkl}=2\pi/G$.

Based on the first point, the plane (hkl) in real space can be represented by a point (hkl) in reciprocal space. As shown in Figure 3.3, the points form a reciprocal lattice and each point represents a plane in the direct lattice. This concept is crucial for connecting the real-space scan geometry with the diffractograms as well as understanding the properties of symmetric and asymmetric scans. In Figure 3.3, the "Ewald Sphere" is formed with a radius of 2π/λ since the lengths of the incident and scattering vector are the same in elastic scattering. Geometrically, diffraction will occur only for reciprocal lattice points that lie on the surface of the Ewald sphere.

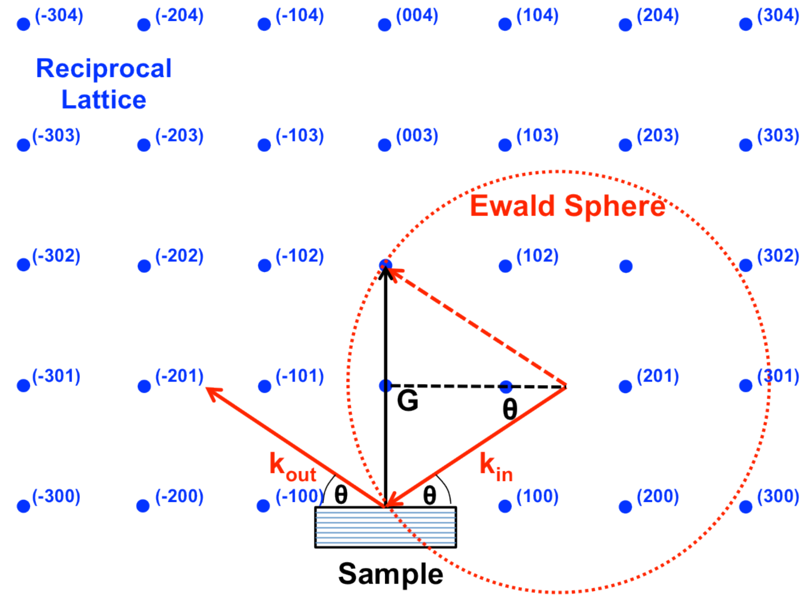

Figure 3.3: The scattering vector and Ewald sphere in the reciprocal lattice. The points are reciprocal lattice points of the crystal, and each point (hkl) in reciprocal space represents a plane (hkl) in real space. Reciprocal lattice points that lie on the surface of the Ewald sphere satisfy the diffraction condition.

We can prove that the diffraction condition in a reciprocal lattice is equivalent to the Bragg's law. Since $\mathbf{G} = \Delta\mathbf{k} = \mathbf{k_{out}} - \mathbf{k_{in}}$, and thus $(\mathbf{G} + \mathbf{k_{in}})^2 = \mathbf{k}_{out}{}^2$

$$\mathrm{G}^2 = 2\mathbf{k_{in}} \cdot \mathbf{G} \qquad (3.8)$$

By replacing G and k_{in} ($d_{hkl}=2\pi/G$, $|\mathbf{k_{in}}| = |\mathbf{k_{out}}| = 2\pi/\lambda$) in the equation, we can prove Equation 3.1, the Bragg's law $\lambda=2d_{hkl}\sin\theta$.

3.1.2 Crystalline Quality and X-ray Scans

The dimensions and perfection of the sample determine the size and shape of each reciprocal lattice point. In the actual diffractions, reciprocal lattice points are volumes instead of points. The following reasons lead to a reciprocal lattice point broadening: finite layer thickness, change in lattice parameter, change in orientation (curvature, tilt), and discontinuities parallel to interface (grain boundaries or island

growth). By providing a quantitative value of the size of the reciprocal lattice point, the full width at the half maximum (FWHM) of a peak in the XRD scan is a good indicator of the crystalline quality.

Figure 3.4 (a) shows representative XRD scans of two identical IC laser structures with different material qualities at the 004 reflection, which serves as a good example of the peak broadening in such structures. R087 and R088 are InAs-based IC laser structures grown on InAs substrates with an identical layer sequence (shown in Figure 3.4 (b)), but with different InAs growth rates in the waveguide region (the InAs layers that sandwich the cascade stages). The higher InAs growth rate of 0.66 ML/s in R087 leads to a rougher surface compared to the InAs layers grown at 0.22 ML/s in R088 [92], and thus results in a rough initial surface for the active region and strongly affects the material quality of the laser. AFM measurements characterized the significant difference in surface morphology, as shown in Figure 3.4 (c) and (d). R087 has a rougher surface with a root mean square (RMS) roughness of 1.0 nm, while R088 has a smoother surface with a RMS roughness of 0.2 nm. According to the XRD data, the center peaks of R087 are much broader than those of R088. For example, the FWHM of the first peak on the right side of the substrate peak is 920 arcsec and 55 arcsec for R087 and R088, respectively. The broadened satellite peaks of R087 indicate an inferior active region quality compared with R088. Since XRD is a bulk probe technique, it provides useful bulk information, which can also affect the surface morphology.

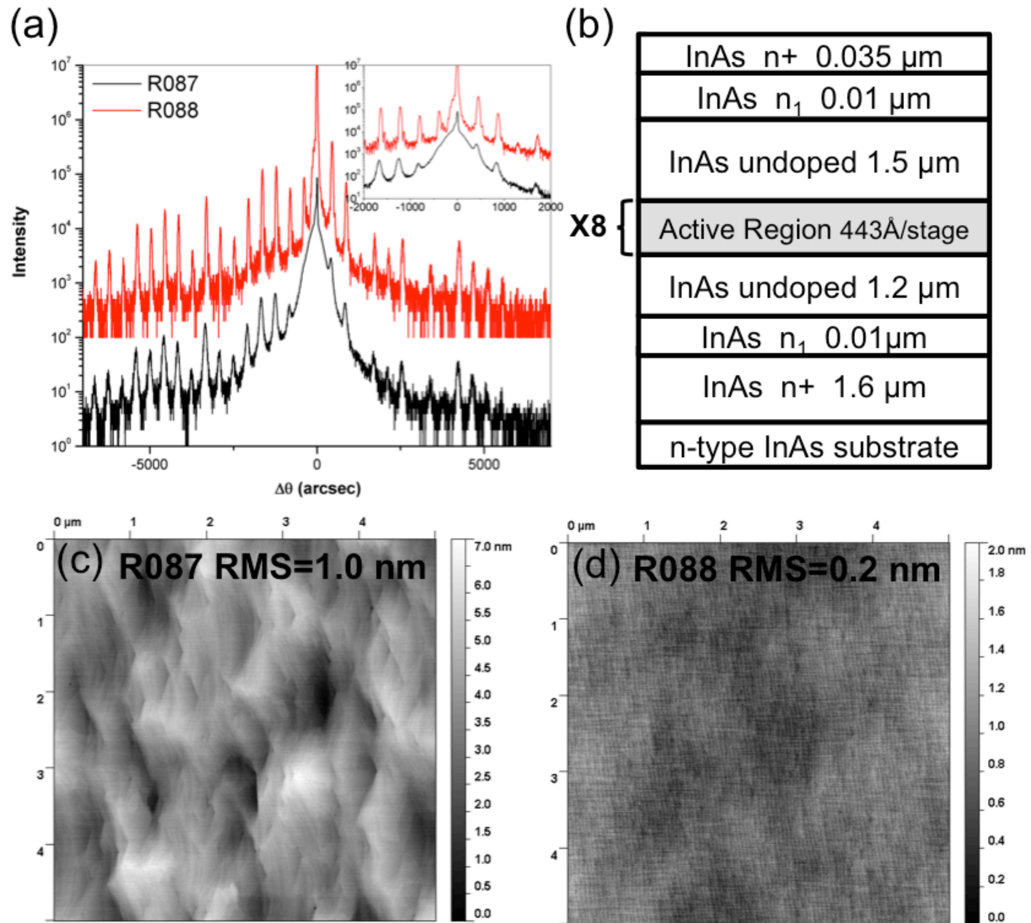

Figure 3.4: Material characterization of IC lasers structures R087 and R088 by XRD and AFM. (a) X-ray diffraction data for ω-2θ scans around the 004 reflection of R087 (lower) and R088 (upper). The inset shows the scan data near the substrate peak. (b) The schematic laser sequence of R087 and R088. (c), (d) AFM images taken from the surfaces of R087 and R088 over a 5 μm × 5 μm area, respectively.

While XRD can provide useful information, there are also limitations in the measurements, as minor differences are hard to discern even if the differences are observed in a microscopic characterization; the IC laser structure R089 is a prime example. Due to the non-uniformities in the growth, low and high defect regions appeared in the same half of the 2-inch wafer. The DIC microscopic images are shown in Figure 3.5 (c) and (d). The low defect area has a defect density of $\sim 1\times10^4$ cm^{-2} with a size from 3 to 30 μm based on the DIC microscopy count, while the high defect area

has a defect density of ~1×10^6 cm^{-2} with most of the defects smaller than 10 μm. The large defects, which appeared in both regions, are oval shaped hillocks elongated along the primary flat in the $[-110]$ direction with a polyhedral pit in the center. This kind of defect is similar to the so-called oval defects found in III-V crystalline materials grown by MBE [93-96]. A detailed study was carried out on InAs homoepitaxial layers and is discussed in Section 4.1.3 [92]. That study suggested that the defects originated at the substrate surface as a result of several possible reasons, such as surface contamination by particles in the laboratory environment, indium clusters and residual oxide on the substrate, and defects intrinsically existing in the substrates; however, the smaller defects shown in the high-density area do not have a pit in the center, and thus may have different formation mechanisms, which is still unclear. Based on the observation that they only appeared in a certain region on the wafer, they may result from a non-uniform substrate temperature in the sample holder.

In order to study the non-uniformities, XRD measurements were carried out in the high and low defect areas of the quarter of the 2-inch wafer as shown in Figure 3.5. (b), where the boundary of the two regions is marked by a dashed line. The size of the x-ray beam is about 6 mm × 1.1 mm at the scanned angle (indicated by the long black and red rectangular shapes in Figure 3.5 (b)), and thus the data will be able to represent the specific area. The scans are shown in Figure 3.5 (a). The average satellite peak separation is measured and leads to a calculated SL period of 45.4 nm for both areas. The FWHMs of satellite and substrate peaks are listed in Table 3.1. The differences between the two scans are so small that they are within the experiment error. This suggests that the XRD measurements are not sensitive to the morphology

differences shown in the DIC microscopies on the same wafer (Figure 3.5 (c) and (d)). It is possible that the defects start on the top surface of the wafer and thus do not affect the bulk material quality. Further studies are needed to show the origin of these small defects in the high defect area, and will help understand the limitations of XRD measurements.

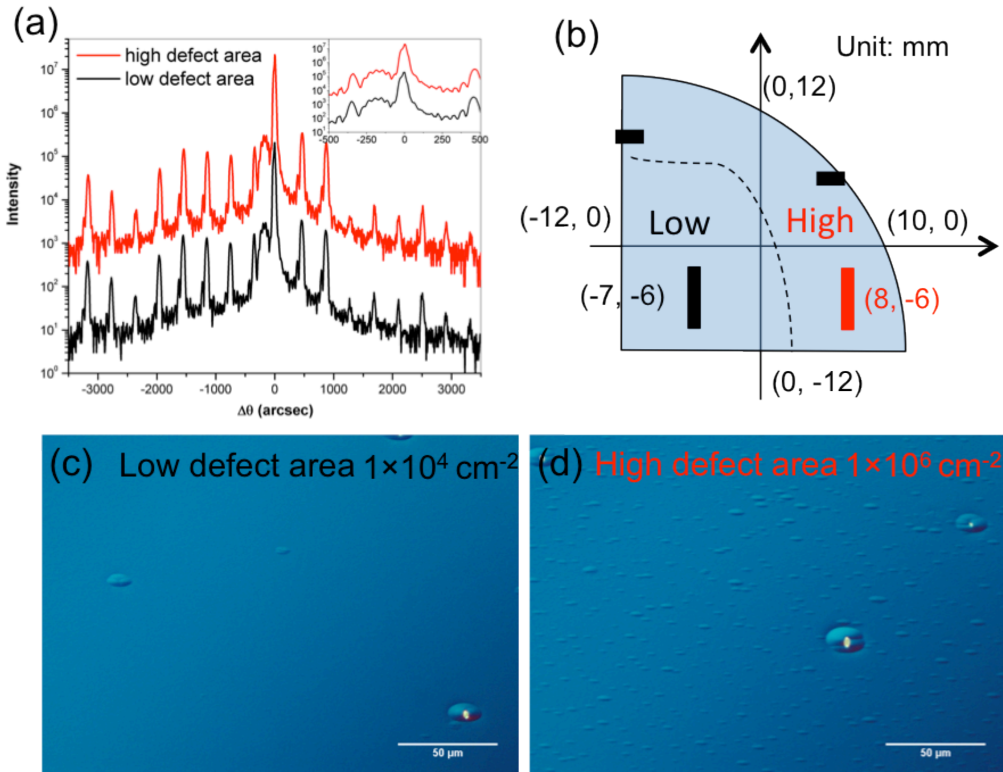

Figure 3.5: Material characterization of different areas on IC laser structure R089 by XRD and DIC microscopy. (a) X-ray diffraction data for ω-2θ scans around the 004 reflection of R089 at areas of high (lower) and low (upper) defect density. The inset shows the scan data near the substrate peak. (b) A schematic of the quarter of the 2-inch wafer, where the dashed line indicates the boundary between high and low defect areas. The long rectangular spots indicate the regions intersecting the x-ray beam for the two scans. Numbers in parentheses are the coordinate on the wafer. (c), (d) DIC microscopy images taken from the area of the low and high defect density on the surface of R089, respectively.

Table 3.1: X-ray diffraction data for two ω-2θ scans of R089 at the area of high and low defect density.

Scan	Average of satellite peaks separation (arcsec)	Period (Å)	FWHM of peaks (arcsec)					
			-3rd	2nd	-1st	0-sub	1st	2nd
High defect area	405.7	454.3	50	46	39	25	50	49
Low defect area	405.6	454.4	45	48	37	26	49	49

3.1.3 Experimental Procedures in XRD Scans

The HRXRD results discussed in this dissertation were carried out using a Philips HR- 2 High Resolution Diffractometer with a four reflection Ge (220) incident beam monochrometer and an incident beam power of 1200W, corresponding to an unobstructed beam-to-detector count rate of about 600,000 counts/second, and a minimum FWHM resolution of 14 arcsec. All the scans and sample alignments were controlled using Philips PC-MRD software. The minimum step size for Omega (ω) and 2Theta (2θ) are 0.00025° and 0.001°, respectively. The incident x-ray wavelength is λ=1.54059Å, corresponding to the CuKα1 transition [97].

The quality of data collection using the PC-MRD software depends not only on the correct choice of hardware options, but also on the correct choice of parameters within the scan program. A schematic diagram of the XRD unit is shown in Figure 3.6 with both a side view and a plan view. The system goniometer consists of a base plate, and co-axial 2theta (2θ) and omega (ω) drives attached to detector and sample stages, respectively. The sample stage can be rotated about a horizontal axis by using a psi (ψ) axis motor so that the [001] direction is in the diffraction plane that defined by the incident beam and diffraction beam (as well as the plane of the detector and the x-ray

gun in the system). Moreover, the sample stage can be rotated about the surface normal by using the phi (ϕ) axis motor. X and Y movements are also available to move the sample stage relative to the incident beam so that the data can be collected from different areas of the sample. As shown in Figure 3.6 (b), the angle between the incident beam and the sample surface is defined as omega (ω), and the angle between the incident beam and the diffracted beam is defined as 2theta (2θ).

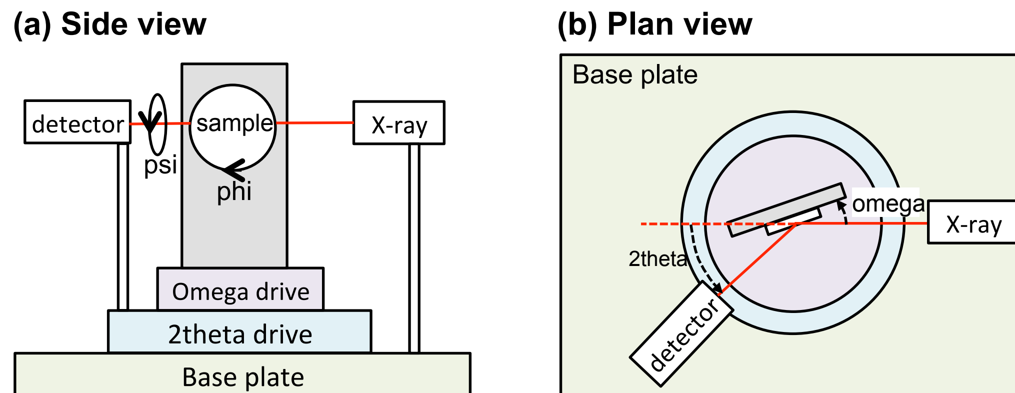

Figure 3.6: A schematic diagram of the XRD unit in (a) a side view and (b) a plan view.

In the experiments, the most commonly used scan is the ω scan, where the detector is fixed at a certain position while the ω angle is varied. Since the detector acceptance angle is about 2°, only 1° of the ω-scan can be collected by the detector. In the ω-2θ scan, the 2θ drive is moved at double the angular speed of the ω drive, and thus the ω-2θ scan can be used when a longer scan range is required.

There are three main steps needed for recording an ω or an ω-2θ scan: find the peak, optimize the scan direction, and collect the intensity data. In the first step, positions of ω and 2θ for the peak are calculated based on the material parameters

stored in the program. However, there will be a small difference between the actual ω position of the reflection and the calculated value. The main reason is the sample mounting, which may not exactly be parallel to the sample stage. Other reasons include a tilt between the substrate and epilayer, lattice parameter deviation from the assumed value, and experimental errors in goniometer position. A quick ω scan of 3° is used for the peak search. The actual ω value of the substrate peak is used to align the sample and the detector.

The second step is crucial to ensure that the scan is made through the center of the reciprocal lattice point. The optimization process is achieved by finding the ψ angle where a maximum intensity is collected across a minimum width. A series of short ω scans are made at different ψ angles. A PC-MRD ψ -optimizing program can be written to automatically collect and calculate the optimizing ψ according to a seven-point parabolic fit. In order to determine the true peak maximum, the ω step size has to be reduced to 0.001°. ω-scan steps of $\leq \sim 20\%$ of the minimum expected half width are recommended to accurately estimate the peak intensity. With this procedure, it is usually adequate to have the reflecting plane perpendicular to the diffraction plane.

The last step is to record the intensity data, usually by an ω scan or an ω-2θ scan, depending on the scan range. A continuous scan is preferred rather than a step scan, since it records an average intensity over each step and may find peaks which are narrow compared to the step width. Scan step and scan time are determined according to the measurement purpose. If the purpose of the scan is to measure the widths and separations of intense peaks, a small step size and short count time per step can be

used. If the purpose is to study low-intensity fringes, the count time must be longer and the maximum step size should be determined by the fringe spacing [98].

3.1.4 Strain Calculation

If the purpose of the scan is to determine the material composition and strain of the epitaxial layers, the measurement and analysis can be complicated. Let's first consider the tilt between layers and the substrate. Tilt between the surface planes of an epitaxial layer and the equivalent crystallographic planes in the substrate can result from growth on an off-axis substrate and tilting introduced by mismatch dislocation networks [98]. Since the two set of planes are no longer parallel, a shift of the layer peak relative to the substrate peak will appear. The shift will vary with the direction of the incident beam relative to the substrate. Therefore, the three steps described in the last section would not be sufficient for the calculation. A separate scan is needed by rotating the sample 180° about the ϕ axis. The splitting due to lattice mismatch can be calculated by averaging the two measurements [99].

$$\delta\theta = (\delta\theta_0 + \delta\theta_{180})/2 \qquad (3.9)$$

where $\delta\theta_0$ and $\delta\theta_{180}$ are the splitting measured at two ϕ angles 180° apart. Then the lattice difference of the substrate and epilayer in the direction of normal to the substrate, δd, can be calculated through the equation

$$\frac{\delta d}{d} = -\delta\theta \cot\theta \qquad (3.10)$$

where θ is the substrate's theoretical omega value, d is its lattice spacing.

To calculate the tilt angle, several scans are needed at ϕ*, ϕ*+90°, ϕ*+180°, and ϕ*+270°, where ϕ* is an arbitrary value of ϕ. The details of measurement and calculation can be found in reference [98].

In the measurement of material composition, one has to take strain and relaxation into consideration, since a thick mismatched layer beyond the critical thickness will partially relax. Figure 3.7 shows the changes of the epilayer unit cell when relaxation takes place for (001) wafers. In a partially relaxed situation, the unit cell in-plane width "a" is no longer the same as the one in the substrate "a_s". A symmetric scan (such as the 004 reflection) will measure unit cell thickness in the growth direction "c", and an asymmetric scan (such as the 115 reflection) has to be measured in addition to evaluate "a" of an epilayer. Then the bulk cubic lattice parameter for the epilayer can be calculated from the equation:

$$a_L = c\left(1 - \frac{2\nu}{1+\nu} \cdot \frac{c-a}{c}\right) \qquad (3.11)$$

where ν is Poisson's Ratio for the layer (about 1/3 for III-V materials).

The mismatch (m) of a heteroepitaxial layer is defined by

$$m = \frac{a_L - a_s}{a_s} \qquad (3.12)$$

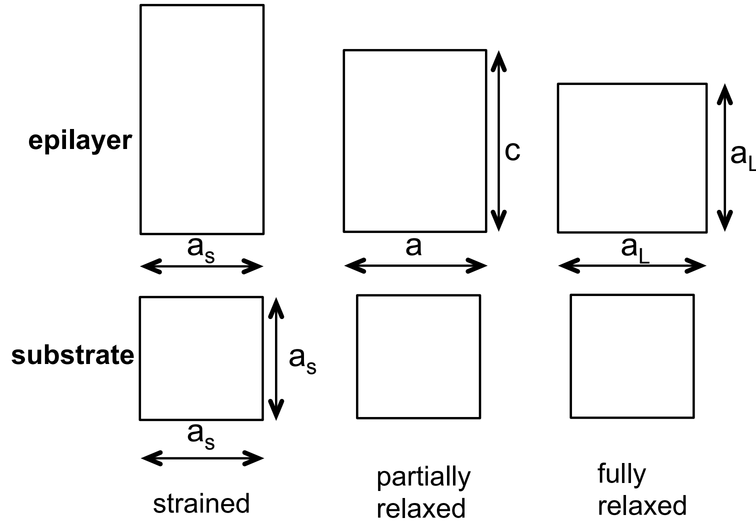

Figure 3.7: Change of the epilayer unit cell with relaxation in (001) wafers.

3.1.5 XRD Measurement of IC Structures

In Section 3.1.2, we discussed how XRD scans can help analyze the crystalline quality based on the peak FWHMs in the IC structures. In this section we focus on the periodicity and strain information that can be extracted from the XRD scans.

The IC structures contain repeated quantum well structures in the design. ICPDs utilize InAs/GaSb SLs as absorbers, which usually have hundreds of periods, each with a thickness of ~5 nm. IC lasers have a quantum engineered cascade stage, which is repeated for ~10 times with a period of 50 nm. The periodic structures have a corresponding set of points in reciprocal space, which will be extended into rods due to the limited thickness nature of the layers. A smaller period in the real space corresponds to a larger separation of reciprocal lattice points. Therefore, the satellite separations in ICPD structures (~1.0°) are much larger than that in IC lasers (~0.1°). The positions of the satellite peaks are no longer determined solely by the composition of an alternating layer, but also by the SL period. The position of the zero order peak

(which is usually stronger than the other satellite peaks) corresponds to the average lattice parameter (composition) of the SL. The intensity and width of the satellite peaks are affected mainly by the number of periods or the total thickness of the SL structure, the sharpness and grading of the interface, and the thickness or period dispersion.

The strain in the structure can be estimated by the position of the zero order peak. The measurement for an ICPD structure is straightforward as the satellite peaks are separated far apart enough to identify the zero order peak. Figure 3.8 (a) gives an example of an ω-2θ scan at the 004 reflection of ICPD R120. The substrate and zero order peak are marked in the figure. There are repeated InAs/GaSb SLs with a period of ~6.2 nm. In order to estimate the effect of a tilt angle in the structure, ω-2θ scans were measured at ϕ^*, $\phi^*+90°$, $\phi^*+180°$, and $\phi^*+270°$, where ϕ^* is an arbitrary value of ϕ. The scans around the substrate and zero order peaks for the four ϕ^* values are plotted in Figure 3.8 (b). The ω value, FWHM and distance between the two peaks are listed in Table 3.2. An extra measurement at ϕ^*, listed in the 5th row in Table 3.2, was made after remounting the sample and realigning. The difference of the peak splitting in the two measurements (number 1 and 5 in Table 3.2) is about 4%, which is a measure of the experimental error in the measurement. Moreover, the peak splitting of four measurements made at different ϕ angles are within the experiment error. By using the equations in [98] and the collected ω values at different ϕ angles, the tilt between the substrate plane and the mounting stage was determined to be 0.75°, and the tilt between the substrate plane and average epilayer plane is 0.002°. These tilt values may not be precise due to the possible experimental error. However, they

suggest that the tilt is so small that it will not affect the calculation of mismatch in this ICPD structure.

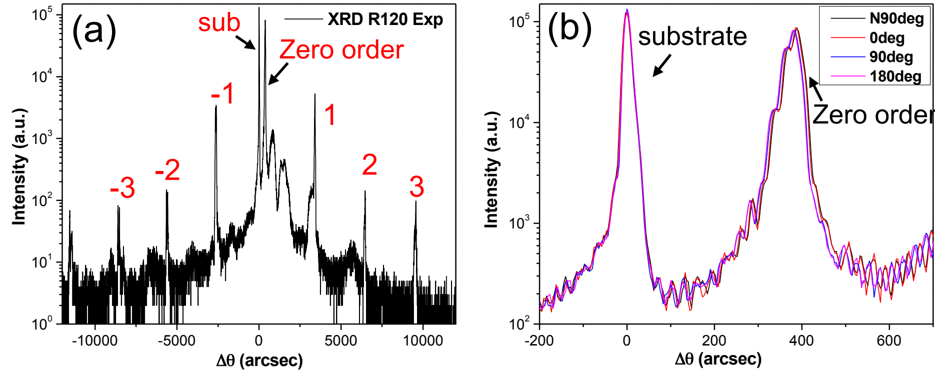

Figure 3.8: (a) X-ray diffraction data for R120 for ω-2θ scans around the 004 reflection at φ* and (b) the scan comparison of scans at φ*, φ*+90°, φ*+180°, and φ*+270° (φ-90°).

Table 3.2: X-ray diffraction data of R120 for five ω-2θ scans of R120 at φ*, φ*+90°, φ*+180°, φ*+270° (φ-90°), and φ* with different alignments.

	Phi (°)	Substrate (°)		0th order peak (°)		separation		Perpendicular mismatch
		omega	FWHM	omega	FWHM	° degree	arcsec	
1	0	29.6815	0.0050	29.7892	0.0113	0.1077	388	-0.321%
2	90	30.6209	0.0046	30.7266	0.0114	0.1057	380	-0.315%
3	180	30.8532	0.0049	30.9582	0.0114	0.1050	378	-0.313%
4	270	29.6787	0.0053	29.7867	0.0113	0.1080	389	-0.322%
5	0*	30.2470	0.0049	30.3505	0.0117	0.1035	373	-0.308%

Since the data were taken from a symmetric scan at the 004 reflection, the zero order peak position indicates the average lattice parameter in the growth direction "*c*". Therefore, $c = \delta d$ from Equation 3.10. Then the perpendicular mismatch equals to

$$m_p = \frac{c - a_s}{a_s} \qquad (3.13)$$

The perpendicular mismatch calculated with measurements at different ϕ angles equals -0.32%, and details are listed in Table 3.2. The mismatch is relatively large compared to most of the IC structures grown at OU. If the SL is fully strained, $a=a_s$, then from Equation 3.11, 3.12, and 3.13, the mismatch can be calculated as follows,

$$m = m_p \left(\frac{1-\nu}{1+\nu}\right) \approx \frac{1}{2} m_p \qquad (3.14)$$

since Poisson's Ratio ν is about 1/3 for III-V materials. Because an accurate Poission's Ratio of the SL is unknown, it is preferred to use perpendicular mismatch m_p in the XRD measurement of an IC structure.

Another example is given to explore how the tilt angle will affect the FWHMs of the satellite peaks and the periodicity of the SL. We continue the study in Section 3.1.2 of structure R089 by comparing the scans at ϕ*, ϕ*+90°, ϕ*+180° for the high defect region. Figure 3.9 plots ω-2θ scans around the 004 reflection at these ϕ angles as well as two additional scans of the low defect region with different alignments. The substrate ω values, FWHMs of satellite peaks, and deduced periods are listed in Table 3.3. The two scans with different alignments show a small experimental error in both period and FWHM (which is not an accurate measure of the error but yield an estimate). The average satellite peaks separations are very close to each other and lead to a ~1% difference in deduced period in the three scans taken at ϕ*, ϕ*+90°, ϕ*+180°. The differences in FWHMs are also within the experiment error (~3 arcsec). Even though the structures have a slightly off-axis substrate (0.35° for both InAs and GaSb substrates) and a noticeable amount of mismatch (perpendicular mismatch ~0.3% for

R120), the tilt between epilayers and substrate is so small that it has a negligible effect on the XRD measurements of the IC structure.

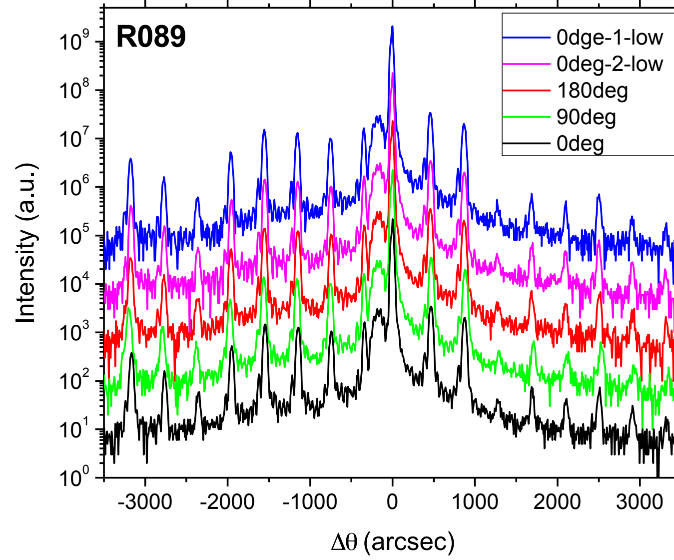

Figure 3.9: X-ray diffraction data for ω-2θ scans around the 004 reflection at ϕ*, ϕ*+90°, ϕ*+180° for a high defect region of R089, and at ϕ* in two alignments for a low defect region.

Table 3.3: X-ray diffraction data for ω-2θ scans of R089 at different regions, ϕ angles, and alignments.

Scan	Phi (°)	sub peak (°) omega	Average of satellite peaks separation (arcsec)	Period (Å)	FWHM of peaks (arcsec)					
					-3rd	2nd	-1st	0-sub	1st	2nd
1-High defect area	0	30.5436	405.7	454.3	50	46	39	25	50	49
2-High defect area	90	30.5523	409.0	450.6	48	49	39	24	50	51
3-High defect area	180	30.4103	407.0	452.2	49	46	40	23	50	50
1-Low defect area	0	30.5504	405.6	454.4	45	48	37	26	49	49
2-Low defect area	0	30.5657	405.7	454.4	48	47	36	24	50	50

Compared to the mismatch calculations for ICPDs, it is more complicated to deduce the mismatch for ICL structures from the XRD scans. There is a large uncertainty in the estimate of the mismatch, which arises from the criteria used to identify the zero order peak in the repeated structures. IC laser structure R088, which was discussed in Section 3.1.2, is a good example. The designed structure of R088 is shown in Figure 3.4 (b), and contains 8 cascade stages with a period of 44.3 nm. The repeated cascade stages have a series of satellite peaks with an average separation of 419.4 arcsec (0.1165°) in the experimental scan shown in Figure 3.10. The deduced period is 44.5 nm and 0.4% larger than the designed value. As shown in Figure 3.10, the experimental scan shows a good agreement with the simulation of R088 (using the designed parameters in a commercial XRD simulator (X'pert Epitaxy)) in both peak position and satellite intensity. The good agreement leads us to believe the grown structure is very close to the designed one, and thus the zero order peak should be the one that is the closest to the substrate peak, providing the lowest mismatch value. As shown in Figure 3.10, the zero order peak is submerged in the high intensity substrate peak, and should be around 30 arcsec based on the average separation between right and left peaks (indicate by the blue arrow). It suggests an in-plane tensile strain with a perpendicular mismatch of -0.025%.

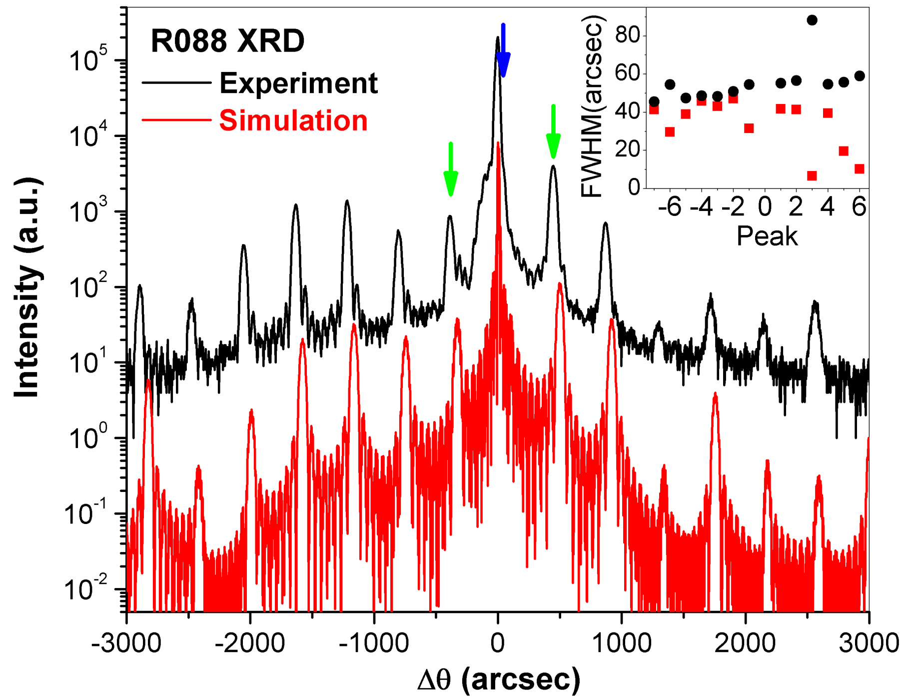

Figure 3.10: X-ray diffraction data (upper) and a corresponding simulation (lower) for an ω-2θ scan around the 004 reflection of R088. The inset shows the FWHMs of satellite peaks around the substrate peak.

However, in many of our structures the experimental scan does not match well with the simulation due to the variation in MBE growth, and there is no strict criterion to identify the zero order peak. In fact, the satellite peaks are not always symmetric from the center peaks, and the zero order peak is not always the one with the highest intensity, or closest to the substrate peak. In that case, how does one determine the zero order peak? Is it possible that the zero order peak is the peak that is the next closest to the substrate peak (indicated by the green arrow in Figure 3.10)? We tried to compare the FWHMs of the satellites in the experimental and the simulation scans in the inset of Figure 3.10, hoping to find the zero order peak by carrying out a

polynomial fit as suggested in Ref.[100]; however, the FWHMs in both scans show neither a strong dependence of the peak position, nor an agreement between them.

In this work, we use the Matthews-Blakeslee critical thickness criteria [101] of a mismatched heteroepitaxial layer as a reference to help narrow down the answer. The narrowness of the satellite peaks implies that the IC structure is close to being fully strained. And this is consistent with the absence of a cross-hatch morphology in DIC micrographs. Therefore, if we assume the structure is fully strained, then the position of the zero order peak should be consistent with a Matthews-Blakeslee critical thickness that is equal to or larger than the length of the cascade stages (*i.e.* the length of the cascade stages of R088, 8 × 44.3 nm = 354.4 nm).

The Matthews and Blakeslee model [102, 103] is used to calculate the critical thickness for hereroepitaxy. Here we follow the calculation in Ref. [101]. Once the epilayer is thicker than the critical thickness, a preexisting threading dislocation in the substrate replicates in the growing epilayer and can bend over to create a length of misfit dislocations in the interface. The glide force acting on a dislocation is given by

$$F_G = \frac{2Gb\varepsilon h(1+v)cos\lambda}{1-v} \quad (3.15)$$

where b is the length of the Burgers vector for the threading dislocation, h is the layer thickness, G is the shear modules and has been assumed to be equal for the epitaxial layer and the substrate, ε is the strain and equals the mismatch m, and λ is the angle between the Burgers vector and the line in the interface plane that is perpendicular to the intersection of the glide plane with the interface. The line tension of the misfit segment of the dislocation is given by

$$F_L = \frac{Gb(1-v\cos^2\alpha)}{4\pi(1-v)}\left[ln\left(\frac{h}{b}\right)+1\right] \qquad (3.16)$$

where α is the angle between the Burgers vector and the line vector of the dislocation. When the epilayer thickness is smaller than the critical thickness, the threading dislocation is stable, as the glide force cannot overcome the line tension. When the layer is thicker, threading dislocation will glide to create a misfit dislocation to relieve the strain. Thus, the critical thickness h_c is solved by equating the glide force for the line tension for the segment of the dislocation.

$$h_c = \frac{b(1-v\cos^2\alpha)}{8\pi|m|(1+v)\cos\lambda}\left[ln\left(\frac{h_c}{b}\right)+1\right] \qquad (3.17)$$

In the calculation of the critical thickness on an InAs (001) substrate, $\cos\alpha = \cos\lambda = 1/2$, $b = a/\sqrt{2}$, with "a" equal to the InAs lattice constant. This corresponds to 60° dislocations on $a/2\langle 110\rangle\{111\}$ slip system [101]. Note that the calculation is different from the original publication [103], where the maxima $\varepsilon = \frac{1}{2}m$ in Equation 3.15, and the critical thickness is defined at a condition, $F_G = 2F_L$. Thus, the critical thickness is 4 times thicker in Ref. [103] than in Ref. [101].

In Figure 3.10, the positions of left and right second-closest satellite peaks are -386 and 445 arcsec, and the corresponding perpendicular mismatch is about 0.32% and -0.36%, respectively. Based on the above calculation [101], the critical thickness is respectively 93 and 82 nm for a threading dislocation to propagate in a heteroepitaxial layer. Moreover, it has been found that SL structures have a larger Matthews-Blakeslee critical thickness compared to a single heteroepitaxial layer. This is because a SL structure can help prevent mismatch dislocations from propagating

and eliminate relaxation. In a previous experiment [104], 3.3 μm AlSb/InAs SLs were grown on a GaSb substrate, and are fully strained with a strain range from zero to at least 0.08% [104]. The Matthews-Blakeslee critical thickness of a heteroepitaxial layer with 0.08% mismatch is calculated to be ~210 nm. Therefore, it suggests that a fully strained SL was grown to a thickness larger than the Matthews-Blakeslee critical thickness by a factor of 15 (3.3 μm / 0.21 μm ≈ 15). Assuming the quantum well structures in the cascade stage have a similar tolerance, the thickness, below which the cascade structure can be grown fully strained, is respectively 1.40 and 1.23 μm for situations where left and right second-closest satellite peaks are considered to be the zero order peak. These thicknesses are still larger than the total thickness of the cascade stages (354.4 nm). Therefore, if we identify either of these two peaks as the zero order peak, a fully strain situation could still be expected. Similarly, Table 3.4 lists the calculated critical thickness values of satellite peaks that are close to the substrate peak. Compared to the total length of the cascade stages of 354 nm in R088, choosing the satellite peak at 869 or -801 arcsec as zero order peak would still be possible to meet the fully strained criteria. In conclusion, by using the fully strain assumption and Matthews-Blakeslee critical thickness calculations, we have five possible satellite peaks that could be set as the zero order peak. Thus there is a large uncertainty in determining the mismatch in IC lasers when a good match to simulation is absent.

Table 3.4: Matthews-Blakeslee critical thickness of mismatched layers. The mismatch is deduced by assuming a satellite peak close to the substrate peak is the zero order peak in R088.

	0	+1	-1	+2	-2	+3	-3
Position (arcsec)	30	445	-386	869	-801	1294	-1218
Perpendicular mismatch	-0.025%	-0.36%	0.32%	-0.71%	0.66%	1.06%	1.00%
Critical thickness (nm)	1710	82	93	36	39	22	23
15×Critical thickness (μm)	25	1.23	1.40	0.54	0.59	0.33	0.34

3.2 Atomic Force Microscopy

Atomic force microscopy (AFM) is a widely used technique in science and engineering fields due to its ability to provide quantitative sub-nanometer resolution in measuring surface morphology. By tracking the movement of the scanner in the z-direction, while raster scanning in the x- and y-directions, AFM measures the height information and thus provides a three-dimensional image of the surface. Note that AFM can be used for a variety of purposes, *e.g.* it was recently used to study the voltage drop and electric field over an IC laser based on scanning voltage microscopy [105]. In this section, we focus on AFM measurements of material surface morphology, which has been extensively used in our project.

3.2.1 Principle and Microscope Architecture

Figure 3.11 is simplified schematic of an AFM system [106]. A light source (laser or LED) provides focused light onto a very sharp tip, attached to the end of a cantilever, as shown. The light is reflected off the backside of the cantilever and collected by a position sensitive detector. As the surface structure changes, the tip position will change and so will the defection or amplitude signal from the position sensitive detector. The signal is digitized, recorded and fed back to the control mechanism. The Z stage responds to the feedback and moves up and down to keep the signal the same. Thus, a Z distance motion is recorded per X,Y point and a three-dimensional image is produced.

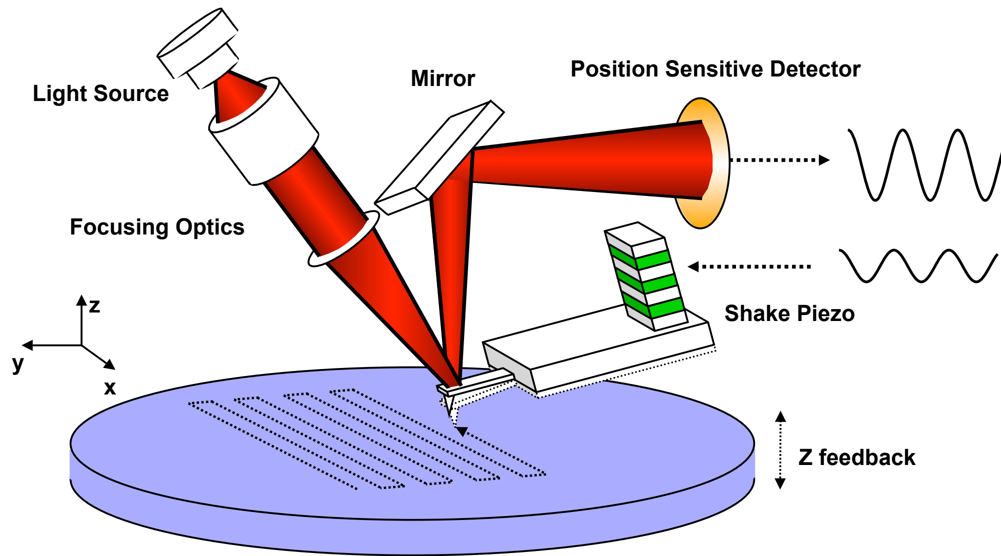

Figure 3.11: Simplified schematics of an AFM system [106].

The AFM results discussed in the paper were carried out using an Asylum Research MFP-3D AFM system. The MFP-3D ARC2 controller enables various imaging mode, such as Contact, Constant Force, Non-contact, AC (intermittent contact), Dual AC, and Force Spectroscopy. The scanning system has a closed-loop operation with position sensors in three axes, and each axis of motion is independently actuated by its own piezo stack and flexure stage. The tip can travel 90 µm in the X and Y direction, while the Z motion can scan over 15 µm. In addition to the Z piezo voltage signal (height), a closed-loop sensor, Z sensor, measures Z distances by monitoring how much the flexure plates move in response to the piezo moving. The Z sensor is linear in the measurements and is more accurate in measuring distance (especially >200 nm) compared to the Piezo (height) voltage signal due to the creep, hysteresis and non-linearity issues of the actuators [106]. The system utilizes an infrared superluminescent diode (SLD) as the light source with a wavelength of 860 nm and a focus spot of 10 to 50 µm. The SLD is incident on the cantilever at a 22°

angle to the sample normal. This inverted SLD path reduces interference problems due to laser retro-reflections [107].

A silicon cantilever (Asylum Research AC160TS-R3) was used in the scanning, with a resonant frequency of 300 (200-400) kHz and a spring constant of about 26 (11-54) N/m. The top of the cantilever is coated with Al to improve the reflectance of the laser light. The radius of the tip is 9±2 nm, and note that features smaller than this radius will be enlarged in the image (> 9 nm).

There are three main modes commonly used for the AFM image: contact mode, non-contact mode, and intermittent-contact (or tapping) mode. Figure 3.12 shows the operation regimes in the force verses distance curve for the different scanning modes. In the contact mode, the tip makes hard contact with the sample, and thus the force between the cantilever and the sample is repulsive. While the tip is raster-scanned across the surface, the deflection is monitored and maintained constant. In the non-contact mode, the tip is close to the sample, but not touching, and the force is an attractive van der Waals force. Instead of keeping static, the tip oscillates at or slightly above its resonant frequency. The oscillation amplitude (typically <10 nm) and frequency is sensitive to the force, and thus the topographic image is constructed by scanning the tip above the surface and keeping an average tip-to-sample distance. Scanning in non-contact mode involves much reduced lateral forces and little sample damage compared to scanning in contact mode. However, the attractive forces from the sample are substantially weaker than the forces used by the contact mode and lead to lower resolution. Intermittent-contact mode (or tapping) is an advanced method of imaging achieving high resolution without inducing destructive force. By using a

higher oscillation amplitude (typically ~100 nm) than that in the non-contact mode, the interaction between tip and sample involves both attractive and repulsive regimes. Changes in the oscillation of the cantilever are normally detected by measuring the variation in the amplitude and used as the feedback input signal. The tapping nature enables the tip to pass through contaminated, soft, and/or rough surfaces, because the oscillating amplitude is larger and accommodates greater variations in height more easily [108].

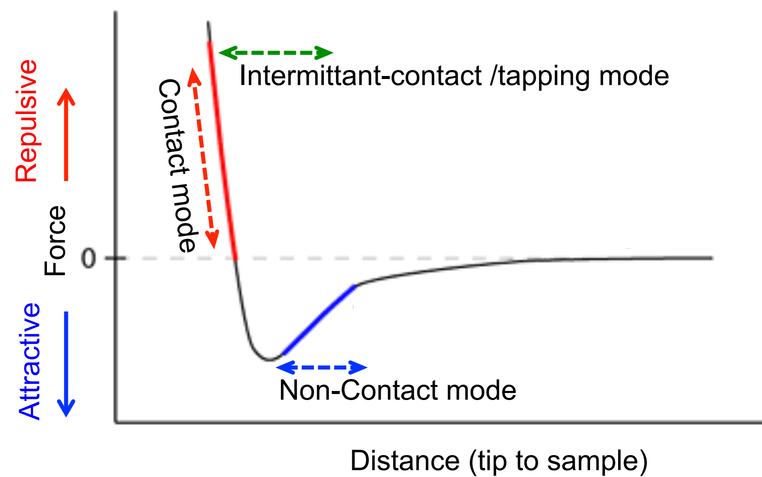

Figure 3.12: Interatomic force verses distance (tip to sample) curve. The operating regimes of the different scanning modes are shown.

The measurements are carried out with the Asylum Research Igor program in AC mode. A thermal tune is performed to determine the nature resonant frequency of the cantilever. The important parameters in imaging are: Scan Rate, the frequency used to complete a trace-retrace cycle; Set Point Voltage, the voltage the feedback tries to maintain; Internal Gain, which controls how fast the feedback system reacts to the error signal; and Drive Amplitude, the amplitude of the drive signal that goes to the piezo that drives the cantilever. To improve the tracking on a surface, one

decreases the Set Point Voltage and increases the amount of Drive Amplitude, which increases the force applied to the sample. Tuning is usually operated in either repulsive mode or attractive mode, so that "mode hopping" between net repulsive forces and attractive forces is avoided.

3.2.2 AFM of Surface Morphology

We give an example of AFM scans on ICPD structure R120 in Figure 3.13. The scan size is 2 μm × 2 μm, with 512 points in each line and a scan rate of 1 Hz, and thus, the scan speed was 5 μm/s. The scan angle is set to 45° so that the step lines in the structure are also along ~45° direction to provide good resolution. The amplitude setpoint voltage is 511.49 mV and the drive amplitude is 25.76 mV. The drive frequency is 308.36 kHz. Integral gain is 10.435. Figures (a) and (b) show the surface image in height trace and retrace, respectively. Because each scan line does not exactly overlap, the two images can be slightly different. The similarity of the two images, *i.e.* the same shape of the small features without directional tails, suggests a good tracking of the tip on the sample. The measured retract amplitude was around 56 nm and the retrace phase was about 108±2° (Figure 3.13 (c) and (d)), suggesting the scan was in the attractive regime. The Z Sensor signal shown in Figure 3.13 (e) has less detail in the image because it is not as sensitive when the distance is less than 40 nm. The images in the different channels show changes of scanning components and parameters regarding the features on the sample. The height information from (a) and (b) are the most commonly used to determine surface morphology.

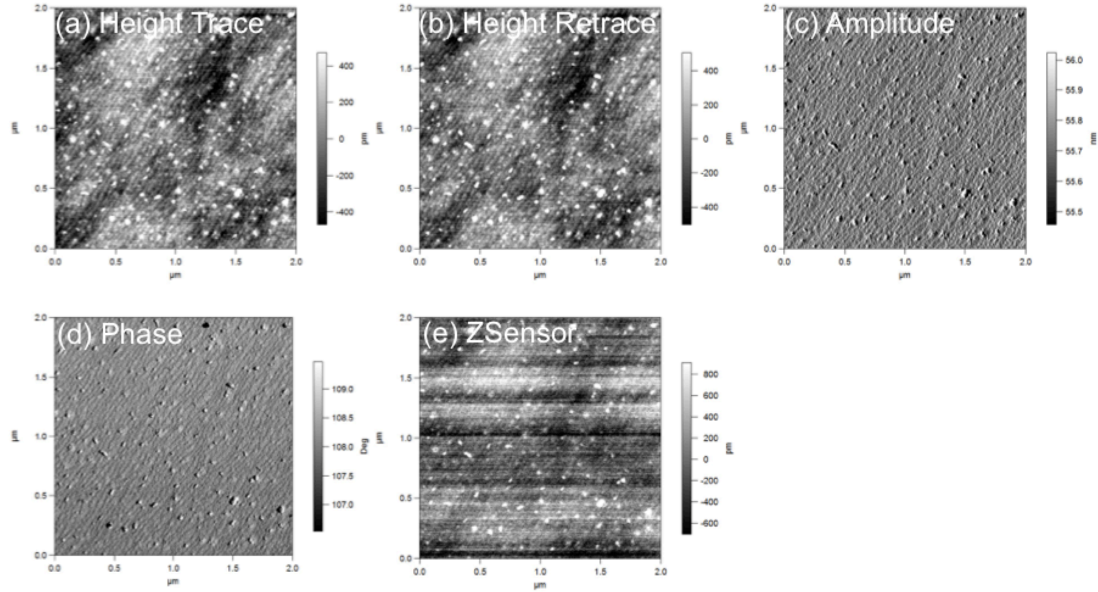

Figure 3.13: AFM scans on ICPD structure R120 over a 2 µm × 2 µm area in (a) height trace, (b) height retrace, (c) amplitude, (d) phase, and (e) ZSensor channels.

In the AFM image (height retraced) of R120 (Figure 3.13 (b)), the root mean square roughness is 0.2 nm, indicating a smooth surface. Spots that are 1–3 nm tall and ∼50 nm wide with a density of 3×10^{8} cm^{-2} were observed on the surface. They may be associated with the 35 nm InAs capping layer rather than actual structural defects in the ICPD structure. Figure 3.14 shows the line profile in the image with 2 µm covering ~50 atomic steps. The average step length is about 40 nm, which results from the off-cut angle of the (001) substrate. Following the equation, sin(off-cut angle) = monolayer thickness / step length, the calculated off-cut angle of the substrate is 0.44°, which is close to 0.47° specified by the substrate vendor (Wafer Technology GaSb R3/GS/1048/Un). A monolayer thickness of GaSb = ~0.305 nm was used in this estimation. The step lines are along the [-110] since the off-cut is towards (111)A.

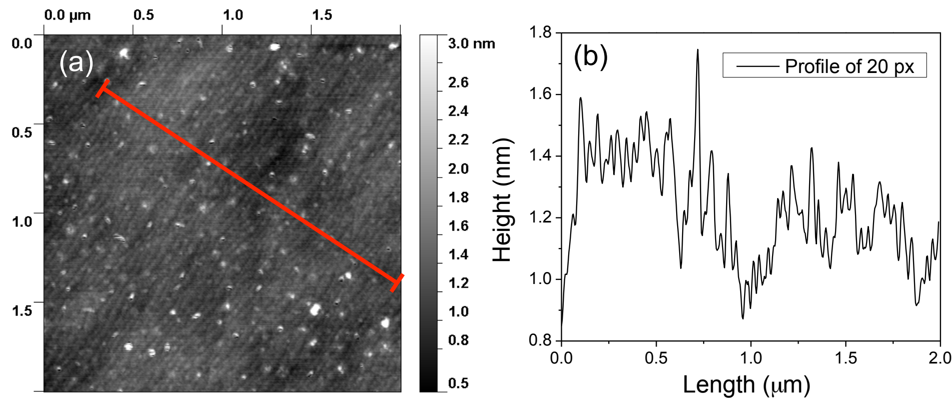

Figure 3.14: (a) AFM scans on ICPD structure R120 over a 2 µm × 2 µm area in height trace. The red line indicates the position of the line profile shown in (b). (b) The profile of 20 pixels crossing ~50 atomic steps.

Figure 3.15 shows an AFM scan over a larger area of 10 µm ×10 µm. The surface is uniform over the 10 µm square in terms of the roughness and the defect density. Two horizontal lines appearing in the image are scars resulting from a scanning error. When the cantilever suddenly encounters a very tall feature (*e.g.* particle on the sample, the white one with a tail to the right), the closed loop cannot return to proper tracking immediately and leaves a scar (or stripe, stroke) parallel to the scanning axis in the image. The long diagonal lines are real features on the sample, which are known as slip lines defects oriented in <110>. Slip line defects typically originate from the thermal stresses associated with temperature gradients in the wafer substrate, and the external forces on the wafer from clips, the diffuser plate, and the weight of wafer [109]. The lines are heavier and deeper around the edges of the wafer than in the center. In optical images with DIC microscopy typically only the slip lines at the edges (larger) can be observed; whereas with AFM center slip lines (smaller) are also observed.

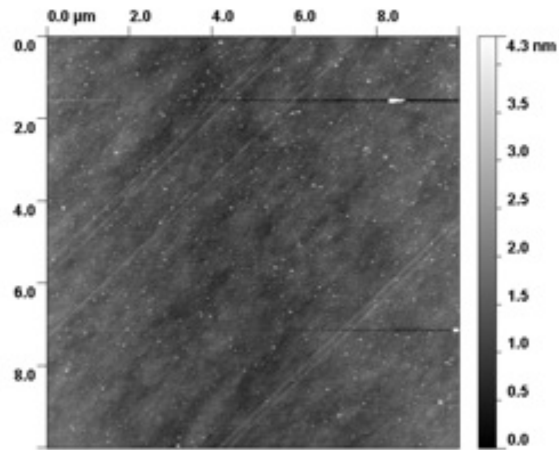

Figure 3.15: AFM scans on ICPD structure R120 over a 10 µm ×10 µm area in height trace.

3.3 Scanning Electron Microscopy

Scanning electron microscopy (SEM) is a microscopy technique based on the interaction of a focused electron beam that is scanned in a raster pattern. Compared to AFM, SEM provides great flexibility in choosing scanning areas, directions and magnifications, as well as a variety of information about surface topography, composition, and other properties such as crystal orientation, and electrical conductivity. SEM was widely used in this project to study the surface morphologies of the epitaxial samples and for failure analysis of devices, especially for troubleshooting the device fabrication procedures.

3.3.1 Principle and Microscope Architecture

The electron beam is produced by the electron gun, focused through electron optics, and reaches the specimen surface with a spot size about 1~10 nm in diameter. The energetic electrons interact with atoms in the specimen and lead to a large interaction volume with micron-sized dimensions. Figure 3.16 shows the droplet shaped interaction volume including labels showing where different types of signals originate. The size and shape of the volume depend on many factors, including accelerating voltage of the electrons and sample composition. Secondary electrons (SEs) are loosely bound outer shell electrons from the specimen atoms which receive sufficient kinetic energy during inelastic scattering of the beam electrons to be ejected from the specimen and set into motion [110]. The SEs have energy less than 50 eV (usually ~5 eV), and these electrons originate within 50 nm of the surface, which forms the shallowest interaction volume in the Figure 3.16. This is why an SEM with

SE imaging can produce very high-resolution images for a specimen surface, revealing details less than 10 nm in size.

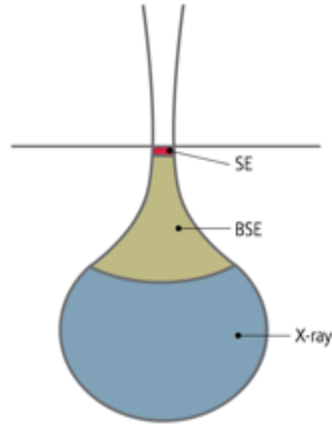

Figure 3.16: Different types of signal originate from different volumes of interaction [111].

Backscattered electrons (BSE) are high-energy electrons that originate from the primary electron beam and are scattered out of the specimen by elastic collisions. Because the intensity of the BSE signal is sensitive to the atomic number of the specimen, BSE images can provide information about the distribution of different elements in the sample. For crystalline samples, the density of atoms that the beam encounters will vary with the crystal orientation, so the BSE signal can also be used to study electron-channeling patterns and identify orientations. However, due to the high energy the interaction volume extends to a few micrometers below the surface. The image resolution is limited particularly for backscattered or x-rays signals which originate from the deeper parts of the interaction volume. A Monte Carlo simulation can help estimate the size of the interaction volume mainly based on the backscattered electrons [112]. For example, because silicon has a density of 2.3 g/cm^3, the depths of the interaction volume are about 0.35 μm and 1.15 μm with a 5 and 10 keV electron

source respectively. For gold with a density about 19.3 g/cm^3, the depth of the interaction volume is about 0.2 μm with a 10 keV electron source.

Characteristic x-rays originate from an even deeper part of the interaction volume. They are emitted when the electron beam removes an inner shell electron from the sample, causing a higher energy electron to fill the shell and release energy. These characteristic x-rays are used to identify the elements in the sample, and hence reveal much about its composition.

A ZEISS NEON 40 EsB high-resolution SEM was used to take all the SEM images in this work. It combines the imaging and analytical capabilities of a high-resolution FE-SEM, using the proven GEMINI lens design, with an advanced Canion FIB column. The microscope uses accelerating voltages from 0.1 to 30 keV, achieves magnification from ×20 to ×900,000, and achieves resolution down to 1.1 nm. The microscope also has do energy dispersive x-ray spectroscopy (EDS) point analysis and mapping and electron backscatter diffraction (EBSD) mapping. It also has a focused ion beam (FIB) milling unit with multi-channel gas injection system for deposition of metal and insulating layers as well as enhanced and selective etching.

Three detectors are used in the imaging: an in-lens secondary electron detector, a backscattered electron detector (BSD), and a secondary electron (SE) detector. The in-lens detector is set above the snorkel lens (the final objective lens), and the SEs can spiral upward in the magnetic field to reach this detector. The highly energetic backscattered electrons are less strongly confined by the magnetic field and reach the retractable annular backscattered electron detector beneath the lens [110]. Thus, the SEs can be separated from the backscattered electrons effectively leading to high

resolution and low noise imaging of backscattered electrons. Another SE detector is available below the lens at an angle to the side of the specimen. It detects primarily SEs but also has a small component of line-of-sight BSEs, which can give some compositional contrast. In addition, since the SE detector collects the signal at an angle away from the top-down line of sight, the image from the SE detector gives a bit more topographical information compared to the flatter image produced by the in-lens detector [89].

3.3.2 SEM of Surface Morphology

Figure 3.17 shows SEM images of the same series of defects in an InAs homoepitaxial layer taken with different detectors and accelerating voltages. Figure 3.17 (a) and (b) were taken with an in-lens detector with 5 keV and 10 keV accelerating voltages, respectively. Due to the lower accelerating voltage for (a), the interaction volume is smaller and this leads to a higher resolution and more topographic details in the center of the defect compared to image (b). Figure 3.17 (c) was taken by a BSD, which could not define the morphology inside the defect pit due to the much larger interaction volume of the signal (shown in Figure 3.16). However, the hillock structures and atomic steps are more obvious in a BSD image than in an in-lens detector image, *e.g.* the insets to (c) and (a) of the same defects. For a crystalline specimen, the backscattered electrons are sensitive to not only the atomic number, but also the crystalline properties (atom arrangement). Paths of high incident electron penetration are along certain directions (channels), which permit a larger fraction of the beam to penetrate deeper into the crystal before scattering. These directions can be tilted due to strain at dislocations and step edges, which results in a difference in BSE

yield, and thus contrast in the BSD signal. Thus, the BSD image can provide strain sensitive information in crystalline samples.

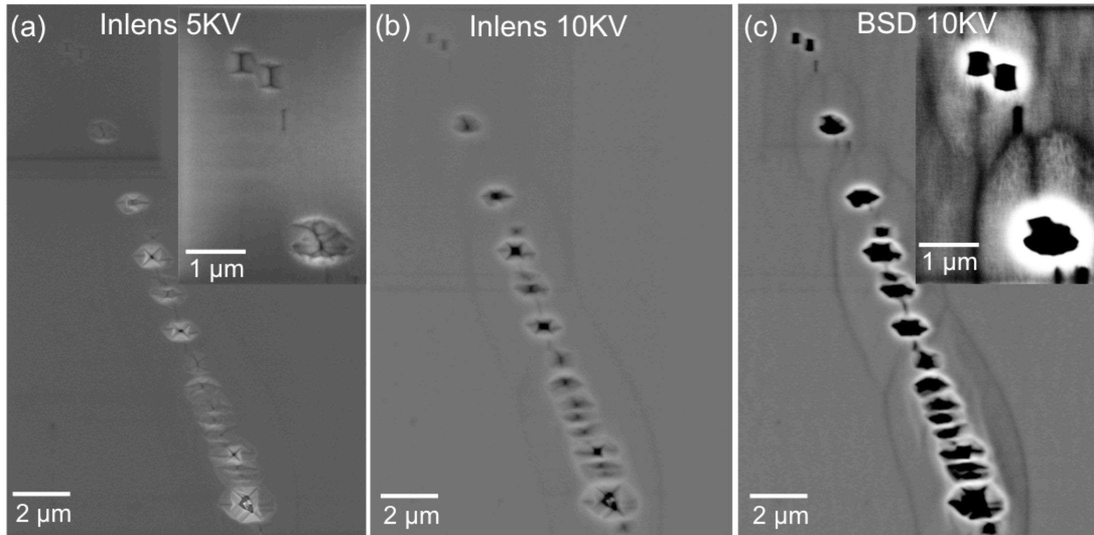

Figure 3.17: Detailed morphology of the same defects in an InAs homoepitaxial layer in images using: (a) the in-lens detector with 5 keV accelerating voltage, (b) the in-lens detector with 10 keV accelerating voltage, (c) the BSD detector with 10 keV accelerating voltage. Insets to (a) and (c) are the same top-left defects in a higher magnification.

Figure 3.18 shows more defects taken by a BSD with a 10 keV accelerating voltage in an IC laser structure R099. A DIC microscopy map was stitched with ~90 images (not shown) to help locate each defect and compare the morphology in DIC microscopy and SEM images. The defects that are outlined in the DIC microscopy image (a) are typical ones in a device structure and were imaged by SEM in (b-e). Since DIC microscopy is ultra-sensitive to height differences, both large and small shallow defects are seen with good contrast. Therefore, we mainly rely on DIC microscopy for regular surface morphology characterizations. More information on defect characterization can be found in Chapter 4.

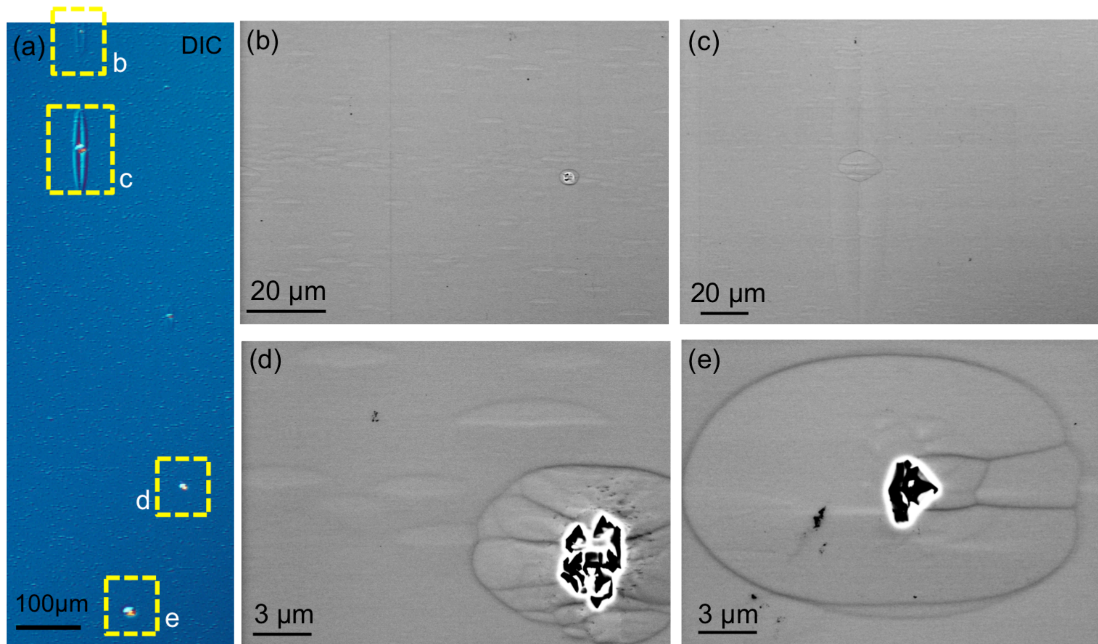

Figure 3.18: (a) DIC microscopy image of IC laser structure R099. (b-e) BSD SEM images of defects appearing in image (a) (labeled squares) taken at 10 keV.

A further example of SEM of surface morphology can be found in Figure 3.19 (a-c), where the atomic steps are visible in homoepitaxial InAs layers using the BSD and agree well with the details in AFM images (d-f). Figure 3.19 (a-c) were taken by the BSD with a 10 keV accelerating voltage at a working distance of 4.2 mm, while (d-f) were taken by AFM on the same samples. Both SEM and AFM images are scanned over a 2 μm ×2 μm area, and the ~55 nm long atomic steps are easily seen. It is clear that T485 (b) has a more wave-like surface compared to T488 (a) and T454 (c), as seen in the AFM images as well. Because of the electron channeling effect, ~55 nm wide atomic steps with a few nanometers height difference can also be seen in the SEM image. However, it can be more challenging to image atomic steps on a smooth surface. A good focus of the beam is required with a scan speed of 9 or slower to reduce the noise in the image. Other critical image settings are: a contrast of >90 %, a brightness of <3%, and a high BSD gain. Tilting of sample stage is sometimes useful

to promote the channeling effect by finding an angle at which the backscattering yield varies sharply with the tilt of the atomic planes. In this work it is important to be aware of the changes in focus due to the sample tilt related changes in working distances as the sample is moved.

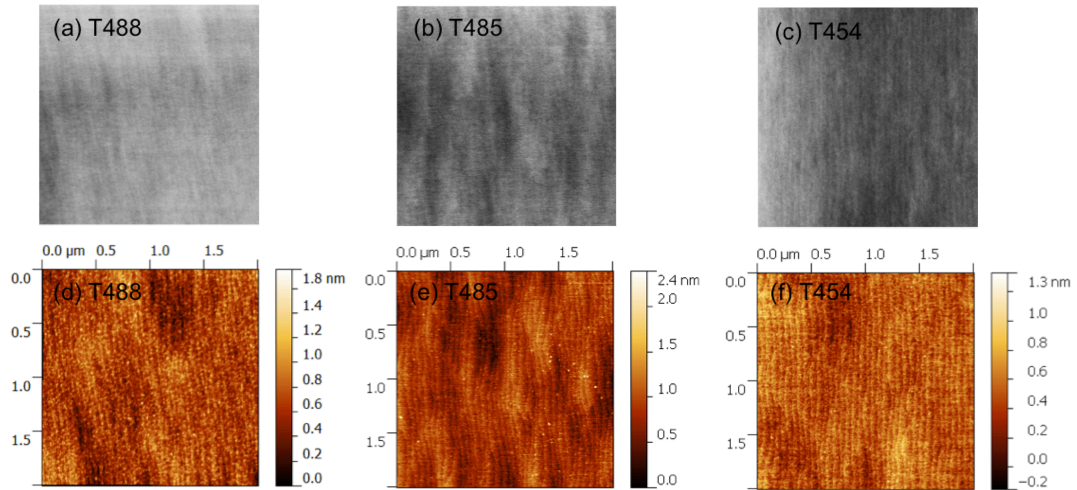

Figure 3.19: (a-c) SEM images of InAs homoepitaxial layers over a 2 µm ×2 µm area taken by the BSD with a 10 keV accelerating voltage at a working distance of 4.2 mm; (d-f) AFM images of the same samples.

3.3.3 SEM of Devices after Fabrication

SEM plays a crucial role in investigating fabrication quality and conducting device failure analysis, because of its great flexibility in image scales and directions, as well as the ability to analyze material compositions. Several failure analysis examples will be discussed in this section.

SEM was used to investigate how mirror facet qualities affect the device performances of broad-area (BA) IC lasers (150 mm wide laser ridge). In semiconductor lasers, the natural cleavage planes form laser end mirrors, because of their sharp refractive index difference between the crystal and the surrounding air. The

threshold current of the laser I_{th} can be simply expressed by the following equation, and it increases with mirror loss and internal loss.

$$I_{th} = I_{tr} + \frac{1}{a}(\alpha_m + \alpha_i) \qquad (3.18)$$

I_{tr} is the transparency current where population inversion occurs, "a" is the differential gain, α_m is the mirror loss, and α_i is the internal loss. The mirror loss α_m can be written as

$$\alpha_m = \frac{1}{2L} ln\left(\frac{1}{R_1R_2}\right) \qquad (3.19)$$

where L is the cavity length, and R_1 and R_2 are the reflection coefficients of the front and back side mirrors. Based on these equations, poor mirror facets with low reflection can reduce the threshold current of the laser.

More than 16 lasers on 2 bars of R096 were characterized electrically by measuring the resistance, threshold voltage, threshold current density, and operation wavelength at 80 K. Lasers with a low threshold current density were also tested at their highest operation temperature. For saser bar R096BA-1, which a cavity length of 1.2 mm, 6 of the 8 devices lased at 3.96±0.03μm with the lowest threshold current density 10.8 A/cm^2. All the working lasers had a threshold current density lower than 18 A/cm^2. However, 4 of the 6 working lasers had an unstable intensity, especially at high temperatures. The highest operation temperature was 190 K and 320 K in CW and pulsed mode, respectively. For laser bar R096BA-2, which has a cavity length of 0.88 mm, 7 of the 8 devices lased at 3.96±0.02 μm with the lowest threshold current density of 21.6 A/cm^2. The highest operation temperature was 210 K and 305 K in cw mode and pulsed mode, respectively. However, the lasers' non-uniformity issue is

severe, as 4 lasers have threshold current densities greater than 80 A/cm^2, and two of them were not stable.

To investigate the non-uniformity issue, SEM was used to check the front and back side facets. Because the laser bars are cleaved by hand after sample lapping down to a thickness of ~150 µm, the facet quality could not be well controlled and cracks would appear on the facet. Note that no antireflection coating was used in our fabrication. Figure 3.20 shows the schematics of the broad-area laser structure corresponding to the front side facet. Figure 3.21 shows four representative lasers on R096BA-1 and R096BA-2 with their front and back side facet details. Since the laser bar was mounted on a chip carrier and a heat sink, back side facet images were taken at a long working distance of 15 mm and a tilt angle of 50° to 60°. Therefore the resolution is lower than the front side facet images, which were taken in cross-sectional view at 90° and at a ~3 mm working distance. The two laser bars were cleaved from the same wafer after broad-area processing. The laser ridge is about 150 µm wide, the cascade stages are about 480 nm thick with 10 stages, the SiO_2 is 220 nm thick, and the Ti/Au contact layer is about 30/300 nm thick.

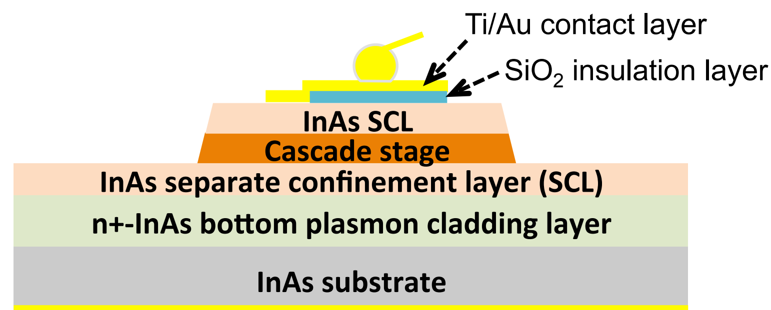

Figure 3.20: Schematics of a broad-area laser with the SiO_2 insulation layer and Ti/Au contact layer.

By comparing the facet morphology and the device performance, we found that the cracks on the facet were common and had a very limited effect on the device performance. The R096BA-2 had a bad cleave on the back side facets. All the devices on the bar have cracks on the facet in a similar degree, as shown in Figures 3.21 (a) and (b). It seems that the three low-threshold-current-density lasers have smooth front facets (*e.g.* R096BA-2-F in Figure 3.21 (b)). However, high-threshold-current-density devices R096BA-2-G and H also have a smooth front side facet. For laser bar R096BA-1, some contamination spots were found on the facet which could be due to the handling of the laser bar during experiments but did not affect the device performance. Five lasers (B, C, D, E, F) have similar facet morphology. The back side facet has deep cracks while the front side one is smooth (*e.g.* R096BA-1-C in Figure 3.21 (c)). However, devices B and F lased, C and E lased but not stable, and D would not lase at all. Even though device H has the smoothest facets among all the devices we checked (Figure 3.21 (d)), it does not have the lowest threshold current density and the lasing intensity is not stable. To summarize, we did not find a link between the facet morphology and device performance.

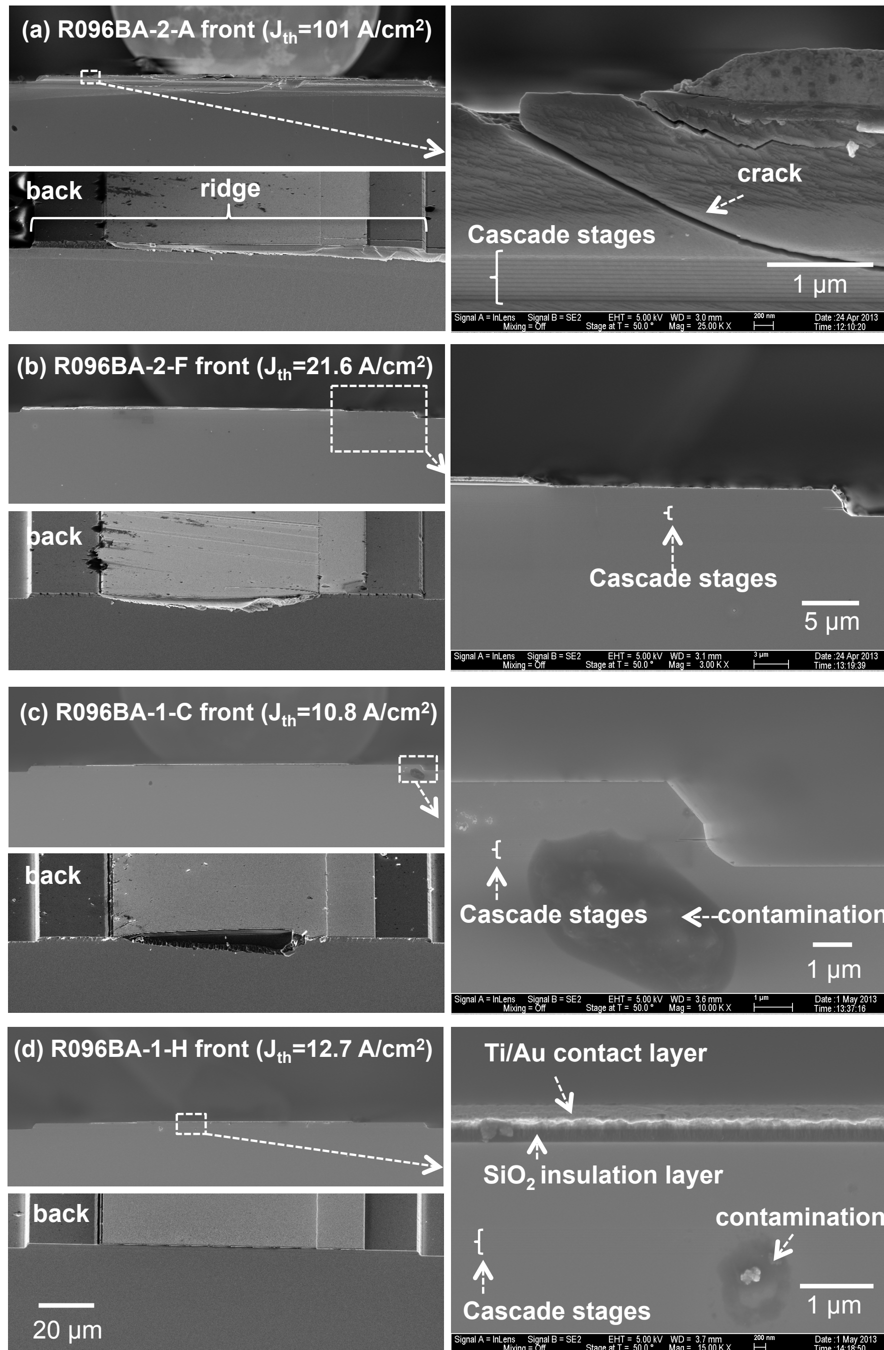

Figure 3.21: SEM images of the laser facets on different lasers. Full size view images of front and back side facets were taken under the same magnification. The front side facet images which were taken in cross-sectional view at 90° and at a ~3 mm working distance. The back side facet images were taken at a long working distance of 15 mm and a tilted angle of 50° to 60°.

The best device in R096BA1 has a lower threshold current density than the best one in R096BA2, which may result from the shorter cavity length of R096BA2

instead of the facet morphology. In addition, DIC microscopy images were taken for these lasers after testing to count the number of large defects on the laser mesas. Oval and elliptic defects larger than 10 μm were counted (similar to the ones in Figure 3.18 (a)), and there are 0~5 large defects on each mesa. However, no correspondence between the defect number and threshold current density was found. The mechanism that leads to the non-uniformity is still unknown. Other factors in material growth and/or device fabrication limit the device performance and overpower the effects that facets or large defects contributed.

Another example of using SEM and EDS is given on the same IC laser R096BA-2 to investigate the bonding-delamination problem. After the wafer was processed into lasers, laser bars are mounted onto the heat sink and electrically connected to the chip carrier using gold wire bonding. However, ~30% of the bonds failed on IC laser R096BA-2 and other devices processed together. The bonding process makes craters on the laser ridge as the bonding ball is pulled off, and the contact layer seems to easily delaminate from the semiconductor surface (shown in Figure 3.22 (a)). From the SEM top-view images of the delamination (Figure 3.22 (b)), the semiconductor and SiO_2 or Ti/Au interfaces should be the breaking link. However, the clear boundary lines between the part underneath the delamination and the mesa surface (indicated by the arrows in Figure 3.22 (b)) suggest other possibilities, *e.g.* a delaminated semiconductor layer (there is a 35 nm highly doped InAs layer on top).

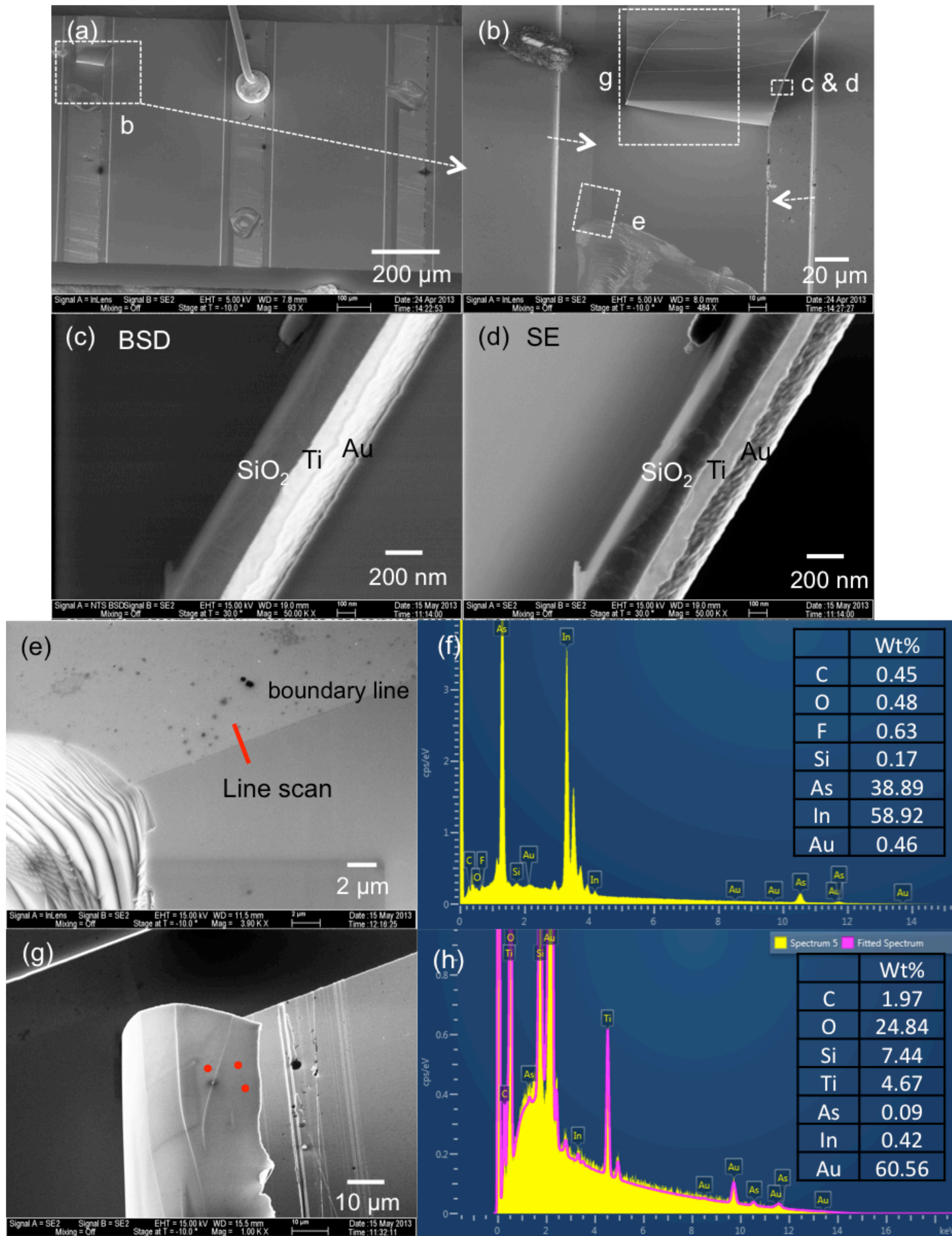

Figure 3.22: SEM and EDS analyses on IC laser R096BA-2 of the bonding-delamination problem. (a, b) SEM images of devices with failed bonding craters and delaminated contact layers. Dashed squares indicate the positions at which the images were taken. (c, d) SEM images of delaminated contact layers using the BSD and SE detectors. (e) The EDS line scans on the laser ridge. (f) The line scan sum spectrum and the weight percent of the elements in the line scan. (g) The EDS spots on the backside of the delaminated contact layers. (h) Representative point scan spectra and the weight percent of the elements.

SEM using the BSD and SE detectors was used to check the peeled off layers in Figure 3.22 (c) and (d), respectively, at a view parallel to the laser ridge. Although the SiO_2, Ti, and Au layers can be seen, it is hard to distinguish the fourth layer of InAs next to the SiO_2 layer due to the edge effect. EDS was used to check the compositions across the boundary lines, and there is no noticeable difference in the elemental compositions. The line scan sum spectrum is shown in Figure 3.22 (f) with the weight percent of the elements. A small amount of carbon, oxygen, and fluorine were detected due to the contaminations, semiconductor oxides, and HF residue during fabrication. Silicon was detected because it is the dopant in the InAs layers in the laser structure. Moreover, a small amount of gold was detected, which might come from the scattered electrons interacting with nearby gold layers. Three spots at the backside of the peeled layer were scanned, and the EDS spectra were collected (Figure 3.22 (h)).

Oxygen, silicon, titanium, and gold were detected from the SiO_2 and Ti/Au layers. The amounts of indium and arsenic that were detected was so small (less than 10% titanium weight) that it could not be a layer thicker than 10 nanometers. The signal may come from the In and As bonds (>3 nm) to the SiO_2 layer, or the scattered electrons interacting with the background. Therefore, the boundary line was most likely coming from the process, as the surface not covered by Ti/Au most likely has residue from the bonding wax used to hold wafers during backside thinning. This is also why the layer seems smoother under the SiO_2 and Ti/Au. The result suggests that the weakest link that breaks in the bonding is the semiconductor and SiO_2 or Ti/Au interfaces, which may be an issue of surface oxides on the laser mesa before the deposition of SiO_2 or Ti/Au layers.

Chapter 4 MBE Growth of InAs-Based Interband Cascade Laser Structures

4.1 InAs (001) Homoepitaxy

In this chapter we will discuss the MBE growth of InAs-based ICL structures grown on InAs substrate, and we start with the growth of InAs layer. The InAs homoepitaxial layer serves as the initial surface for the cascade region and strongly affects the realization of the designed band structure of the interband cascade laser. It is essential to have high quality layers with low defect densities and atomically smooth surfaces to facilitate high performance devices. In addition, InAs has attracted interest in different device applications due to its advantages of high electron mobility, narrow band gap, feasibility of having high carrier concentration, and the opportunity for quantum engineering in the 6.1 Å lattice-matched system. InAs layers with different doping concentrations on InAs(001) substrates have been made into devices such as photodetectors [113, 114], thermophotovoltaic cells [115], resonant tunneling diodes [4, 116] and avalanche photodiodes [117]. Highly *n*-type doped (and lightly doped or undoped) homoepitaxial InAs layers were used as plasmon-cladding (and waveguide-spacer) layers in the applications of mid-infrared (IR) quantum cascade (QC) and interband cascade (IC) lasers to replace the conventional semiconductor waveguide structures and help extend the emission wavelength [118-122]. Recently, highly doped InAs was demonstrated to be a candidate for mid-IR plasmonic and metamaterial structures, since the plasma frequency can be controlled over a broad range of mid-IR frequencies [123]. Therefore, the study of InAs homoepitaxy layers benefits the growth of interband cascade lasers as well as wider InAs applications.

In the previous research on InAs homoepitaxy by MBE, most of the theoretical [124] and experimental [125-128] work focused on the surface reconstructions and their transitions. A few experimental studies investigated different growth conditions and provided useful information on kinetic evolution and defect formation [85, 129, 130]. However, there is still limited information about the relation between InAs growth conditions and the resulting InAs crystal quality, as well as the defect morphology and origins [131, 132]. This section documents n-type doping of InAs layer with Si and GaTe, in a systematic study of the optimum InAs growth conditions at a high growth rate. Defect density, defect morphology, and surface roughness were carefully investigated to evaluate material quality *ex situ* by using DIC microscopy, SEM, and AFM. A further study was carried out on pitted oval hillock defects to help elucidate their origin. The underlying goal is to further understand the growth mechanism and provide high quality InAs homoepitaxial layers for different applications.

4.1.1 n-type Doping of InAs Layer with Si and GaTe

Room temperature Hall-effect measurements were carried out on InAs layers grown on semi-insulating GaAs substrates to calibrate doping concentration. InAs layers suffer from an electron accumulation layer due to surface Fermi level position above the conduction band minimum determined by the surface geometry [133]. Because of the parallel conductance from the two-dimensional electron gas at the surface, one needs to be cautious when interpreting Hall data for low doping concentration InAs layer. Considering the bulk and the surface layers as two resistors in parallel, the bulk resistance needs to be much smaller than the surface resistance to

allow the use of a one-carrier model in the calculations. By measuring two undoped InAs layers (1.25 μm and 2.5 μm thick) grown on GaAs substrates, the surface carrier concentration was determined to be 1.5×10^{12} cm^{-2}, which is similar to the value reported in literature [134]. Growing thicker bulk layers can partially reduce the problem and make the measurement more reliable. For example, if the measured bulk layer has a three-dimensional carrier concentration of 5×10^{16} cm^{-3}, a 0.5 μm thick bulk layer leads to a two-dimensional concentration of 2.5×10^{12} cm^{-2}, while a 2 μm thick layer leads to 1×10^{13} cm^{-2}. The one-carrier Hall model can be used in the latter rather than the former, since the former has a much smaller difference with the surface carrier concentration.

Silicon is an n-type dopant in arsenides and is capable of a wide range of doping concentrations. Figure 4.1 shows the Arrhenius plot of silicon doping calibrations on InAs layers using a 5cc Si cell in the GEN II (red squares) at a growth rate of 0.22 ML/s and a 1.5 cc Si cell in the GENxplor (triangles) at a growth rate 0.66ML/s. The electrical concentrations are measured by the Hall measurement, and we assume that the doping concentration equals the electrical concentration in the InAs layers. The silicon temperature is the thermocouple reading in the cell. For comparison, a 0.22 ML/s deduced data is plotted in open triangles by increasing doping concentration 3 times for the 1.5 cc cell, assuming the doping concentration is proportional to the inverse of the growth rate. Due primarily to the difference in surface area, the doping concentration is much lower (about 43 times) for the 1.5 cc cell compared to the 5 cc cell at the same cell temperature.

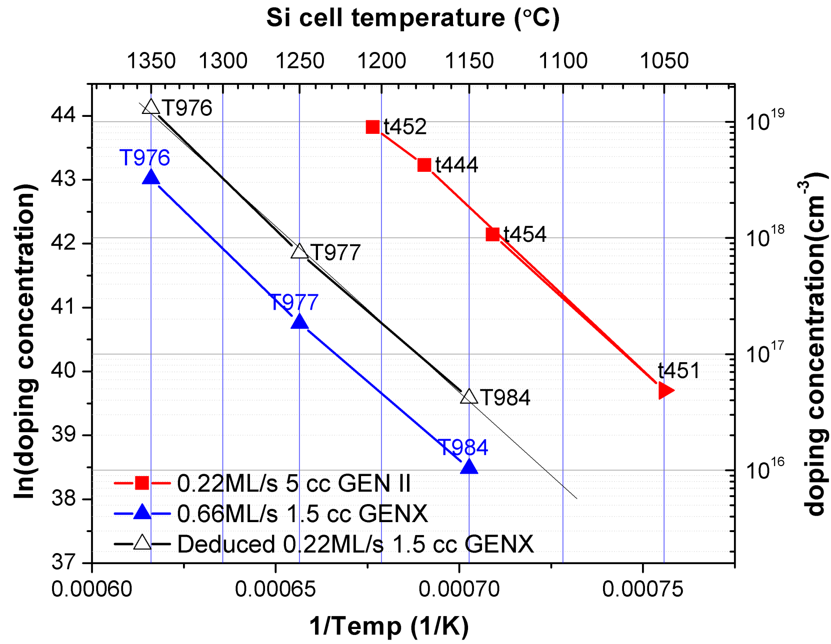

Figure 4.1: Electrical concentration at 300 K versus Si cell temperature for of InAs layer grown on GaAs substrate.

Tellurium (Te) is a group-VI element and acts as a donor in III-V semiconductors by substituting group-V atoms. Te as a source has a very high vapor pressure and hence is not suitable for MBE. GaTe was as an alternative used to dope InAs layer to n type, and the result is shown in Figure 4.2 with carrier concentrations from 10^{17} to 10^{19} cm^{-3}. We used stoichiometric Ga_1Te_1 from UMC (6N) in a 1.5cc crucible in a dual doping cell in the GENxplor. It was observed that GaTe outgassing can affect the doping results, which is also reported in the literature [91]. In our case, outgassing the GaTe cell at 550°C is not efficient to remove elemental Te and Ga_2Te_3, which have higher vapor pressure and may contribute to a higher electrical concentrations (shown in the black dots in Figure 4.2). After outgassing at 630°C for more than 1 hour before growth, the doping concentrations are lower and repeatable (red squares in Figure 4.2).

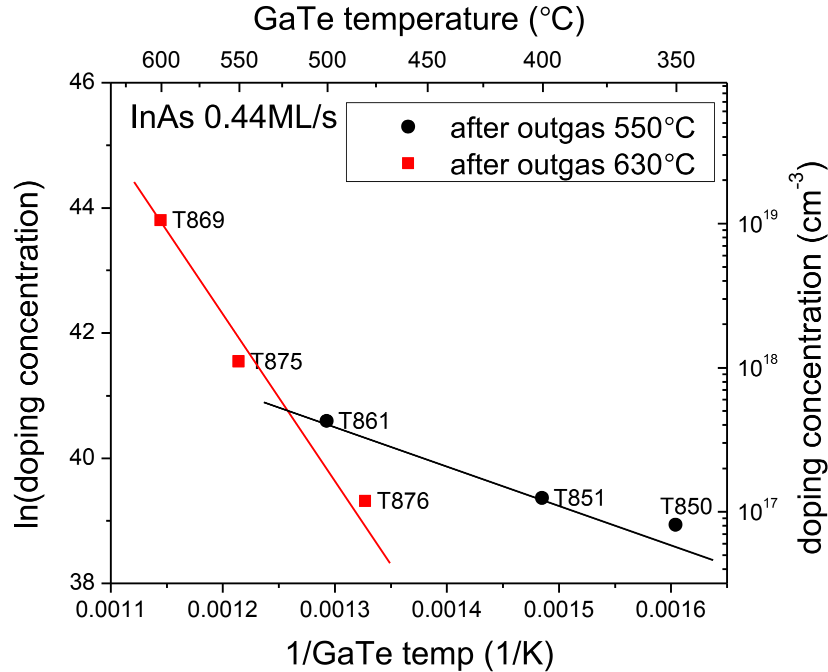

Figure 4.2: Electrical concentration versus GaTe cell temperature based on Hall measurement of 0.5 µm InAs layers grown on GaAs substrates at 0.44 ML/s. Black circles represent layers grown after a 550°C outgassing, while red squares represent layers grown after a 630°C outgassing.

Homoepitaxial InAs growth with high GaTe doping was carried out and resulted in an inferior surface morphology at doping of ~1×10^{19} cm^{-3}, compared to undoped or silicon doped layers. A series of wafers were grown on InAs substrate under different conditions, and the results are partially shown in Figure 4.3 and Table 4.1. Since the InAs substrate is conductive, a Hall effect measurement would be difficult to interpret. Instead, spectral reflectance measurements, as described in an earlier publication [135], were carried out at room temperature to estimate the doping concentrations in the range of 10^{18} to 10^{19} cm^{-3}. The reflectance measurements were designed to probe the Berreman effect, which causes strong absorption of p-polarized light at frequencies where the dielectric function approaches zero [135]. The frequency where strongest absorption occurs is near the plasma frequency. Table 4.1

lists the fitting parameters, the plasma frequency and the electron relaxation time τ, for the reflectance spectra. The high frequency limit of the dielectric constant is taken to be 12.25 for InAs. The effective mass is dependent on the carrier concentration and is estimated using calculations based on the eight band Kane model [135]. When fitting the spectrum to a modeled curve [135], the position and the shape (width in frequency and depth in reflectance) of the minimum provide a measure of the plasma frequency (and therefore the electron concentration) and electron relaxation time (inverse of damping constant).

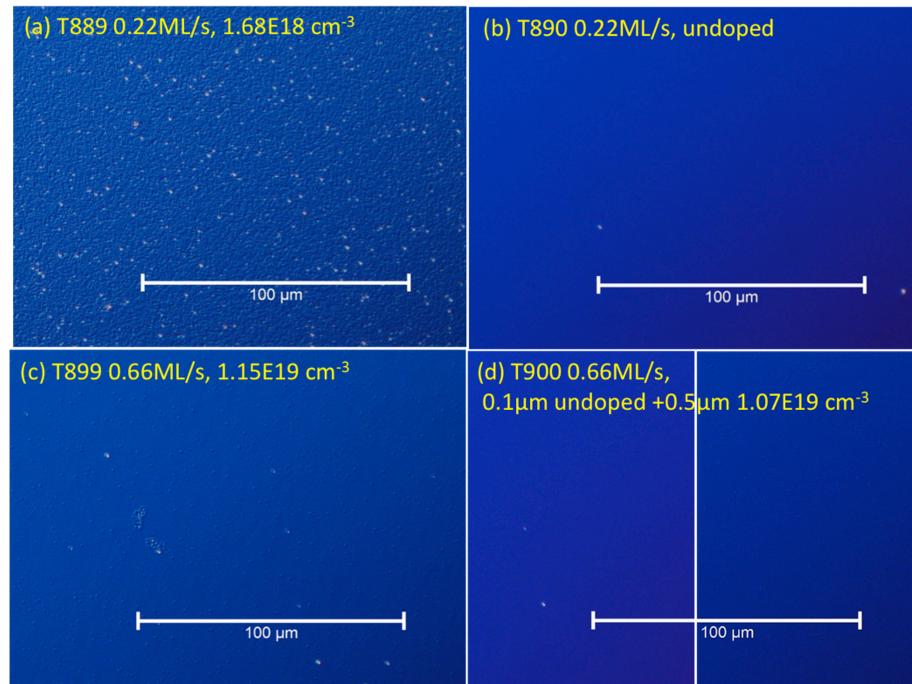

Figure 4.3: DIC microscopy images of InAs epitaxial layers on InAs (001) substrates, (a) T889, (b) T890, (c) T899, (d) T900 with higher and lower defect area.

Table 4.1: Growth conditions and fitting parameters of spectral reflectance measurement in InAs epitaxial layers.

	Structure	Growth Rate (ML/s)	Substrate Temp (°C)	GaTe cell (°C)	Target density (cm^{-3})	Plasma freq (cm^{-1})	Tau (ps)	Measured density (cm^{-3})	Surface morphology (cm^{-2})
T869	0.5µm InAs on GaAs	0.44	~420	600	1.04E19	1085	0.13	1.09E19	Rough
T889	0.5µm InAs on InAs	0.22	~420	591	1.4E19	550	0.3	1.68E18	Rough
T890	0.5µm InAs on InAs	0.22	~420	No doping					<1E4
T899	0.5µm InAs on InAs	0.66	~400	623	1.4E19	1130	0.11	1.15E19	>2E16
T900	0.1µm undoped + 0.5µm InAs on InAs	0.66	~400	−/ 623	-/ 1.4E19	1100	0.12	1.07E19	1E4~1E6

T889 (Figure 4.3 (a)) and T890 (Figure 4.3 (b)) are InAs homoepitaxial layers grown under the same conditions with and without GaTe doping, respectively. T889 has a much rougher surface than T890 as well as a lower than expected electron concentration based on the calibrations in Figure 4.2 (1.4×10^{19} cm^{-3} versus 1.68×10^{18} cm^{-3}). The observations are in contrast to InAs homoepitaxial layers with silicon doping or no doping, where the surface morphology is smooth [92]. This contradicts earlier observations that Te improves InGaAs and GaAs material quality and surface morphology as a surfactant both in MBE and MOCVD systems [136-138]. However, it has also been proposed in chemical beam epitaxy that the Te surfactant effect increases the Ehrlich-Schwoebel barrier and thus causes a three-dimensional growth, which greatly affects the resulting surface morphology [139]. The incorporation of Te decreases with increasing growth temperature and decreasing growth rate [139]. Moreover, the surfactant effect of Te is thermally activated. Thus, kinetically limiting growth parameters (low growth temperature, high growth rate) favor a two-dimensional growth [139]. To test the hypothesis, T899 was grown with a decreased growth temperature from ~420 to 400˚C, and an increased growth rate from 0.22 ML/s

to 0.66 ML/s. In agreement with the hypothesis [139], the surface morphology is greatly improved (Figure 4.3 (c)). However, it is still worse than the undoped layer and has a high defect density of $>2\times10^{6}$ cm^{-2}. Note that the electron concentration has also been increased to the 1×10^{19} cm^{-3} range.

During the growth in T899, it was found that the RHEED pattern was spotty and diffuse during the first 50 to 100 nm. Therefore, T900 was grown with an additional 100 nm undoped InAs buffer layer to smooth out the rough surface after oxide desorption. Both higher and lower defect areas were observed on the wafer surface (Figure 4.3 (d)). Therefore, the extra buffer layer was not able to solve the problem completely.

XRD measurements were applied to check if there was any lattice dilation due to the larger size of Te atoms compared to As atoms [138, 139], or a lattice mismatch due to the incorporation of Ga atoms in the InAs layer. The FWHMs of the InAs peaks were about 15 arcsec, and no noticeable epilayer peak was found. This suggests that the rough morphology was not due to the influence of a changing InAs lattice as proposed in the reference [140]. Further studies are needed to address the problem of rough surface morphology at high Te doping. Therefore, silicon was preferred for InAs n-type doping in the IC laser structures.

4.1.2 Surface Roughness of Homoepitaxial InAs

We investigated InAs homoepitaxy at a growth rate of 0.66 ML/s that is high enough to enable sophisticated device structures to be grown in a reasonably short time. The InAs homoepitaxial structure was grown on an epi-ready S-doped (n~2.5×10^{18} cm^{-3}) InAs substrate using a GEN II MBE system. Guided by the growth

conditions reported in the literature [126, 130, 141], the substrate temperature and As_2/In beam flux ratio were selected to cover wide ranges of 400 – 500˚C and 7:1 – 30:1, respectively. The growth conditions and defect densities have been investigated and discussed in a previous work mainly by DIC microscopy [142]. The wafers were renamed for easier reading, (T1=T456, T2=T485, T3=T483, T4=T499, T5=T478, T6=T488, T7=T484, T8=T473, T9=T463, T10=T459, T11=T454). A low defect density in the InAs layer is important because defects that propagate into the laser structure can serve as recombination centers that degrade device performance. In addition to the defect density, the surface morphology, characterized as roughness, of the InAs layer is an important criterion of material quality, especially for applications where device structures are subsequently grown on the InAs layer. For example, a laser structure may be successively grown on an InAs lower waveguide layer. A smooth surface of the highly-doped InAs layer not only suggests good crystalline quality of the waveguide layer, but also facilitates sharp interfaces in the subsequent laser structure, which is composed of more than ~100 ultrathin layers in interband cascade or quantum cascade devices [5, 143]. An example is given in Section 3.1.2 for IC laser structures, where a rough surface of the InAs buffer layer affects the sharpness of the SL interfaces and thus can cause difficulties in obtaining the designed band offset. In order to evaluate the surface roughness, SEM and AFM were used to study the homoepitaxial layers under different growth conditions.

In Figure 4.4, we graphically represent the relation between the surface defect densities and growth conditions for the InAs homoepitaxial layers. Instead of using the thermocouple for reading temperature [142], Figure 4.4 uses pyrometer measurements

for substrate temperature. A larger circle indicates that the corresponding InAs layer has a smaller defect density. As can be seen in Figure 4.4, the defect density depends on the As_2 overpressure significantly and is relatively insensitive to the substrate temperature in the range from 400˚C to 470˚C. For homoepitaxial InAs layers, a growth region with a low defect density was found when a moderate As_2 overpressure was applied (As_2/In beam flux ratio of 11:1 to 21:1) and with a substrate temperature of 400 to 450˚C. A significantly lower defect density of 2×10^4 cm^{-2} was obtained under these conditions with the majority of defects being oval hillock defects with pits.

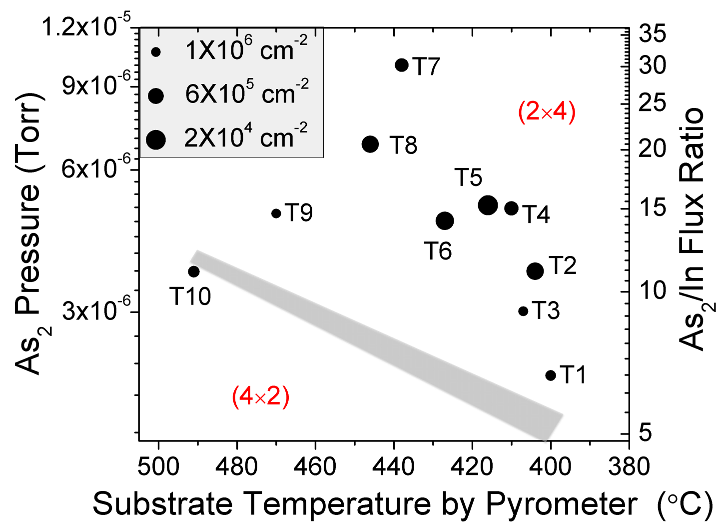

Figure 4.4: The relation between the surface defect density and growth conditions for InAs homoepitaxial layers. A larger circle size shows that the corresponding InAs layer has a smaller defect density. The gray area indicates a transition region that separates regions where 2×4 or 4×2 reconstructions were observed during growth. The transition region was experimentally determined by decreasing the As flux for a brief time during some of the layer growths. Based on the RHEED patterns, all the structures were grown in the As-stabilized (2×4) region except T10 [92].

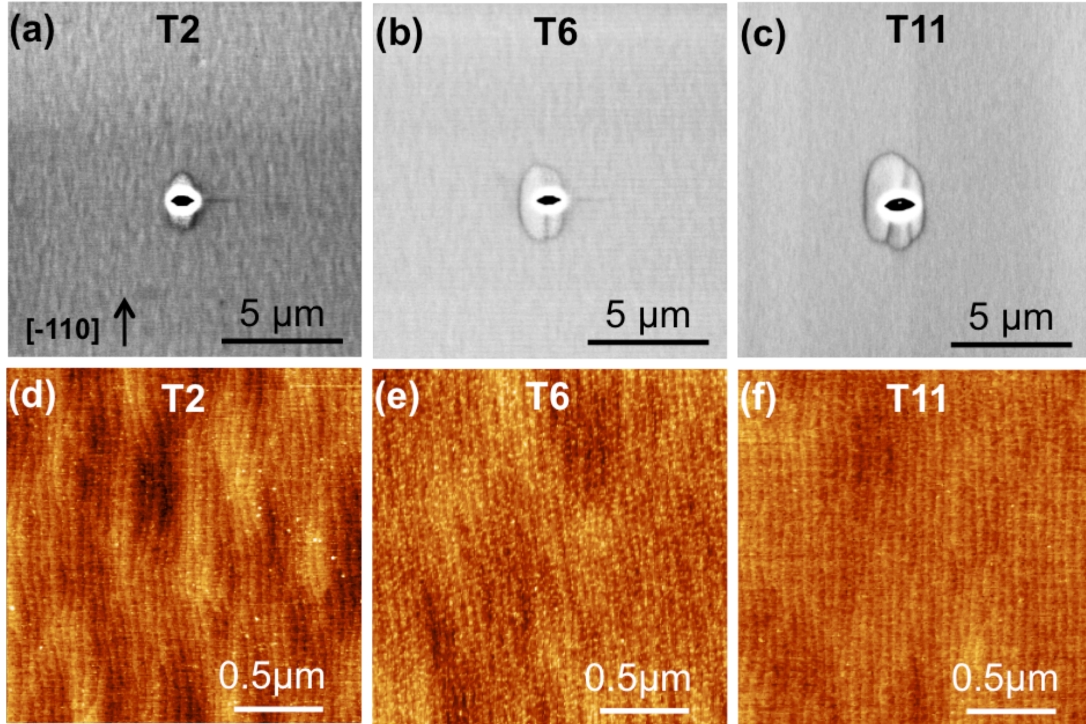

Figure 4.5: SEM images (a, b, c) captured by an annular backscattered electron detector and 2 μm × 2 μm AFM area scans (d, e, f) of the homoepitaxial structures grown at different conditions. The color scale is 2 nm in the AFM images. The substrate temperature (T), As_2/In flux ratio (V/III), RMS surface roughness (RMS) and peak to valley height (P-V) are as follows: (a, d) Structure T2, T= 405˚C, V/III=11:1, RMS = 0.22 nm, and P-V = ~1.3 nm; (b, e) Structure T6, T= 427˚C, V/III=14:1, RMS = 0.19 nm, and P-V = ~0.8 nm; (c, f) Structure T11 grown at 0.22 ML/s, T= 400˚C, V/III=8:1, RMS = 0.13 nm, and P-V = ~0.8 nm [92].

Figure 4.5 shows SEM images (a)-(c) captured by an annular backscattered electron detector (BSD) and 2 μm × 2 μm AFM area scans (d)-(f) of the homoepitaxial layer surfaces. According to the SEM images of the structures grown with moderate As_2 overpressure, the structure grown at a low substrate temperature below 420˚C had a relatively undulating surface, while the structures grown at a higher substrate temperature had a smoother surface. Figures 4.5 (a) and (b) show the SEM images of structures T2 and T6, respectively as examples of low and high substrate temperature structures. For structure T2, grown at 405˚C, the RMS roughness and the peak to

valley height are 0.22 nm and ~1.3 nm, respectively. The corresponding values for structure T6, grown at 430˚C, are 0.19 nm and ~0.8 nm. These results suggest that a higher substrate temperature between 430˚C and 460˚C led to a smoother surface, which might result from the increased kinetic energy for indium migration on the surface.

According to the growth condition map shown in Figure 4.4, optimum growth conditions for homoepitaxial InAs(001) growth at 0.66 ML/s can be found at a substrate temperature of between 430˚C to 450˚C and an As_2/In flux ratio of about 15:1. Under these conditions, material with both a low defect density and a smooth surface was obtained. It is worth noting that the optimum growth conditions can be different for InAs layers in SL structures, where good conditions for a second material will need to be considered.

A slow growth rate of 0.22 ML/s was used for structure T11, which was grown at a substrate temperature of 400˚C and an As_2/In beam flux ratio of 8:1 on a quarter of a 2-inch wafer. The density of pitted oval hillock defects was 4×10^3 cm^{-2}, which is lower than the lowest defect density found at 0.66 ML/s. The SEM and AFM images are shown in Figures 4.5 (c) and (f), respectively. The RMS surface roughness and the peak to valley height are 0.13 nm and ~0.8 nm, respectively. According to our analysis, the quality of the homoepitaxial InAs layer grown at 0.22 ML/s is slightly better than that of layers grown at 0.66 ML/s under optimum growth conditions. Additionally, compared with structures T1, T2, and T3, which were also grown at around 400˚C with different As_2 overpressures, the defect density is higher and the surface is more undulating for the higher growth rate. This suggests that InAs homoepitaxial growth is

sensitive to the growth rate, and a low growth rate of 0.22 ML/s is preferred to achieve a high material quality since it provides a longer time for atoms to migrate across the surface. However, consider the example of an InAs-based plasmon waveguide IC laser with SL active regions and more than 4 μm of InAs cladding layers. The growth time is significantly increased from 8 hours to 20 hours when the InAs growth rate is decreased from 0.66 ML/s to 0.22 ML/s. The three-times-longer growth time requires the stability of the growth conditions over a much longer time. Therefore the preferred growth rate depends on the importance of throughput versus crystalline quality and SL uniformity.

4.1.3 Oval Hillock Defect on Homoepitaxial InAs Layers

In the InAs homoepitaxial layers, the oval hillock defect without a pit (T3), round defect (T9), and truncated pyramid defect (T10) were eliminated at optimal growth conditions. However, the pitted oval hillock defect is the dominant defect and remained at a density of $\sim 1\times10^{4}$ cm^{-2} even in the high-quality layers. This kind of defect is similar to the so-called oval defects found in other III-V crystalline materials grown by MBE [93-96]. In the past three decades, oval defects have been most intensively investigated on the GaAs surface with a focus on the origin of the defects and reduction of their density [93-96], but few studies have been made on the InAs surface.

According to the SEM images, the oval shaped hillock is elongated along the primary flat in the [-110] direction and is 1~5 μm in length, and the polyhedral pit in the center has its longest diagonal along the [110] direction (shown in Figures 4.5 (a)-(c)). The size of the largest defect in the layer is proportional to the layer thickness.

Figure 4.6 presents the detailed morphology of the same pitted oval hillock defect as imaged by SEM and AFM. Figures 4.6 (a) and (b) are SEM images captured by a BSD and an in-lens detector, respectively. The in-lens detector is a high-resolution SE detector and was used to reveal the morphology inside of the polyhedral pit. The AFM scan over the same defect and a line scan profile at the center of the pit are shown in Figures 4.6 (c) and (d), respectively. The oval defect rises about 25 nm from the surface and has a central polyhedral pit ≥250 nm deep (possibly limited by tip geometry). A similar polyhedral pit geometry was found in the GaAs oval defect system and was due to propagating stacking faults around the defect regions at the substrate surface [95]. Figure 4.6 (e) is a vertically corrected oblique-view SEM image of the FIB milled cross-section of the same defect. A small dark feature, 20 nm in diameter, appeared about 540 nm beneath the center of this defect in 5 frames (20 nm/frame) and is indicated by a white circle in Figure 4.6 (e). The milling current was 200 pA. Similar dark features appeared at the same depth in several comparably large defects, as shown at the top of Figure 4.6 (e), but were not observed in smaller defects, as shown at the center of Figure 4.6 (e). Higher resolution backscatter and secondary images of similar features have not yet allowed its exact determination, but the SE edge scattering suggests that it is most likely a void located at the substrate-epilayer interface.

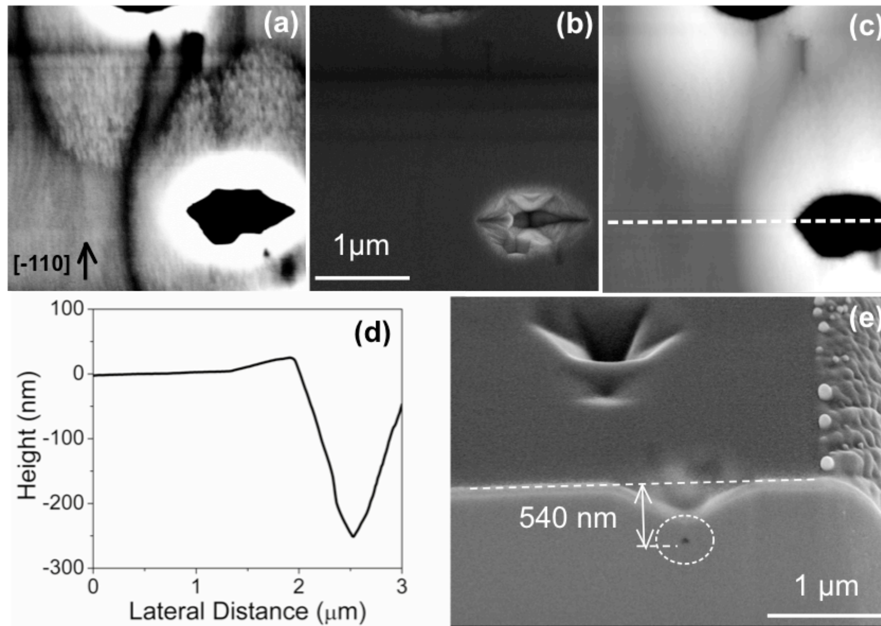

Figure 4.6: Detailed morphology of the same defect in images by SEM and AFM. (a ,b, c) are images of the same defect at the same scale; (a) and (b) are plan-view SEM images captured by an annular backscattered electron detector and the in-lens secondary electron detector, respectively. (c) is a 3 µm × 3 µm AFM scan of the defect. The dashed white line indicates the position of the line profile shown in (d). (d) is the profile crossing the center of the pit which shows that the oval defect rises about 25 nm from the surface and a pit depth of ≥ 250 nm (tip geometry limited). (e) is a vertical height corrected oblique-view SEM image of the defect's cross section obtained by FIB milling at 200 pA with 20 nm steps. A dark feature 540 nm from the surface of the hillock is present in 5 sequential frames and highlighted by a white circle [92].

TEM was also carried out on a specimen prepared by a FIB unit (in a Zeiss Neon EsB dual beam SEM/FIB microscope). One of the unique advantages of the FIB is the ability to select the target area precisely. Figures 4.7 (a) and (b) are SEM images of a typical oval hillock defect in an InAs homoepitaxial layer captured by a BSD and an in-lens detector, respectively. A 40 nm thin section was selected at the center of the defect as shown in Figure 4.7 (a). A few hundred nanometers of e-beam-deposited Platinum (Pt) and about one micrometer of FIB-deposited Pt were used to cover the section and prevent etching or damage in the ensuing FIB etching steps. Two trapezoidal trenches were etched on either side of the section, and then the section was

thinned on both sides using a milling current of 100 pA at 30 keV. The final polish step was done with a current of 100 pA at 5 keV. Figure 4.7 (c) and (d) shows the "lift-out" process of the thin specimen from the bulk layer onto the TEM grid using the micromanipulator.

Figure 4.7 (e) shows the TEM image of the center of the defect with some of the artifacts introduced by the FIB. Note that two layers of deposited Pt cover the defect. The pit is slightly deeper than 500 nm with a basin shaped flat bottom. The location is the same as the void in Figure 4.6 (e) at the substrate-epilayer interface. A dip was found on the right corner of the pit, indicated by an arrow in Figure 4.7 (e), and was suspected to be an etching pit of the wafer that led to the formation of the defect. It is hard to justify the origin of the defect due to the low resolution of image in this specimen. Although no obvious amorphization was observed in the diffraction patterns (not shown), the image still shows FIB damage including a rough surface due to milling and contrast effects due to specimen bending. It has been observed previously in silicon that the sidewall damage was ~21 nm, 2 nm, and 0.5 to 1.5 nm for ion energies of 30 keV, 5 keV, and 2 keV, respectively [144]. Further cleaning/milling is needed to get higher resolution, *i.e.* using a lower milling voltage, so that we can see the epilayer interface (or stacking faults).

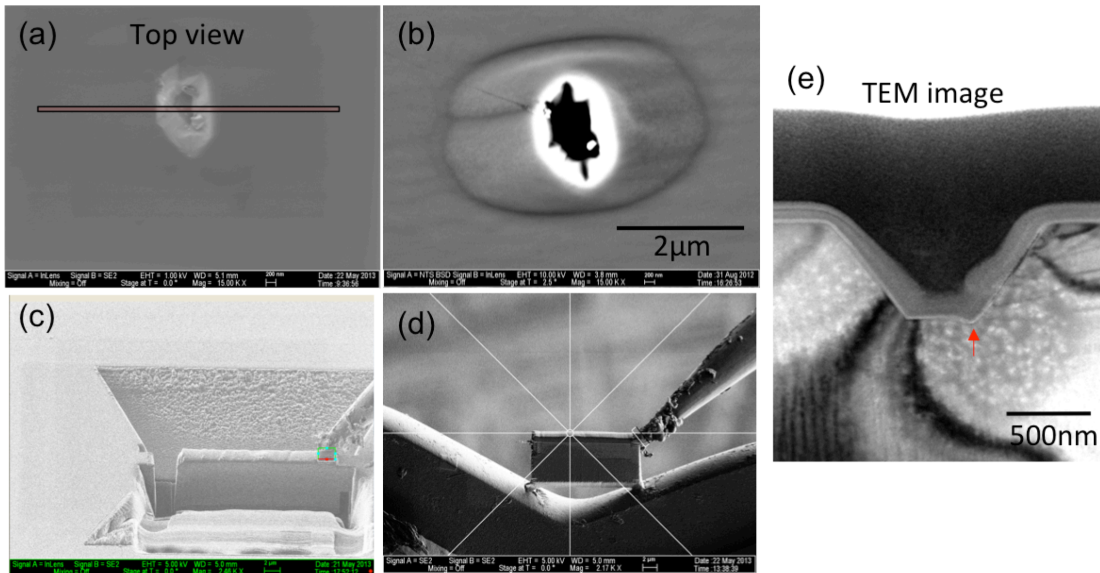

Figure 4.7: SEM and TEM images of an oval hillock defect and the specimen prepared by a focused ion beam (FIB) unit. (a) and (b) are plan-view SEM images captured by an annular backscattered electron detector and the in-lens SE detector, respectively. (c) The tilted SEM image showing removal of the TEM thin section with the micromanipulator. (d) The tilted SEM image showing the placement of the TEM thin section onto a specialized TEM grid. (e) High resolution TEM image of the oval hillock.

To determine the origin of the oval hillock defects, an InAs(001) substrate was examined before and after oxide desorption. Figure 4.8 shows an AFM image of the InAs substrate after the oxide desorption. The surface is rough with an RMS roughness of ~0.6 nm. The small bright dots are suggestive of indium clusters resulting from an In-stabilized oxide desorption process. A particle density of 1×10^3 cm^{-2} was also observed by DIC microscopy after loading the substrate and desorbing the oxide. It is therefore possible that 10 percent of the oval hillock defects may form as a result of surface contamination by particles in the laboratory environment or in the chamber. Moreover, the average etch pit density is $\sim 7 \times 10^3$ cm^{-2} for the InAs substrate (M5/IA/748/S), as specified by the substrate supplier (Wafer Technology LTD). It is plausible that the majority of the oval hillock defects result from the

indium clusters, residual oxide, and the etch pits on the substrate. The defects originating from the substrate surface can affect the device performance because they propagate through the device layers and provide defect related recombination centers for the carriers [145]. However, the defect density in the range of 1×10^4 cm^{-2} should be acceptable for most device applications since the defects usually occupy a small fraction (less than 5%) of the total volume and thus have little effect on the electrical properties of devices [146].

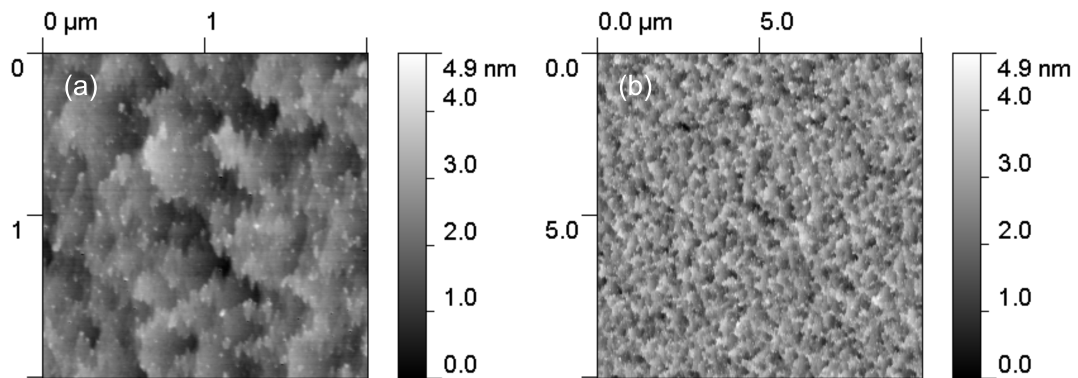

Figure 4.8: (a) 2 μm × 2 μm and (b) 10 μm × 10 μm AFM images of the InAs substrate after oxide desorption.

4.2 MBE Growth and Material Characterization of InAs-based IC Laser Structures

In this section, we will discuss the growth conditions of InAs-based IC laser. The IC laser structures were grown on an epi-ready InAs substrate using an Intevac GEN II MBE system. The growth temperature was monitored by an IRCON Modline 3 infrared pyrometer, which was calibrated using the GaSb surface reconstruction transition from (1×3) to (2×5) [147]. The growth rates for group-III sources (In, Ga and Al) were calibrated by intensity oscillation of RHEED patterns as discussed in Section 2.2.3. And the beam equivalent pressure from the BFM was measured prior to the growth of the IC laser structure. Moderate growth rates were adopted to grow Ga- (~0.45 to 0.3 ML/s in GaAs) and Al-containing (~0.45 ML/s in AlAs) alloys, compared to a low growth rate (0.22 ML/s) for InAs, which was found to be optimum in our previous growths of laser structures [92]. The cracker zones for both As and Sb were kept at 900°C to provide stable beams mostly composed of As_2 and Sb_2, respectively. While the flux ratios of Sb_2/Ga and Sb_2/Al were both maintained around 3, the As_2/In flux ratio was kept near 8 to achieve a slight As_2 overpressure as determined by the observation of an As-rich (2×4) surface under RHEED observation. During growth, the As-valve position was kept constant and only the shutter was used to control the As flux for the different layers. The whole structure was grown at 400°C as a compromise between the optimal growth window for the thick InAs layers and the ultra-thin InAs/AlSb/Ga(In)Sb layers in the cascade regions.

Most of our IC lasers were grown with the growth conditions described above. The wafer qualities may differ from each other due the evolving status of the MBE system. Take the long-wavelength IC laser R110 [26] as an example of a good quality

wafer, whose structure is shown in Figure 4.9. After the oxide desorption process described in Ref. [142] and [92] was completed, the growth was initiated with a 2.3 μm highly *n*-doped (Si, ~7×10^{18} cm^{-3}) InAs layer as a bottom plasmon waveguide cladding layer. Then a (~1.9 μm) unintentionally doped InAs separate confinement layer (SCL) was grown, followed by the 20 cascade stages (46.2 nm per stage) for achieving an optical gain that is sufficient to overcome the likely increased optical loss expected for the longer wavelength range. Next, a top (~2.5 μm) unintentionally doped InAs SCL was grown and the growth ended with 35 nm of highly *n*-doped (Si, ~7×10^{18} cm^{-3}) InAs as the top contact layer. Each cascade stage was composed of an *n*-type electron injector made of InAs/AlSb multiple QWs, an active region (InAs/$Ga_{0.65}In_{0.35}Sb$/InAs, 38/28/33.5 Å, similar to "W"-shape QWs [148]), and a hole injector (GaSb/AlSb QWs). Because InAs has the smallest lattice constant among all the alloys in the IC laser structure, strain balance for the whole structure to the InAs substrate was achieved by using AlAs interfaces in the electron/hole injection regions. Otherwise, there was no intentional shutter sequence at the interfaces between the ultra-thin alloy layers. Some of the InAs QWs in the electron injector were heavily *n*-doped to ~2.3×10^{18} cm^{-3} to rebalance the hole concentration [21]. The entire growth time exceeded 30 hours as the total thickness was close to 8 μm.

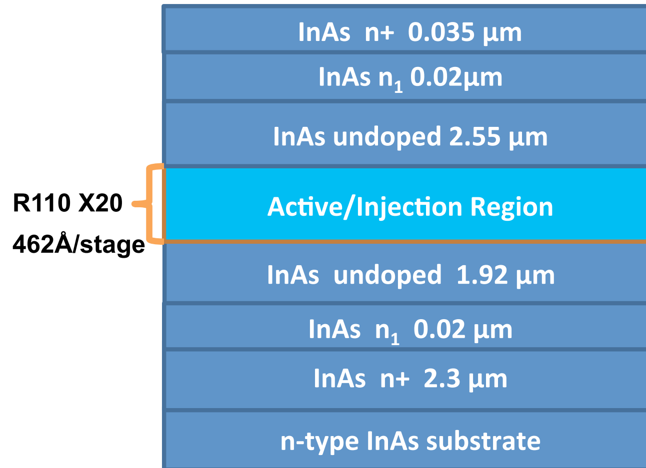

Figure 4.9: Structure of a long-wavelength IC laser, R110.

After growth, the wafer was first assessed by DIC microscopy for surface defects and texture, as shown in Figure 4.10. The surface defect density ranged from 7×10^3 to 2×10^4 cm^{-2} over the wafer. This density is comparable to the average etch pit of ~1.5×10^4 cm^{-2} for the InAs substrate, as specified by the substrate supplier. Despite the long growth time for this thick structure, there was no appreciable increase in the defect density. Besides the limited defect density, the surface looks flat and featureless. The surface smoothness was quantified using an AFM. The AFM image (Figure 4.11) shows uniform steps with atomic step edges, as expected from the InAs substrate miscut of ~0.35° from (100) toward (111)A. On the 2 µm × 2 µm and 10 µm × 10 µm scan area, the RMS roughness is only 0.1 nm.

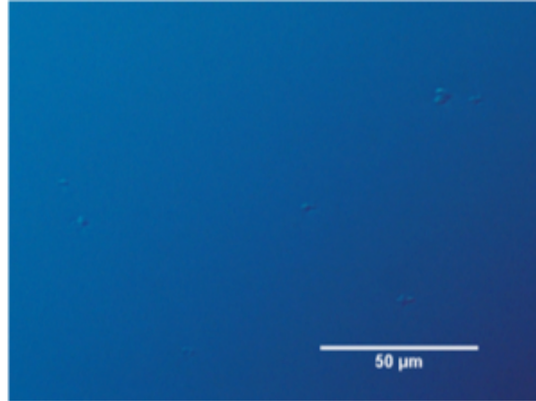

Figure 4.10: A DIC microscopy image of R110.

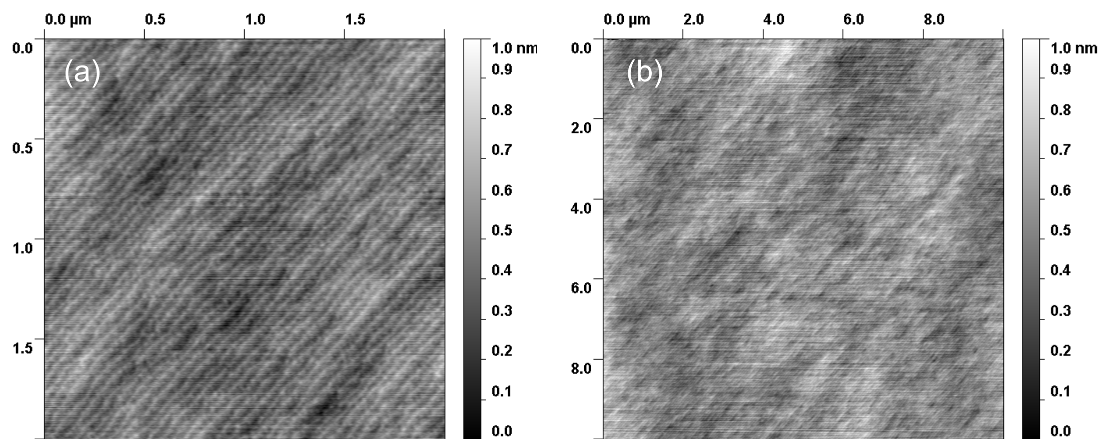

Figure 4.11: AFM images for the IC laser structure in (a) 2 µm × 2 µm and (b) 10 µm × 10 µm area scans.

The crystalline quality of the IC laser structure was characterized using a XRD system. Figure 4.12 (top) shows experimental data from an ω-2θ scan around the InAs (004) reflection for the IC laser structure. Numerous sharp and narrow satellite peaks over ±3° around the InAs substrate peak were observed (>30 orders at each side of the substrate peak with FWHM less than 30 arcsec), indicating that the structure has an excellent crystalline quality. A simulated XRD curve (Figure 4.12, bottom) based on the designed IC laser structure was calculated. The average thickness per stage in the cascade region of the IC laser structure (47.5 nm as derived from the spacing of the

satellite peaks) is only 3% more than design value. The experimental and simulated curves are nearly identical to each other, demonstrating that the MBE growth was well controlled over the long growth time.

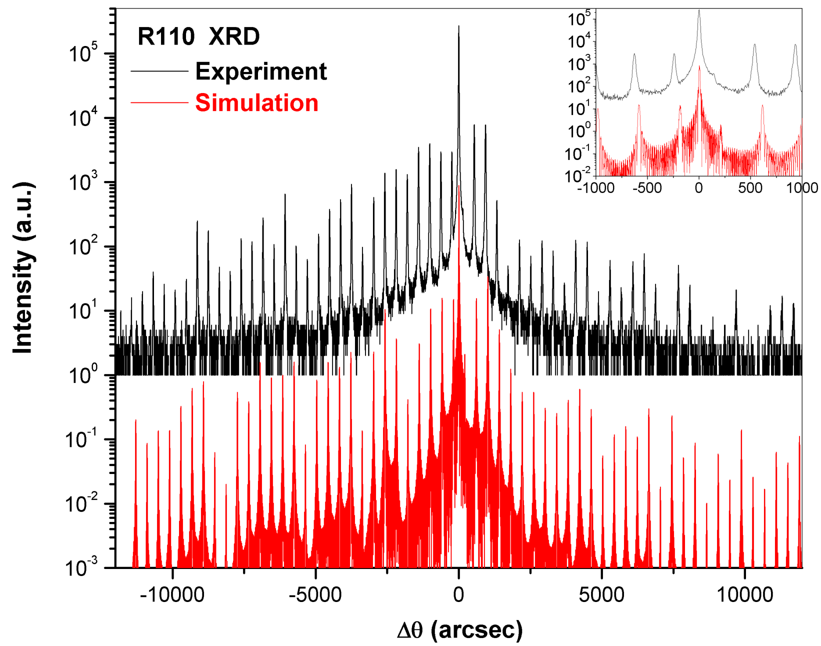

Figure 4.12: (Top) Experimental XRD curve from an ω-2θ scan around the InAs (004) reflection for the IC laser structure. (Bottom) Corresponding simulated XRD curve calculated for the designed structure. The inset shows the data around the substrate.

4.3 Device Performance

In addition to the material characterizations, device characterizations of the grown IC lasers provide further feedback to the growth procedure (both electrical and optical properties). The long-wavelength structure, R110, was fabricated into broad-area lasers with a dielectric-metal hybrid top cladding using a SiO_2 insulating layer and a top metal layer to confine the optical wave [26, 145]. The lasers were mounted epi-side up on a copper heat sink with indium solder and then wire bonded. In cw mode, a 1.6-mm-long device lased near 10.8 μm at 80 K, and was operated at up to 97 K with an emission wavelength at 11.1 μm, as shown in the to Figure 4.13. In pulsed mode (1 μs at 5 kHz), the device lased at temperatures up to 130 K near 11.2 μm (the inset of Figure 4.14), the longest wavelength achieved among III-V interband lasers [26].

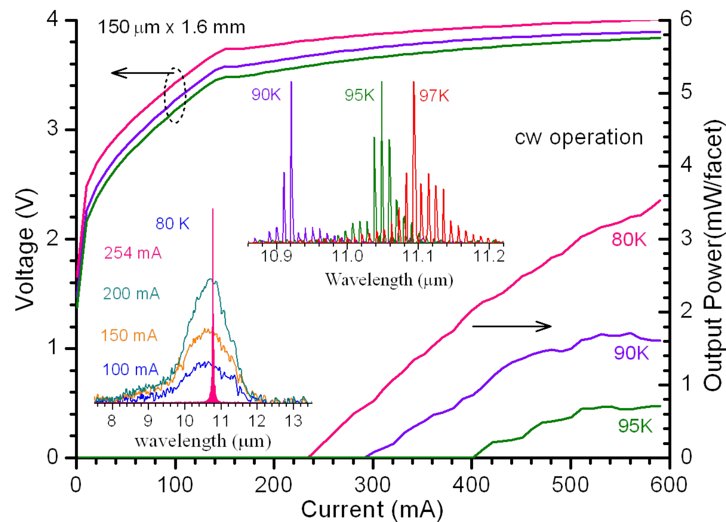

Figure 4.13: Current-voltage-light characteristics for a 150-μm-wide device in cw operation. The insets are its cw lasing spectra at heat-sink temperatures of 80 K to 97 K, and emission spectra at 80 K with several injection currents before threshold [26].

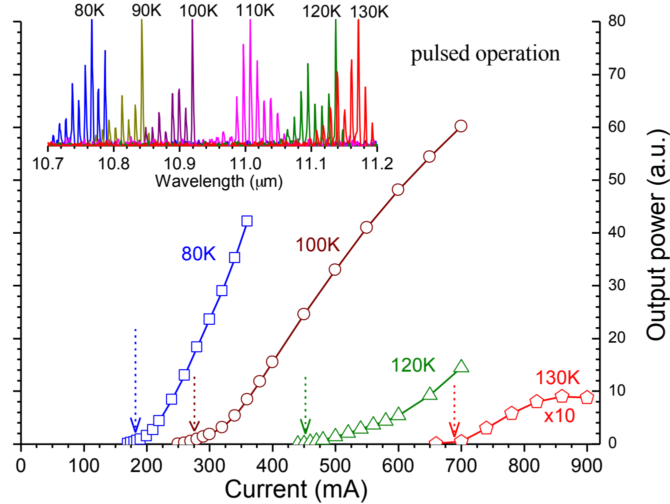

Figure 4.14: Light-current curve for a broad-area IC laser in pulsed mode at temperatures of 80 K to 130 K. The arrows point to threshold currents where spectra were taken. The inset shows the pulsed spectra at several temperatures [26].

However, the threshold current density at 80 K in cw mode was 95 A/cm^2, much higher than the ~10 A/cm^2 for IC lasers near ~9 μm operated under the same conditions [118]. The threshold voltage was 3.91 V at 80 K, corresponding to a voltage efficiency of 61% that is lower than a typical value (*e.g.* 90%) for InAs-based IC lasers. In Figure 4.13, some abnormal behavior was observed in the current-voltage characteristics, *i.e.* the slope that corresponds to the differential resistance had an abrupt drop well before the current reached the threshold [26]. The emission spectra taken at several injection current levels confirmed that the device did not lase before the current reached 95 A/cm^2. The abrupt drop in differential resistance might be caused by the activation of a carrier leakage channel, which increases the threshold current density and reduces the output power. This suggests a correlation with defect related leakage and material non-uniformity, even though no clear material characterization evidence was found. Another possible explanation is a large increase of internal optical loss beyond the common free carrier absorption [26]. Further

investigations are required to achieve a better understanding of the high threshold current density of this long wavelength IC laser.

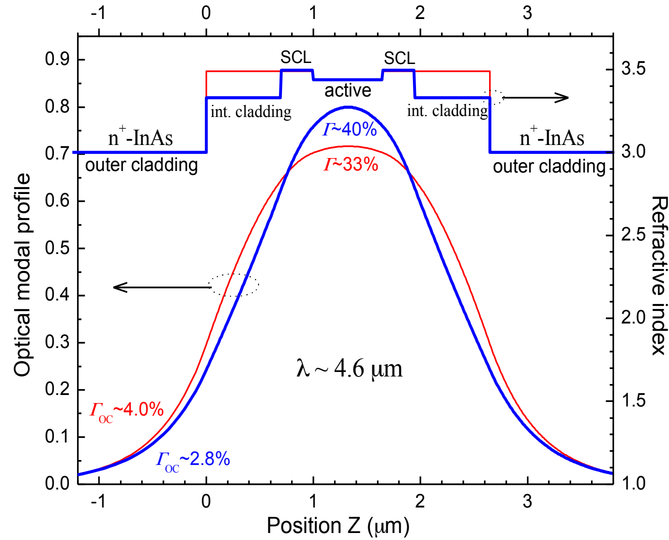

Figure 4.15: Calculated optical modal profiles of IC lasers without (thin lines) and with intermediate superlattice cladding layers (thick lines) [20].

In addition to the long wavelength InAs based IC lasers [26, 118, 145], laser structures grown under similar growth conditions were made into lasers that operated at room temperature in cw mode with the lowest ever threshold current density reported for semiconductor mid-infrared lasers at a similar wavelength [20]. The achievement was enabled by the use of intermediate (int.) SL cladding layers (InAs/AlSb SL) to replace a portion of the undoped InAs separate confinement layers (SCL) as shown in Figure 4.15. The intermediate cladding layer was mainly a 25 Å/23 Å InAs/AlSb SL, in which each AlSb layer contains a 3Å -thick AlAs interface for achieving strain balance. A digitally graded InAs/AlSb(As) QW region was inserted as a transition/connection bridge between the SL intermediate cladding layers and other regions for smoothing carrier transport [20]. More of the optical wave is squeezed into

the center active region, which enhances optical confinement and reduces internal absorption loss [20, 149].

Wafers with different structures (number of stages, InAs SCL thickness, highly doped InAs cap layer thickness, and doping concentrations in electron injectors) were processed into broad-area and narrow-ridge lasers. The device performances were much better than the devices from wafer R125 without the intermediate SL cladding layers as summarized in Table 4.2. For example, a broad-area device from a 15-stage wafer, R140, had a threshold current density J_{th} of 247 A/cm^2 near 4.6 μm at 300 K, the lowest ever reported among mid-IR semiconductor lasers at similar wavelengths. Another broad-area device from a 10-stage wafer, R144, lased at temperatures up to 377 K near 5.1μm, the highest operating temperature reported for electrically pumped interband lasers at this wavelength [20].

Table 4.2: Parameters of wafer structures and pulsed performance of broad-area lasers.

Wafer	No. of stages	Top n^+-InAs layer (nm)	Int. SL clad. (μm)	InAs SCL (μm)	Doping (cm^{-3}) in e injector	Cavity length (mm)	Lowest J_{th} (A/cm^2) at 300 K	λ (μm) at 300 K	J_{th} (kA/cm^2) at T_{max} (K)
R125	15	35	0	1.5/1.3	3.3×10^{18}	2.0	393	5.1	1.6@340
R136		800	1.0	0.35	3.3×10^{18}	1.5	340	5.2	1.6@372
R140		35		0.35	3.3×10^{18}	2.0	247	4.6	2.0@370
R142	12	700		0.39	3.3×10^{18}	2.0	290	4.75	1.8@359
R143		700		0.39	1.6×10^{18}	2.0	278	4.5	3.9@376
R144	10	800		0.43	3.3×10^{18}	2.0	290	4.7	3.1@377
R145		800		0.43	1.6×10^{18}	2.0	330	4.6	2.0@360

However, the device performance results from Table 4.2 do not provide a clear indication of how the design differences in the structures would affect the threshold current density. This may be attributed to variations of material quality and uniformity. The IC laser structures with intermediate SL cladding layers were grown when the

MBE chamber was in a poor status and their material quality was not as good as in the previous growth campaign (*e.g.*, wafer R125). While R125 has a defect density of 1×10^{3} cm^{-2} for most of its surface (only the edge area has 1×10^{6} cm^{-2}); the wafers with intermediate SL cladding layers has worse surfaces with high defect regions and even foggy areas, as summarized in Table 4.3. Figure 4.16 shows the comparison between the experimental XRD curves of R136, R143, R144 and R125. Compared with R125, the wafers with the intermediate SL layer (R136, R143, and R144) have wider and less intense satellite peaks, indicating an inferior crystalline quality. The satellite peaks with wider separations (~3850 arcsec) correspond to the intermediate SL with a designed period of 48Å. Their large FWHMs (some of them are > 80 arcsec) indicate a poor reproducibility and consistency in the growth flux of the bottom and top intermediate SL layers. This could be related to an unstable Al cell in the GEN II system, whose flux might fluctuate up to 8% during a long growth time.

Nevertheless, it is very evident that the lasers made from the later wafers exhibited significantly improved device performance, which validates the advantages of the intermediate SL cladding waveguide structure shown in Figure 4.15. With a better MBE growth quality, an even superior device performance can be achieved at higher operation temperatures and longer wavelengths.

Table 4.3: Surface morphology as assessed by the DIC microscopy and superlattice parameters as determined by XRD.

wafer	Defect density (cm^{-2})	Surface Morphology	XRD Design (Å)	XRD Meas. (Å)	XRD Error	FWHM (arcsec) sub	FWHM -2nd	FWHM -1st	FWHM 1st	FWHM 2nd
R125	1E3-1E6	Most of area low defect density, high on the edge.	420	428	1.9%	20	30	31	31	30
R136	rough	Long foggy strips, large metal-centered defects	48	50.5	5.2%	61	69	67	79	109
			418	434.4	3.9%		65	66	66	65
R140	rough	rough	48	48.4	0.8%	29	116	39	124	-
			418	420.5	0.6%		65	91	59	65
R142	5E3-1E6	Most of the area high defect density	48	47.4	-1.3%	29	29	37	85	77
			417	414.0	-0.7%		38	39	39	41
R143	1E4	Most of the area low defect density, foggy corner	48	48.3	0.6%	29	38	81	47	71
			417	414.6	-0.6%		37	40	39	39
R144	6E3-1E6	Half area high defect density, foggy corner	48	50.8	6%	24	29	28	59	34
			417	428.1	2.7%		43	47	43	43
R145	1E4-1E6	1/3 area high defect density, foggy corner	48	48.7	1.5%	23	27	27	33	-
			417	416.0	-0.2%		41	46	45	43

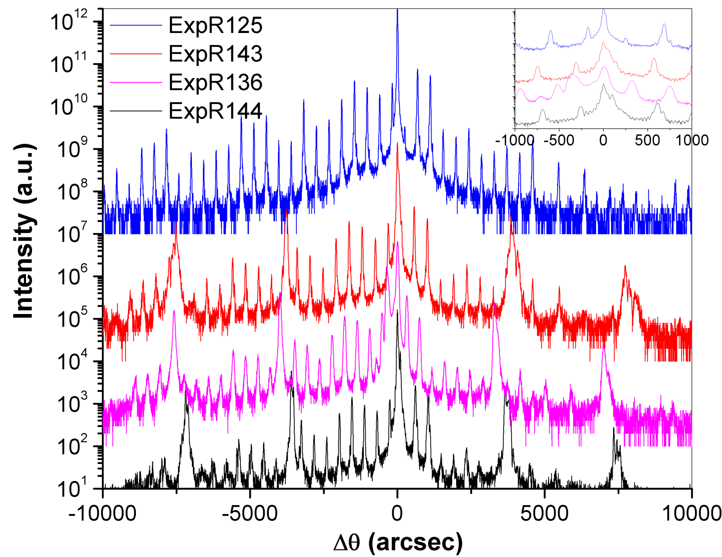

Figure 4.16: Experimental XRD curves from an ω-2θ scan around the InAs (004) reflection for the IC laser structures R125, R143, R136, and R144 (from top to bottom). The inset shows the scans data around the substrate.

Chapter 5 MBE Growth of ICPD and ICPV Structures

5.1 Structures with InAs/GaSb Superlattices

In this chapter we will discuss the MBE growth of ICPD and ICPV structures. Since both were developed based on the idea of the IC lasers, they share the same material system, which implies no significant difference in growth conditions. They are grown on nominally undoped p-type GaSb (100) substrates and utilize InAs/GaSb SLs as absorbers. The electron and hole barriers are composed of GaSb/AlSb layers and InAs/AlInSb layers, respectively. The barriers sandwich the absorber layers to impose a preferred carrier flow direction and form recombination interfaces.

For the structures grown in the GEN II system, the substrate temperature was monitored by a pyrometer. The epi-ready GaSb substrate was loaded into the MBE system, directly followed by several hours of outgassing in the buffer chamber at a substrate temperature of 250˚C. After the substrate was transferred into the growth chamber, the surface oxide layer was desorbed at 530-540˚C under an Sb_2 overpressure for ~ 10 minutes, where a 3× RHEED pattern is visible on the [-110] azimuths. The Sb overpressure was the same as used in the GaSb growth (~4.5×10^{-7} Torr in the GEN II). A 0.35 to 0.5 μm thick GaSb buffer layer was first deposited at ~470˚C, followed by the growth of cascade stages and an InAs or GaSb top-contact layer at ~415˚C. In the absorber section of the cascade stages, a very thin layer of InSb was intentionally grown at the interface between InAs and GaSb layers (GaSb-on-InAs) in each SL period to achieve a strain-balanced condition and allow the growth of a thick absorber layer; more details will be discussed in Section 5.3. The growth rates were 0.22 ML/s for InAs with a V/III beam equivalent pressure ratio of 8, and

0.52 ML/s for GaSb with a V/III ratio of 3. In each stage, a portion of the absorber was p-type doped in the GaSb layers with beryllium at a targeted dopant concentration of 1.6×10^{16} to 5.1×10^{16} cm^{-3}.

Due to the difference in the chamber geometry and the ion gauge sensitivity, the optimal V/III beam equivalent pressure ratio in the GENxplor is different, even though the growth conditions were intentionally kept the same in the two MBE systems, e.g. the As_2 overpressure is in As-rich condition and ~30% higher than the In-rich boundary. A V/III beam equivalent pressure ratio of 3 and 4 were used for GaSb and InAs, respectively. However, it is very crucial to minimize the As_2 overpressure to reduce excess arsenic incorporation into the GaSb layers while still maintaining an As-rich environment. Consider wafers Y010D, Y011D and Y012D. They are grown consecutively in the GENxplor with the same growth conditions except the As_2 overpressure was varied. Y010D has an As_2/In ratio of ~4 and a tensile perpendicular mismatch of -0.09%. By reducing the As_2/In ratio from ~4 to ~3.5, Y011D and Y012D have a mismatch of almost zero. Figure 5.1 compares the experimental XRD curves for Y010D with Y011D and Y012D. An ω-2θ scan was taken around the GaSb (004) reflection for each of them. The inset shows the data near the substrate peak. As shown in the figure, Y010D has a zero order peak at 115 arcsec on the right side of the substrate peak, while the zero order and substrate peaks are aligned for Y011D and Y012D. Note that the three wafers have different structures but the same InAs/GaSb SL parameters.

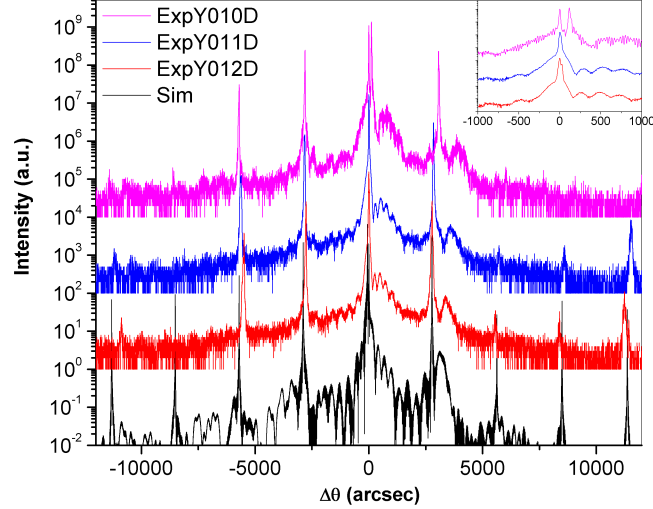

Figure 5.1: Experimental XRD scans from an ω-2θ scan around the GaSb (004) reflection for IC laser structures (Y010D, Y011D, and Y012D). Corresponding simulated XRD scan calculated for the designed structure (bottom curve). The inset shows the scans data near the substrate peak.

Take the two-stage ICPV structure R103 as an example of the growth of IC structure with InAs/GaSb SLs. The structure on GaSb substrate is shown in Figure 5.2 (a). The absorbers in this two-stage ICPV structure were, in the order from the surface to the substrate, SLs of 126 (~605 nm) and 148 (~710 nm) periods. By making the absorber that was located further from the surface thicker, we expected to achieve a reasonable matching of the carrier generation rate in each stage. The electron barrier is composed of alternating layers of AlSb and GaSb with layer thicknesses (in Å) of **15**/32/**15**/40/**15**/53, where the normal and bold numbers refer to the GaSb and AlSb layers, respectively. The hole barrier is a series of InAs/AlInSb layers with thicknesses of 20/**67**/20/**58**/21/**50.3**/22/**44.7**/23/**39**/24/**35**/24/**32**/29, where the normal, bold, and underlined numbers represent AlInSb layers, InAs wells, and AlSb barriers, respectively.

The growth of R103 was carried out in the GEN II. Figure 5.2 (b) shows a representative XRD curve obtained by an ω-2θ scan around the 004 reflection of the two-stage ICPV structure. The FWHM of the zero order peak is about 20 arcsec. Based on the data, the mismatch between the GaSb substrate and the average lattice constant of the InAs/GaSb SL is estimated to be about 140 ppm (0.014%). The SL period calculated from the satellite peaks is 1.2% larger than the designed period. The morphology of the ICPV wafers was studied by using DIC microscopy and *ex situ* AFM. A defect density of 5×10^3 cm^{-2} was determined from DIC microscopy images. The AFM image of the two-stage ICPV structure's surface in Figure 5.3 yields a RMS surface roughness of 0.5 nm. Slip-lines oriented in the [1-10] direction can be seen in the image, which are probably due to thermal and mechanical stress during the growth, as mentioned in Section 3.2.2 [109].

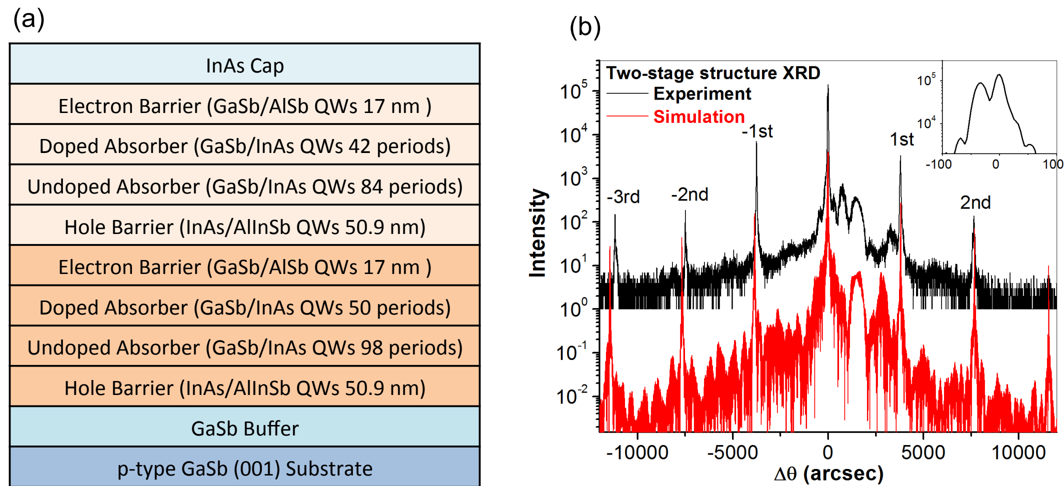

Figure 5.2: (a) The two-stage ICPV structure R103, grown on a GaSb (001) substrate. (b) X-ray diffraction data (black) and a corresponding simulation (red) for an ω-2θ scan around the 004 reflection. The inset shows the experimental data near the substrate peak and the zero order peak [58].

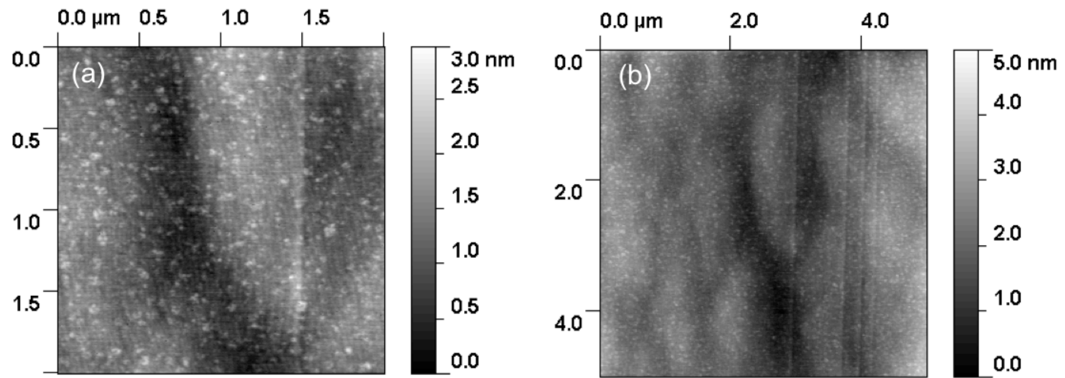

Figure 5.3: AFM image taken from the surface of the two-stage ICPV structure over (a) a 2 µm × 2 µm and (b) a 5 µm × 5 µm areas.

5.2 Device Performance of the Two and Three-stage ICPV Devices

In order to study the advantages of the multiple discrete absorber structures, a three-stage structure, R104, was grown under the same growth conditions as the two-stage structure, R103. The absorbers had 132 (~634 nm), 157 (~754 nm) and 195 (~936 nm) periods. The three-stage ICPV structure exhibited a similar crystalline quality and surface morphology to the two-stage structure. Wafers R103 (two-stage) and R104 (three-stage) were processed into square mesa devices [58].

The relative response of the ICPV devices was measured using a Nicolet 8700 Fourier Transform Infrared (FTIR) spectrometer. The devices were illuminated by a blackbody source with T=900 K to obtain the calibrated zero-bias quantum efficiency (QE). Here, QE is defined as the total number of photo-carriers that are generated and collected in any stage per incident photon. Figure 5.4 shows the QE curves for both a two- and three-stage device at T=300 K and 350 K. A cutoff wavelength of 5.3 μm at room temperature was measured, corresponding to a bandgap of 0.23 eV, which enables energy conversion of long-wavelength infrared photons from a low-temperature heat source (<1000 K). The cutoff wavelength was deduced as the location where the QE began a substantial increase as the wavelength decreased. The cutoff wavelength of the two- and three-stage devices showed that they have very similar bandgaps at all temperatures (see the inset to Figure 5.4). The value agrees with the expected value from the designed InAs/GaSb SL parameters. The results reported for QE are within a ±5% uncertainty range. Our three-stage device showed a higher QE, as expected from the larger overall thickness of the absorber regions and the induced higher photon absorption.

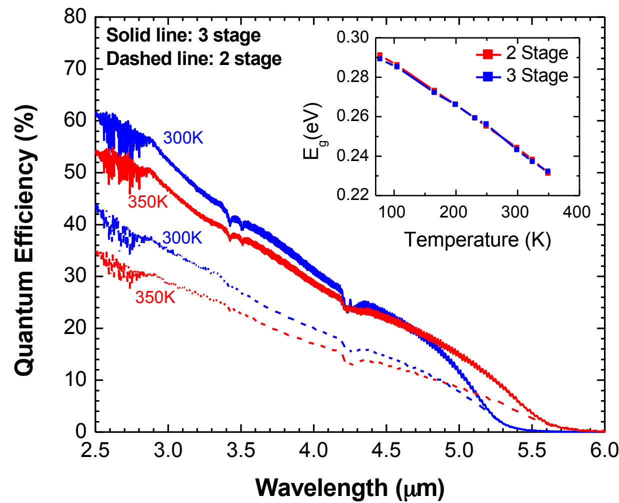

Figure 5.4: Quantum efficiency for two- and three-stage ICPV devices measured at T=300 K and 350 K. The inset shows the bandgap corresponding to a cutoff wavelength at different temperatures for both devices [58].

An IC laser with an emission energy slightly above the bandgap was used to simulate a narrow-band selective emitter with a relatively high intensity. This laser was cooled to 78 K, where it had an emission wavelength of ~4.3 μm. Figure 5.5 shows the current-voltage characteristics of the ICPV devices at temperatures of 300 K and 340 K illuminated by this laser. The larger open circuit voltage of a three-stage device (153 mV at 300 K) compared to that of a two-stage device (107 mV at 300 K) confirms that each stage contributes to a higher open circuit voltage in a multiple-stage ICPV device.

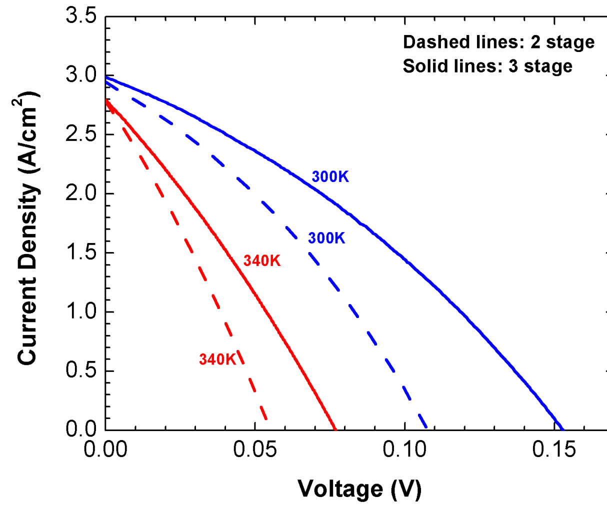

Figure 5.5: Current density versus voltage at T=300 K and 340 K for both two- and three-stage devices. An IC laser with an emission wavelength of 4.3 µm was used for illumination [58].

Figure 5.6 shows plots of V_{oc} and J_{sc} for two- and three-stage devices at different temperatures. At 78 K, the V_{oc} of 0.76 V for the three-stage device exceeded the single bandgap determined value (E_g/e~0.29 V) with a voltage efficiency (eV_{oc}/3E_g) of 87%. The monotonic decrease in the V_{oc} values with increasing temperature was mainly caused by the higher dark current and shorter carrier lifetime at higher temperatures. From Figure 5.6, one can see that the photocurrent densities for the two- and three-stage devices were nearly equal. Because the total thickness of the absorber layers in the first two stages of the three-stage device is only about 73 nm (~5.5%) larger than that of the two-stage device, the photo-generated carrier concentrations in the first two stages of the three-stage device and the two-stage device are approximately the same. Therefore, the roughly equal photocurrent density obtained from both two-stage and three-stage devices suggests that a very high level of current

matching (>90%) between cascade stages was achieved for both devices at most of the measurement temperatures.

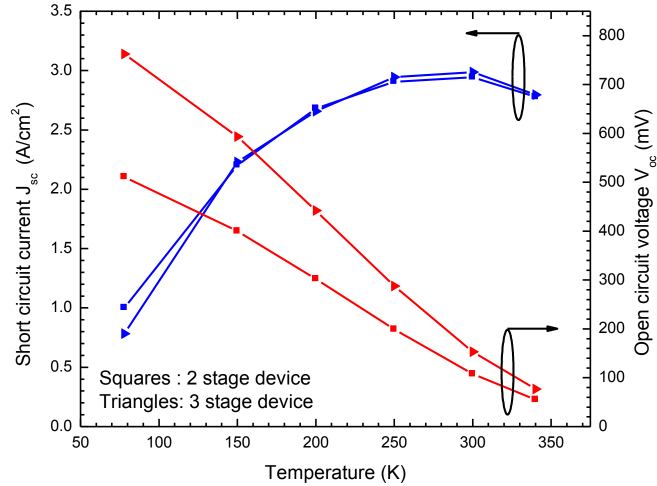

Figure 5.6: Short circuit current density J_{sc} and open circuit voltage V_{oc} for two- and three-stage devices at different temperatures. An IC laser with the same output power was used for these measurements [58].

To summarize, XRD measurements indicate that the MBE growth of the two structures match the design with a good reproducibility. Both the two- and three-stage PV devices have been demonstrated to be capable of high open-circuit voltages even with a cutoff wavelength of 5.3 μm at room temperature, which is, to our knowledge, the longest cutoff wavelength reported for room temperature operation of a TPV device. Our experiments demonstrate the advantages of the interband cascade approach for TPV cell design.

5.3 MBE Growth of InAs/GaSb Superlattice Absorbers with Different Interface Arrangements

5.3.1 Interface of InAs/GaSb Superlattice

In this section, we discuss the interfaces growth of InAs/GaSb SLs on GaSb substrate. Since InAs and GaSb have no common species of atom, the heterojunction interface can be either GaAs-like or InSb-like, depending on growth procedures. In order to balance the in-plane tensile strain for InAs layers (lattice constant a=0.60584 nm) on the GaSb substrate (a=0.60959 nm), some InSb-like (a=0.64794 nm) interfaces must be included. In addition, if some of the SL interfaces are GaAs-like (a=0.56540 nm), an equal amount of InSb should be included for strain balancing. For group-V rich conditions, one might expect InAs-on-GaSb and GaSb-on-InAs to naturally form interfaces that are InSb-like and GaAs-like, respectively. In reality, the interface formation can be influenced by the segregation and intermixing of atoms in those layers, which has been described by different methods [67, 150-154]. A naturally formed GaSb-on-InAs interface has been confirmed to be GaAs-like by Krishnamurthy *et al*. [155]. Therefore it is preferable to force an InSb-like interface at the GaSb-on-InAs interface to reduce the GaAs-like bond that naturally forms at that interface [76]. Once strain balance is achieved, the critical thickness of the SL can be much larger than if there were no interface strain [156].

For long wavelength infrared detectors, strain balancing in SL growth can be more challenging because a thicker InAs layer is required, which will induce a larger tensile strain in the SL. A thicker InSb interface layer is needed to balance this tensile strain, but the interface will degrade if the InSb layer is too thick. Studies of InSb quantum dot formation on a GaSb surface (6.3% lattice mismatch) found that the 2D

to 3D transition occurs at 1.7 to 2.8 ML, depending upon growth conditions [157]. Studies of InAs/GaSb SLs with a thin InSb layer inserted after the growth of each GaSb layer imply that the interface can roughen even if the InSb deposition is below 1.7 ML. According to XRD, AFM, or photoresponse measurements, the interface quality of the completed SL structure was degraded when the InSb deposition exceeded a threshold of 0.45 ML [158], 1.0 ML [79], or 1.1 ML [159]. The XRD data for SLs that exceeded the threshold InSb thickness no longer had the interference fringes that were observed in SLs with less InSb [79, 160], and exhibited larger FWHM for their SL satellite peaks [158, 159]. AFM measurements on the surface of the completed SLs indicated significantly increased surface roughness when the threshold InSb thickness was exceeded [79, 160]. These characterizations suggest an interface degradation that would not benefit the device performance.

One strategy to lessen the possibility of forming a degraded interface is to divide the thickness of a continuous InSb layer at one interface (GaSb-on-InAs) to both interfaces [159, 161]. With the goal of improving the performance of long wavelength type-II SL photodetectors, we tested this strategy by conducting a detailed comparison between materials and devices with two interface structures, one with a nominal InSb layer (~1.2 ML) at the GaSb-on-InAs interfaces and another with two thinner nominal InSb layers (~0.6 ML) at both GaSb-on-InAs and InAs-on-GaSb interfaces. The InSb thickness of 1.2 ML was chosen to strain balance an InAs/GaSb SL designed for a cut-off wavelength of ~9 μm. By incorporating the SLs into an ICPD structure, we were able to study not only the material properties but also their impact on the device performance.

5.3.2 ICPD Structures with Different Interface Arrangements

The two-stage ICPD structures for this study were grown in the GEN II with similar growth conditions that were described in Section 5.2 [162]. The structure is shown schematically in Figure 5.7, where each stage consists of an InAs/GaSb (~12 ML / 7 ML) SL absorber sandwiched between electron and hole barriers. The electron barrier is a series of GaSb/AlSb layers with thicknesses (in Angstroms) of **15**/32/**15**/43/**15**/58, where the normal and bold numbers represent the GaSb quantum wells and AlSb barriers, respectively. The hole barrier is a series of InAs/AlInSb layers with thicknesses of 20/**72**/20/**63**/21/**58**/22/**55**/22/**53**/22/**51**/22/**50**/25, where the normal, bold, and underlined numbers represent AlInSb layers, InAs wells, and AlSb barriers, respectively. In each stage, the GaSb layers in the lower half of the SL absorber are p-doped with beryllium at 3.5×10^{16} cm^{-3}; thus electrons are expected to be the minority carrier in the absorber. In order to facilitate the collection of electrons in the "front illumination" geometry [44], the hole barrier was grown on top of the absorber so that the electron collection point for each stage (the interface between the hole barrier and the electron barrier or the contact layer) would be closer to the incident light. The bottom absorber (756.4 nm) is designed to be thicker than the top one (620.0 nm) to compensate for the attenuated light intensity in the bottom stage.

InAs Cap
Hole Barrier (InAs/AlSb 58 nm)
Undoped Absorber (GaSb/InAs QWs 50 periods)
Doped Absorber (GaSb/InAs QWs 50 periods)
Electron Barrier (GaSb/AlSb QWs 18 nm)
Hole Barrier (InAs/AlSb 58 nm)
Undoped Absorber (GaSb/InAs QWs 61 periods)
Doped Absorber (GaSb/InAs QWs 61 periods)
Electron Barrier (GaSb/AlSb QWs 18 nm)
GaSb Buffer
Undoped p-type GaSb (001) Substrate

Figure 5.7: Schematic diagram of a two-stage ICPD [162].

Two structures were designed in an attempt to investigate how the interface arrangements would affect material quality and corresponding device performance. Wafers I-2 and I-1 were grown under the same conditions within two days. The interface arrangements were designed differently as shown in Figure 5.8. Both the GaSb-on-InAs and InAs-on-GaSb interfaces were forced to be InSb-like (~0.6 ML for each interface) in I-2, while only the GaSb-on-InAs interfaces were forced to be InSb-like (~1.2 ML) in I-1. Note that both structures had the same total nominal InSb layer thickness of 1.2 ML in the SL period. Based on previous studies [79, 158-160], a continuous InSb layer of 1.2 ML inserted in the SL would degrade the structure quality. The specified monolayer thickness of InSb serves as an estimate rather than a precise description. In the real situation, a nominal deposition of one monolayer may not result in complete surface coverage due to a tendency to form islands. The nominal InSb layers were intentionally grown without any interruption using the same shutter sequences as in reference [163]. For example, the InAs-on-GaSb interface was formed by closing the Ga shutter while simultaneously opening the In shutter upon completing the GaSb layer. After growth of 0.6 or 1.2 ML of InSb, the As shutter was opened

while simultaneously closing the Sb shutter to start growth of the InAs layer. The schematic of shutter sequences of I-1 is shown in Figure 5.9. This method may not provide the most abrupt interface compared to soaking [150, 160, 164] or migration-enhanced epitaxy (MEE) [66, 75, 165]. However, it has a higher effective growth rate (shorter time to complete one period), which is expected to result in a SL minority carrier lifetime that is longer than in SLs grown with MEE interfaces using the same InAs and GaSb growth rates [75].

Figure 5.8: InAs/GaSb superlattice structure (one period) with different interface arrangements.

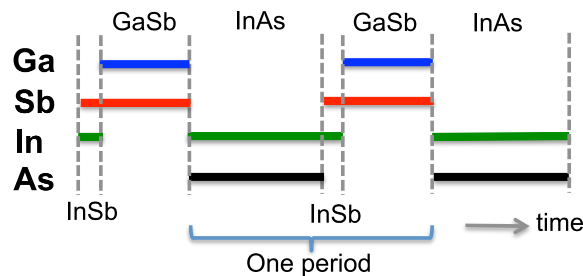

Figure 5.9: Shutter sequences of structure I-1.

After the growth, the two wafers were processed together with the same fabrication recipe into square mesa devices. A two-layer passivation consisting of 170 nm of Si_3N_4 followed by 137 nm of SiO_2 was used for these detectors.

5.3.3 Material Characterization

The surface morphology of the two wafers was studied and compared using DIC microscopy and AFM. Figures 5.10 (a) and (b) are DIC microscopy images of I-2 and I-1, respectively, showing typical oval-shaped defects. Both wafers had an average surface defect density (mostly oval defects) of 5×10^{3} cm^{-2}, based on the DIC microscopy images. Typical AFM images of I-2 and I-1 are shown in Figure 5.10 (c) and (d), respectively. Previous studies [79, 160] had led us to expect the RMS roughness to be several times larger for I-1 than I-2. However, both images show smooth surface with clear atomic steps and a RMS roughness of 0.2 nm and 0.1 nm for I-2 and I-1, respectively. Our result implies that the interface roughness is similar for I-1 and I-2. Spots that are 1-3 nm tall and ~50 nm wide with a density of 3×10^{8} cm^{-2} were only found on wafer I-2, not on I-1. We suspect these spots originated from the 35 nm InAs capping layer instead of structural defects, which tend to propagate throughout the growth and lead to features with much larger characteristic widths and heights [92, 151, 166]. On the other hand, similar spots have been found on an InAs substrate after oxide desorption due to In clusters forming as the As_2 desorbs [92]. For I-2, this may have happened during the reduction of the As_2 overpressure after the growth was completed.

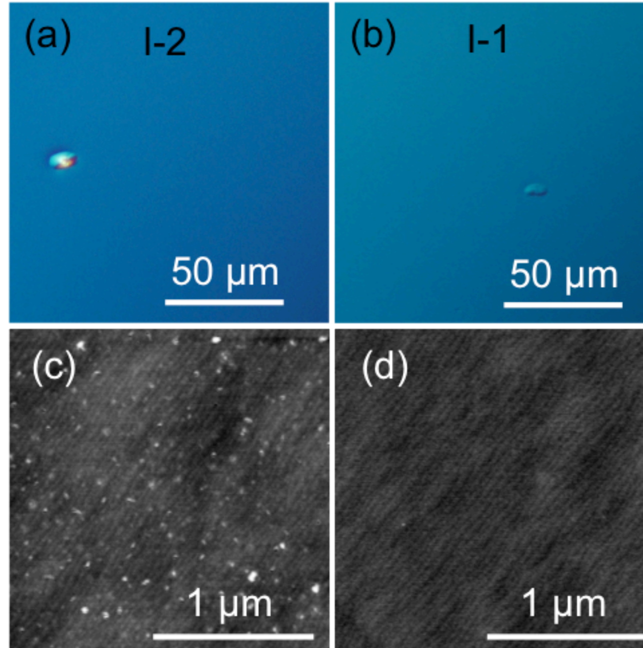

Figure 5.10: DIC microscopy images of wafer (a) I-2 and (b) I-1. AFM images taken of the surface of (c) I-2 (RMS=2 Å) and (d) I-1 (RMS=1 Å). The lateral scale is 2 µm ×2 µm and the gray scale is 3 nm [162].

Wafer crystalline quality was characterized by using XRD measurements. Previous studies [79, 158-160] used the strength of interference fringes and the sharpness of satellite peaks to infer differences in interface roughness for different structures. Figure 5.11 shows the measured diffraction patterns for (004) ω-2θ scans of I-2 and I-1. It also shows a simulation of I-1, which includes one interfacial InSb layer (1.2 ML) per SL period. The series of sharp peaks are satellite peaks due to the SLs while the broad peak on the right side of the substrate peak at ~1530 arcsec corresponds to the InAs cap layer. Table 5.1 lists the information determined from the experimental scans, including: the SL period, the lattice mismatch of the SL to the substrate in growth direction, and the intensity and the FWHM of the zero order (0th) and the first order ($\pm 1^{st}$) SL satellite peaks, as well as the substrate peak (sub). The measured SL period for I-2 (I-1) was 6.11 ± 0.03 nm (6.20 ± 0.03 nm), which was

only ~1.5% (~0%) smaller than the designed period of ~6.2 nm. The zero order SL peak position suggested an in-plane tensile strain in the structure and led to a similarly small mismatch of -0.32% and -0.25% for I-2 and I-1, respectively in the growth direction. Note that the designed SL had an average lattice constant matched to the GaSb substrate. The observed mismatch was probably due to the unintentional incorporation of As in both wafers, since the As valve was kept open during the entire growth. We expect the arsenic incorporation fraction was similarly small for both wafers ($GaAs_xSb_{1-x}$ and $InAs_xSb_{1-x}$ with $0.038<x<0.050$ instead $x=0$) because the growth conditions were nominally identical. An increase in the thickness of the InSb interface layers would reduce the mismatch.

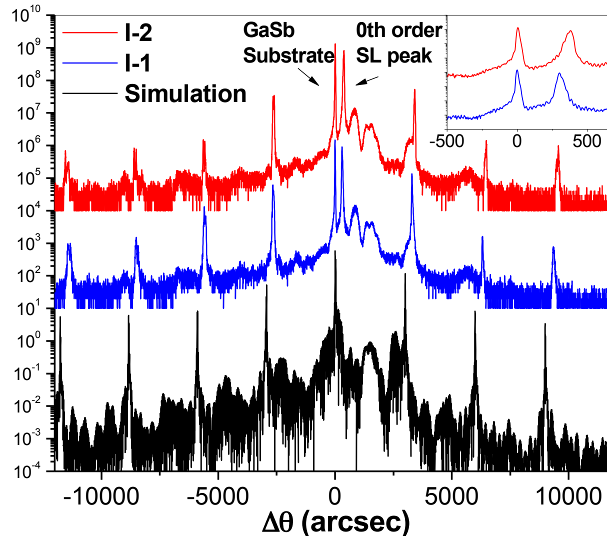

Figure 5.11: X-ray diffraction data for wafers I-2 (top) and I-1 (middle) and a corresponding simulation (bottom) of an ω-2θ scan around the 004 reflection with the interfacial InSb layers. The scans are offset for clarity. The inset shows the experimental data near the substrate peak and the zero order peak [162].

Table 5.1: XRD information from the experimental data, including the deduced superlattice period, the period error compared with the designed period of 62 Å, the perpendicular mismatch of the average superlattice lattice constant in the growth direction compared with the GaSb substrate, the intensity and the FWHM of the first satellite peak on the left (-1st), zero order satellite peak in the center (0th), the first satellite peak on the right (1st), and the substrate peak (sub). The intensity of all peaks is normalized to their substrate peak [162].

	Deduced period (nm)	Period error	Perpendicular mismatch	FWHM (arcsec)				Normalized Intensity			
				-1st	0th	1st	sub	-1st	0th	1st	sub
I-2	6.11±0.03	-1.5%	-0.32%	29	42	32	18	0.03	0.56	0.04	1.00
I-1	6.20±0.03	0%	-0.25%	54	26	28	16	0.04	0.61	0.09	1.00

The intensity and FWHM of the satellite peaks are sensitive to the interface quality. The FWHMs of I-2 and I-1 were similar and indicate good crystalline quality. In order to compare the peak intensities from the two structures, the substrate peak was used as a reference because the substrate quality should be the same. The intensity of the substrate peak was set to one in Table 5.1. The intensities of the SL peaks for I-1 were only slightly higher than for I-2, and nearly indistinguishable on the log scale. In addition, neither I-1 nor I-2 showed strong interference fringes. Therefore, we believe the interface qualities are comparable.

5.3.4 Device Characterization

The dark current was measured to evaluate the performance of photodetector devices made from the two wafers. A cold shield blocked background radiation from reaching the device in the cryostat. At 78 K, I-2 (I-1) had an average dark current density of 4.3×10^{-3} A/cm^2 (2.0×10^{-3} A/cm^2) at a bias of 50 mV and an average R_0A of 32.7 Ω cm^2 (58.3 Ω cm^2) for 17 (16) detectors. I-1 showed a slightly lower dark current density than I-2 at 78 K. The dark current density versus bias voltage for the best performing devices from I-2 and I-1 are shown in Figure 5.11. As mentioned

above, the ICPD structures were designed to have electrons as minority carriers that flow towards the top contact. In this configuration, a positive voltage corresponds to a reverse bias of the photodetector. It is worth noting that the current at a large forward bias (negative voltage in Figure 5.12) was affected by series resistance from the contacts and metal leads, which hampers the analysis of the intrinsic detector properties. The dark current densities at a low bias were comparable from 78 K to 200 K for the representative devices from both wafers. The dark current density at 50 mV was 3.5×10^{-4} (3.0×10^{-4}) A/cm^2 at 78 K and 0.7 (1.0) A/cm^2 at 200 K for I-2 (I-1).

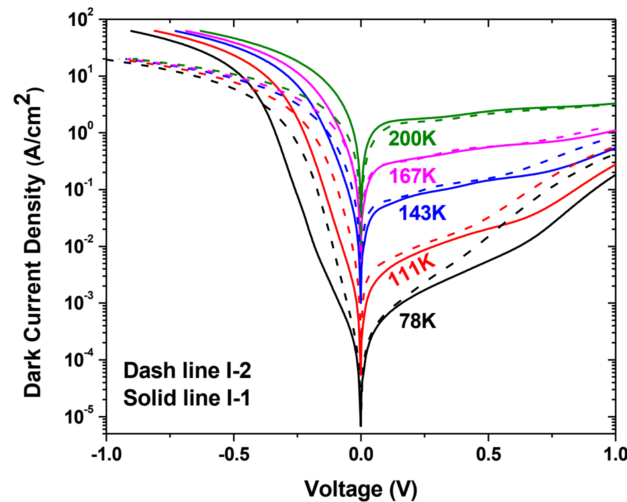

Figure 5.12: Dark current density versus voltage for detectors made from I-2 (dash lines) and I-1 (solid lines) at temperatures from 78 K up to 200 K. The device sizes for I-2 and I-1 are 1×1 mm^2 and 0.4×0.4 mm^2, respectively [162].

A FTIR spectrometer and a blackbody source with a 0.76 cm aperture were used for optical response measurements. The response spectra at temperatures ranging from 78 K to 250 K are shown in Figure 5.13. In some situations, a finite reverse bias was required to fully collect the photogenerated carriers. For example, the zero bias responsivity of I-1 at 8 μm was 0.20 A/W at 78 K. It increased with bias and

eventually saturated at 0.28 A/W for a bias of 300 mV. The table inset to Figure 5.13 lists the bias values at which the responsivity saturated at various temperatures. This bias dependence was not expected from the operation principle of ICPDs [46]. Undesirable barriers may be formed between unipolar barriers and the absorber due to unconsidered factors in the design and possible variations during the growth, which blocked the collection of photogenerated carriers. Detectors from the I-2 wafer did not show any bias dependence up to 167 K. For temperatures above 167 K, the responsivity started to increase with bias and saturated at a certain reverse bias. For example, at 167 K, the responsivity of I-2 at 8 μm increased from 0.31 A/W to 0.32 A/W when the bias was increased from 0 to 50 mV and did not increase with further bias. Whereas I-1 had a bias dependence over the whole temperature range. While the stronger bias dependence for I-1 is not fully understood, we speculate that that some unintentional differences, related to the design and growth, might have been introduced in the regions connecting absorber and unipolar barriers. Further investigation is needed to address this issue.

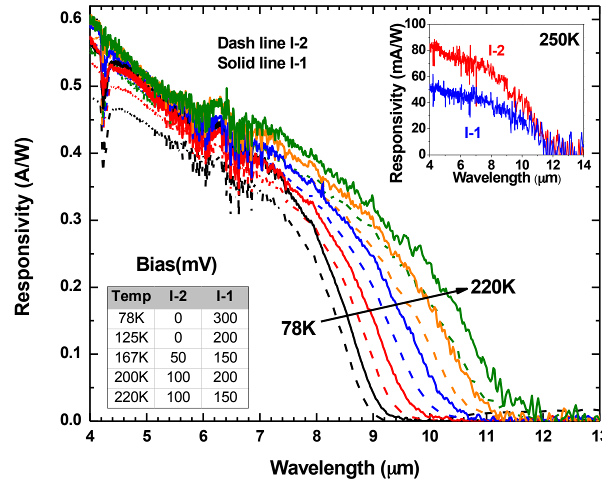

Figure 5.13: Responsivity spectra for detectors made from wafers I-2 (dash line) and I-1 (solid line) at temperatures from 78 K to 220 K. The device sizes for I-2 and I-1 are 0.4×0.4 mm^2. The inset table shows the reverse bias applied to the device during the measurement. The inset figure shows the spectra of I-2 (red line) and I-1 (blue line) at 250 K [162].

As shown in Figure 5.13, the 100% cutoff wavelength of I-2 (I-1) was 9.2 μm (9.5 μm) at 78 K, which corresponds to a bandgap of 135 meV (130 meV). The bandgap of I-2 is slightly wider, consistent with XRD results showing a slightly shorter SL period. Consequently at the same wavelength, the responsivity of I-1 is slightly higher because more photons could be absorbed to generate carriers. This differs from the results of Ref. [79], where the photoresponse was significantly weaker when the InSb thickness was increased from 0.8 to 1.1 ML. At temperatures higher than 220 K, the response spectra were collected without applying a bias (inset to Figure 5.13) due to instrument limitations and the high dark current. From the spectra, both I-2 and I-1 had a cutoff wavelength of 12 μm at 250 K. The results demonstrate the capability of ICPDs to operate at high temperatures in the long-wavelength infrared region.

Figure 5.14 shows the normalized detectivities of I-2 and I-1 from 78 K to 220 K, which were calculated using

$$D^* = \frac{R_\lambda}{\sqrt{\frac{4k_BT}{RA} + \frac{2qJ_d}{N_c}}} \quad , \qquad (5.1)$$

where R_λ is the responsivity, k_B is the Boltzmann constant, T is the absolute temperature, q is the electron charge, J_d is the dark current density, R is the device resistance, N_c is the number of cascade stages, and A is the device mesa area. The equation includes a shot-noise term ($2qJ_d/N_c$) to account for the effect of dark current on the D^* at a finite reverse bias, which reduces D^* at a high reverse bias. As an example, the maximum D^* of I-1 was found at zero bias at 78K, while the maximum photo-responsivity was measured at 300 mV. Therefore the D^* was less bias dependent than the device photoresponse. From the signal-to-noise perspective, I-2 and I-1 were comparable. The highest D^* for I-2 and I-1 at 8 μm under zero-bias operation was 3.7×10^{10} Jones and 3.8×10^{10} Jones, respectively. At 200 K, they were 6.9×10^{8} Jones and 7.0×10^{8} Jones, respectively.

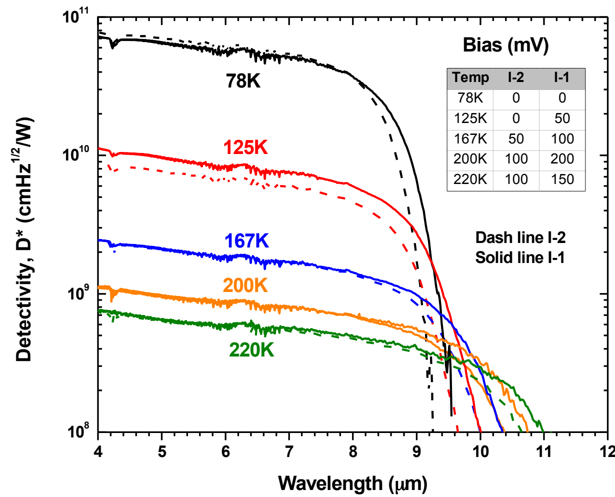

Figure 5.14: Detectivity D^* for detectors made from I-2 (dash lines) and I-1 (solid lines) at temperatures from 78 K up to 220 K. The device sizes for I-2 and I-1 are 0.4×0.4 mm^2. The inset table shows the reverse bias applied to the device during the measurement [162].

Based on the above comparisons, we conclude that devices made from I-2 and I-1 had similar performance and did not exhibit any effects attributable to different interface structures. Although devices from I-1 showed a slightly lower dark current density than devices from I-2 at 78 K, devices from both wafers had a similar detectivity (3.7×10^{10} Jones for 78 K at 8 μm) and were able to operate up to 250 K.

From the above structural, optical and electrical results, we learned that the I-2 structure (InSb layer at two interfaces) is not better than the I-1 structure (InSb layer at one interface), in contrast to our expectations. There are several possible explanations. First, our growth conditions could have suppressed the roughening mechanism and thus the I-1 structure did not show the degraded material qualities predicted from earlier work [79, 159, 160]. However, even if I-1 did not degrade, I-2 should still have a better device performance due to the two InSb-like interfaces structure as predicted

by reference [161]. Our result implies that an InSb-like interface naturally forms at the InAs-on-GaSb interface under the group-V rich conditions used for I-1. In this case, I-1 also has two InSb-like interfaces. Therefore, the device performance would be the same for I-2 and I-1. An alternative explanation is that the device performance was dominated by factors other than the interface quality (and type). Similar conclusions were reached by Svensson *et al.* [74] after examining the minority carrier lifetime with various interface densities. They concluded that the carrier recombination process was not dominated by the interface, but by non-interface-related mechanisms such as the native defects (*e.g.* vacancies, anti-sites, and interstitials) within the GaSb and/or InAs layers of the SL. Hence, the relatively short minority carrier lifetime was caused primarily by bulk defect centers and dictated the device performance of InAs/GaSb SL detectors. Similarly, the device performance of ICPDs made from I-2 and I-1 could be dominated by bulk defect centers even though surface defect densities are not high; while interface factors only play a secondary role. If this were the case, then one would not be able to observe any substantial difference in device performance for I-2 and I-1. Further investigation is needed to obtain a more definitive answer.

Nevertheless, these device performance results demonstrate the capability of ICPDs to operate at high temperatures in the long-wavelength infrared region. Our results imply that the interface quality was reasonably controlled for the interface arrangements of both I-2 and I-1, and resulted in photodetectors with good performance. Inclusion of 1.2 ML of InSb at half the interfaces did not degrade the performance of an ICPD, in contrast to the inferences from previous studies. Inclusion

of up to 1.2 ML of InSb at all the interfaces could be a viable strategy for devices with even longer wavelengths.

Chapter 6 Conclusion and Future Work

This dissertation focused on the MBE growth of interband cascade structures for lasers, photovoltaic devices, and photodetectors using III-V materials. These devices utilize a multiple-stage architecture to achieve effective conversion between electricity and infrared light. Operation principles of these devices were introduced in Chapter 1. The devices are composed of InAs, GaSb, AlSb, and their alloys, which share a similar lattice constant around 6.1 Å and thus can be grown on InAs or GaSb substrates under strain balanced condition. High material quality is a prerequisite for good device performances.

Chapter 2 introduces the MBE growth with details of how to control the growth conditions. The reproducibility in the growth rate is obtained by using beam equivalent pressures as references, since a relationship between beam equivalent pressure and growth rate can be established using RHEED oscillations. The evolving statuses of the MBE system are less controllable factors in the growth, as some of them imply intrinsic facility problems. For example, the flux becomes less stable at the end of the campaign due to the rapid change of the surface area of the source material. Moreover, cell issues, such as shutter transient, thermal expansion of the cell thermocouple, and filament short circuit, could lead to low stability, reproducibility, or even failed growths. Therefore, precise MBE growth relies on an excellent facility and deliberate maintenance.

Two MBE systems, an Intevac Gen II and a Veeco GENxplor, are used in the group for IC structure growths. The GENxplor only started to operate in 2015, growth conditions in the GENxplor are not yet optimized. With a fair comparison in the

growth qualities, it will be interesting to know how a 20-year-newer machine could facilitate a better growth. An improved shutter transient issue was observed using sumo crucibles with a dual-filament cell in the GENxplor. However, the long-term stability of the cells seems to be a problem due to the intrinsic designs and has hampered the growth of thick structures. Further improvement of the machine is expected to bring out the advantages of the GENxplor.

An antimony cell with a valved cracker was installed to the GENxplor, and the flexibility of changing the Sb overpressure can be particularly useful for IC structures. For example, a fine tuning of the V/III ratio in GaInSb and AlSb layers can be carried out in cascade stages of the ICL. The Sb overpressure is a compromised value between various layers and was kept the same in the structure in the GEN II to avoid changing the Sb cell temperature, since there is no valve available. Also, with extra ports available in the growth chamber, a quadrupole mass spectrometer can be used as an *in situ* sensor to monitor the incorporation of the group-V species [167]. This will be useful in the growth of mixed group-V alloys, and thus could be beneficial to grow type-I ICLs, where GaInAsSb is used in the active region [168].

Chapter 3 discussed the material characterization methods including XRD, AFM, and SEM. The SL period and lattice mismatch were deduced from the XRD measurements to check the growth quality and reproducibility. Experimental errors and limitations were discussed, especially concerning the determination of the zero order peak in scans of ICL structures with criteria from Matthews-Blakeslee critical thickness calculations. Further studies of strain and relaxation can be explored by using an asymmetric scan and reciprocal space map. Furthermore, AFM and SEM

were used to evaluate surface morphology. Surface roughness can be observed by SEM using a backscattered electron detector under particular imaging conditions. SEM played an important role in device failure analysis and has wider applications with the use of a focused ion beam to prepare TEM specimens and carry out special pattern fabrications.

Chapter 4 focused on the InAs-based ICL structures starting with the InAs layers. Si and Te doping of InAs layers were investigated, and further studies are needed to address the problem of rough surface morphology at high Te doping. Optimal conditions for growth of homoepitaxial InAs layers at a growth rate of 0.66 ML/s were investigated with DIC microscopy, SEM, and AFM. Better growth quality was attained by using a slower InAs growth rate of 0.22 ML/s instead of 0.66 ML/s at a substrate temperature of ~400°C. The growth conditions for a lower growth rate were not investigated systematically, and thus further improvement is possible. However the three-times-longer growth time requires the growth conditions be stable over a much longer time, especially for thick structures. Approaches to maintaining good material quality at a high growth rate are worth investigating. The geometry of oval hillock defects in InAs layers was characterized by coordinated measurements (AFM, SEM, FIB, and TEM). The features appearing beneath the pit of large oval hillock defects suggests that they are generated by a contaminant, residual oxide, or excess indium that blocks initial homoepitaxial growth at the substrate interface. To eliminate the defects, further investigations are needed of various aspects, *e.g*, InAs substrates with low etch pit density, chemical etching process of the wafer that helps oxide desorption, and spitting from indium crucibles.

The growth conditions for a typical ICL structure were introduced. Lasers fabricated from these structures achieved state-of-the-art performance including the longest emission wavelength (11 μm) among interband lasers based on III–V materials. However, the high threshold current density in the long wavelength ICLs suggests a correlation with a defect-related carrier leakage channels and non-uniformity. Further investigation of the growth conditions for the cascade stages should be carried out, especially for long wavelength structures, where larger a mismatch exists in the GaInSb layer.

An improved waveguide configuration was proposed with the use of an InAs/AlSb SL in the InAs-based ICLs [20]. Preliminary growths led to the first continuous wave operation of InAs-based IC lasers at room temperature. The threshold current density of 247 A/cm^2 was the lowest ever obtained for semiconductor mid-infrared lasers near 4.6 μm at room temperature. Better device performance at even longer wavelength is expected with an optimized growth condition. Strain balance in the InAs/AlSb SL should be less challenging on InAs substrates than on GaSb substrates, since the compressive strain induced by AlSb can be balanced by predominantly formed AlAs-rich interfaces [169]. With multiple layers/SLs integrated into one structure, using different substrate temperatures that are optimized for them during the growth is expected to improve the material quality [12, 82, 170].

Chapter 5 presented the growth of ICPV and ICPD structures, which consist of multiple discrete InAs/GaSb SL absorbers sandwiched between electron and hole barriers. Strain-balanced InAs/GaSb SL structures were achieved by adjusting the

group-V overpressure during MBE growth. A strain-balanced condition is beneficial for the growth of even thicker absorbers, which may be required to achieve high quantum efficiencies for LWIR detectors. Typical growth conditions were presented for ICPV and ICPD structures. Two- and three-stage ICPV devices operated at room temperature with substantial open-circuit voltages at a cutoff wavelength of 5.3 μm, the longest ever reported for room-temperature PV devices.

To improve the PDs designed for the long-wavelength infrared region, two different interfaces arrangements of InAs/GaSb SLs were studied, one with a ~1.2 ML-thick InSb layer inserted intentionally only at the GaSb-on-InAs interfaces and another with a ~0.6 ML-thick InSb layer inserted at both InAs-on-GaSb and GaSb-on-InAs interfaces. The material quality and the device performances were not substantially different. Both had a detectivity of 3.7×10^{10} Jones for 78 K at 8 μm and operated up to 250 K. This suggests that the arrangement of dividing a thick continuous InSb layer at the GaSb-on-InAs interface into thinner InSb layers at both interfaces can be used to achieve strain balance in SL detectors at even longer wavelengths. On the other hand, it indicates that device performance was dominated by factors other than the interface quality (and type). Studies have suggests that the carrier recombination process was not dominated by the interface, but by non-interface-related mechanisms such as the native defects (*e.g.* vacancies, anti-sites, and interstitials) within the GaSb and/or InAs layers of the SL [74]. Some studies have found that InAs/InAsSb SLs have significantly longer minority carrier lifetimes than InAs/GaInSb SLs, and thus suspect the short lifetime may relate to the presence of Ga [171-173]. Therefore, fundamental material studies of InAs/GaSb are required for

overall device performance improvements. With an improved material quality as well as fabrication, ICPDs should be able to operate at higher temperatures at even longer wavelengths and demonstrate advantages of the discrete absorber architecture.

References

1. B.R. Bennett, R. Magno, J.B. Boos, W. Kruppa, *et al.*, *Antimonide-based compound semiconductors for electronic devices: A review.* Solid-State Electronics, **49**: p. 1875 (2005).
2. C.R. Bolognesi, J.E. Bryce, and D.H. Chow, *InAs channel heterostructure-field effect transistors with InAs/AlSb short-period superlattice barriers.* Applied Physics Letters, **69**(23): p. 3531 (1996).
3. D.H. Chow, H.L. Dunlap, W. Williamson, S. Enquist, *et al.*, *InAs/AlSb/GaSb resonant interband tunneling diodes and Au-on-InAs/AlSb-superlattice Schottky diodes for logic circuits.* IEEE Electron Device Letters, **17**(2): p. 69 (1996).
4. L.F. Luo, R. Beresford, and W.I. Wang, *Resonant tunneling in AlSb/InAs/AlSb double-barrier heterostructures.* Applied Physics Letters, **53**(23): p. 2320 (1988).
5. I. Vurgaftman, J.R. Meyer, F.H. Julien, and L.R. Ram-Mohan, *Design and simulation of low-threshold antimonide intersubband lasers.* Applied Physics Letters, **73**(6): p. 711 (1998).
6. R.Q. Yang, *Infrared laser based on intersubband transitions in quantum wells.* Superlattices and Microstructures, **17**(1): p. 77 (1995).
7. D.L. Smith and C. Mailhiot, *Proposal for strained type II superlattice infrared detectors.* Journal of Applied Physics, **62**(6): p. 2545 (1987).
8. C. Charpentier, S. Fält, C. Reichl, F. Nichele, *et al.*, *Suppression of bulk conductivity in InAs/GaSb broken gap composite quantum wells.* Applied Physics Letters, **103**(11): p. 112102 (2013).
9. C. Liu, T.L. Hughes, X.-L. Qi, K. Wang, *et al.*, *Quantum spin hall effect in inverted type-II semiconductors.* Physical Review Letters, **100**(23): p. 236601 (2008).
10. R.Q. Yang , Infrared laser based on intersubband transitions in quantum wells, at 7th Inter. Conf. on Superlattices, Microstructures and Microdevices, Banff, Canada, August, 1994;
11. C.-H. Lin, R.Q. Yang, D. Zhang, S.J. Murry, *et al.*, *Type-II interband quantum cascade laser at 3.8 μm.* Electronics Letters, **33**(7): p. 598 (1997).
12. I. Vurgaftman, R. Weih, M. Kamp, J.R. Meyer, *et al.*, *Interband cascade lasers.* Journal of Physics D: Applied Physics, **48**(12): p. 123001 (2015).
13. J.R. Meyer, I. Vurgaftman, R.Q. Yang, and L.R. Ram-Mohan, *Type-II and type-I interband cascade lasers.* Electronics Letters, **32**(1): p. 45 (1996).
14. B.H. Yang, D. Zhang, R.Q. Yang, C.H. Lin, *et al.*, *Mid-infrared interband cascade lasers with quantum efficiencies >200%.* Applied Physics Letters, **72**(18): p. 2220 (1998).

15. R.Q. Yang, J.L. Bradshaw, J.D. Bruno, J.T. Pham*, et al.*, *Mid-infrared type-II interband cascade lasers.* IEEE Journal of Quantum Electronics, **38**(6): p. 559 (2002).

16. K. Mansour, Y. Qiu, C.J. Hill, A. Soibel*, et al.*, *Mid-infrared interband cascade lasers at thermoelectric cooler temperatures.* Electronics Letters, **42**(18): p. 1034 (2006).

17. R.Q. Yang, L. Li, L. Zhao, Y. Jiang*, et al. Recent progress in development of InAs-based interband cascade lasers*. in *SPIE*. San Francisco, CA86400Q (2013).

18. S. Höfling, R. Weih, M. Dallner, J. Scheuermann*, et al. Mid-infrared (~2.8 µm to ~7.1 µm) interband cascade lasers*. in *Proc. of SPIE*. Biosensing and Nanomedicine VIII, p. 95500F (2015).

19. C.R. Webster, P.R. Mahaffy, S.K. Atreya, G.J. Flesch*, et al.*, *Mars methane detection and variability at Gale crater.* Science, **347**(6220): p. 415 (2015).

20. L. Li, Y. Jiang, H. Ye, R.Q. Yang*, et al.*, *Low-threshold InAs-based interband cascade lasers operating at high temperatures.* Applied Physics Letters, **106**(25): p. 251102 (2015).

21. I. Vurgaftman, W.W. Bewley, C.L. Canedy, C.S. Kim*, et al.*, *Rebalancing of internally generated carriers for mid-infrared interband cascade lasers with very low power consumption.* Nature Communications, **2**: p. 585 (2011).

22. C. Sirtori, J. Faist, F. Capasso, D.L. Sivco*, et al.*, *Quantum cascade laser with plasmon-enhanced waveguide operating at 8.4 µm wavelength.* Applied Physics Letters, **66**(24): p. 3242 (1995).

23. C. Sirtori, P. Kruck, S. Barbieri, H. Page*, et al.*, *Low-loss Al-free waveguides for unipolar semiconductor lasers.* Applied Physics Letters, **75**(25): p. 3911 (1999).

24. Z. Tian, R.Q. Yang, T.D. Mishima, M.B. Santos*, et al.*, *Inas-based interband cascade lasers near 6 µm.* Electronics Letters, **45**(1): p. 48 (2009).

25. Z. Tian, C. Chen, R.Q. Yang, T.D. Mishima*, et al. InAs-based plasmon-waveguide interband cascade lasers*. in *Proc. SPIE*. San Francisco, California, USA: SPIE, p. 76161B (2010).

26. L. Li, H. Ye, Y. Jiang, R.Q. Yang*, et al.*, *MBE-grown long-wavelength interband cascade lasers on InAs substrates.* Journal of Crystal Growth, **425**: p. 369 (2015).

27. Y. Wei, A. Gin, M. Razeghi, and G.J. Brown, *Type II InAs/GaSb superlattice photovoltaic detectors with cutoff wavelength approaching 32 µm.* Applied Physics Letters, **81**(19): p. 3675 (2002).

28. Y. Wei, J. Bae, A. Gin, A. Hood*, et al.*, *High quality type II InAs/GaSb superlattices with cutoff wavelength ~3.7 µm using interface engineering.* Journal of Applied Physics, **94**(7): p. 4720 (2003).

29. M. Razeghi and B.-M. Nguyen, *Band gap tunability of Type II Antimonide-based superlattices.* Physics Procedia, **3**(2): p. 1207 (2010).

30. F. Fuchs, U. Weimer, W. Pletschen, J. Schmitz*, et al.*, *High performance InAs/$Ga_{1-x}In_xSb$ superlattice infrared photodiodes.* Applied Physics Letters, **71**(22): p. 3251 (1997).

31. W.E. Tennant, *"Rule 07" Revisited: Still a Good Heuristic Predictor of p/n HgCdTe Photodiode Performance?* Journal of Electronic Materials, **39**(7): p. 1030 (2010).

32. C.H. Grein, P.M. Young, and H. Ehrenreich, *Minority carrier lifetimes in ideal InGaSb/InAs superlattices.* Applied Physics Letters, **61**(24): p. 2905 (1992).

33. J.V. Li, R.Q. Yang, C.J. Hill, and S.L. Chuang, *Interband cascade detectors with room temperature photovoltaic operation.* Applied Physics Letters, **86**(10): p. 101102 (2005).

34. I. Vurgaftman, E.H. Aifer, C.L. Canedy, J.G. Tischler*, et al.*, *Graded band gap for dark-current suppression in long-wave infrared W-structured type-II superlattice photodiodes.* Applied Physics Letters, **89**(12) (2006).

35. S. Maimon and G.W. Wicks, *nBn detector, an infrared detector with reduced dark current and higher operating temperature.* Applied Physics Letters, **89**(15): p. 151109 (2006).

36. J.B. Rodriguez, E. Plis, G. Bishop, Y.D. Sharma*, et al.*, *nBn structure based on InAs/GaSb type-II strained layer superlattices.* Applied Physics Letters, **91**(4): p. 043514 (2007).

37. B.-M. Nguyen, D. Hoffman, P.-Y. Delaunay, and M. Razeghi, *Dark current suppression in type II InAs/GaSb superlattice long wavelength infrared photodiodes with M-structure barrier.* Applied Physics Letters, **91**(16) (2007).

38. D.Z.-Y. Ting, C.J. Hill, A. Soibel, S.A. Keo*, et al.*, *A high-performance long wavelength superlattice complementary barrier infrared detector.* Applied Physics Letters, **95**(2): p. 023508 (2009).

39. R.Q. Yang, Z. Tian, Z. Cai, J.F. Klem*, et al.*, *Interband-cascade infrared photodetectors with superlattice absorbers.* Journal of Applied Physics, **107**(5): p. 054514 (2010).

40. Z. Tian, R.T. Hinkey, R.Q. Yang, D. Lubyshev*, et al.*, *Interband cascade infrared photodetectors with enhanced electron barriers and p-type superlattice absorbers.* Journal of Applied Physics, **111**(2): p. 024510 (2012).

41. R.T. Hinkey and R.Q. Yang, *Theory of multiple-stage interband photovoltaic devices and ultimate performance limit comparison of multiple-stage and single-stage interband infrared detectors.* Journal of Applied Physics, **114**(10): p. 104506 (2013).

42. H. Lotfi, L. Li, L. Lei, H. Ye*, et al.*, *High-frequency operation of a mid-infrared interband cascade system at room temperature.* Applied Physics Letters, **108**: p. 201101 (2016).

43. R.T. Hinkey, *Multiple-stage interband cascade photovoltaic devices using 6.1 Å semiconductor materials*, 2013, University of Oklahoma.

44. R.T. Hinkey, H. Lotfi, L. Li, H. Ye*, et al. Interband cascade infrared photodetectors with InAs/GaSb superlattice absorbers*. in *Proc. SPIE*. 886805 (2013).

45. H. Lotfi, L. Lei, L. Li, R.Q. Yang*, et al.*, *High-temperature operation of interband cascade infrared photodetectors with cutoff wavelengths near 8 μm.* Optical Engineering, **54**(6): p. 063103 (2015).

46. H. Lotfi, L. Li, H. Ye, R.T. Hinkey*, et al.*, *Interband cascade infrared photodetectors with long and very-long cutoff wavelengths.* Infrared Physics & Technology, **70**: p. 162 (2015).

47. H. Lotfi, L. Li, L. Lei, Y. Jiang*, et al.*, *Short-wavelength interband cascade infrared photodetectors operating above room temperature.* Journal of Applied Physics, **119**(2): p. 023105 (2016).

48. R.Q. Yang, Z. Tian, J.F. Klem, T.D. Mishima*, et al.*, *Interband cascade photovoltaic devices.* Applied Physics Letters, **96**(6): p. 063504 (2010).

49. D. Wilt, D. Chubb, D. Wolford, P. Magari*, et al.*, *Thermophotovoltaics for space power applications.* AIP Conference Proceedings, **890**(1): p. 335 (2007).

50. V.L. Teofilo, P. Choong, J. Chang, Y.L. Tseng*, et al.*, *Thermophotovoltaic energy conversion for space.* Journal of Physical Chemistry C, **112**(21): p. 7841 (2008).

51. A. Datas and C. Algora, *Global optimization of solar thermophotovoltaic systems.* Progress in Photovoltaics: Research and Applications, **21**(5): p. 1040 (2013).

52. W.R. Chan, P. Bermel, R.C.N. Pilawa-Podgurski, C.H. Marton*, et al.*, *Toward high-energy-density, high-efficiency, and moderate-temperature chip-scale thermophotovoltaics.* Proc. of the National Academy of Sciences, **110**(14): p. 5309 (2013).

53. T.J. Coutts and J.S. Ward, *Thermophotovoltaic and photovoltaic conversion at high-flux densities.* IEEE Transactions on Electron Devices, **46**(10): p. 2145 (1999).

54. M.G. Mauk and V.M. Andreev, *GaSb-related materials for TPV cells.* Semiconductor Science and Technology, **18**(5): p. S191 (2003).

55. M. Zenker, A. Heinzel, G. Stollwerck, J. Ferber*, et al.*, *Efficiency and power density potential of combustion-driven thermophotovoltaic systems using GaSb photovoltaic cells.* IEEE Transactions on Electron Devices, **48**(2): p. 367 (2001).

56. N. Su, P. Fay, S. Sinharoy, D. Forbes*, et al.*, *Characterization and modeling of InGaAs/InAsP thermophotovoltaic converters under high illumination intensities.* Journal of Applied Physics, **101**(6): p. 064511 (2007).

57. H. Lotfi, R.T. Hinkey, L. Li, R.Q. Yang*, et al. Multi-stage photovoltaic devices with a cutoff wavelength of ~3 μm*. in *Photovoltaic Specialist Conference (PVSC), IEEE 40th*. 0220 (2014).

58. H. Ye, H. Lotfi, L. Li, R. Hinkey*, et al.*, *Multistage interband cascade photovoltaic devices with a bandgap of 0.23 eV operating above room temperature.* Chinese Science Bulletin, **59**(10): p. 950 (2014).

59. R.T. Hinkey, Z.-B. Tian, S.M.S.S. Rassel, R.Q. Yang*, et al.*, *Interband cascade photovoltaic devices for conversion of mid-IR radiation.* IEEE Journal of Photovoltaics, **3**(2): p. 745 (2013).

60. H. Lotfi, R.T. Hinkey, L. Li, R.Q. Yang*, et al.*, *Narrow-bandgap photovoltaic devices operating at room temperature and above with high open-circuit voltage.* Applied Physics Letters, **102**(21): p. 211103 (2013).

61. L.L. Chang and L. Esaki, *Electronic properties of InAs-GaSb superlattices.* Surface Science, **98**(1): p. 70 (1980).

62. E. Canova, A.I. Goldman, S.C. Woronick, Y.H. Kao*, et al.*, *Interatomic distance and local order in InAs-AlSb semiconductor superlattices.* Physical Review B, **31**(12): p. 8308 (1985).

63. C.A. Chang, L.L. Chang, E.E. Mendez, M.S. Christie*, et al.*, *Electron densities in InAs–AlSb quantum wells.* Journal of Vacuum Science & Technology B, **2**(2): p. 214 (1984).

64. E.E. Mendez, C.A. Chang, H. Takaoka, L.L. Chang*, et al.*, *Optical properties of GaSb–AlSb superlattices.* Journal of Vacuum Science & Technology B, **1**(2): p. 152 (1983).

65. H. Kroemer, *The 6.1 Å family (InAs, GaSb, AlSb) and its heterostructures: a selective review.* Physica E, **20**: p. 196 (2004).

66. M.E. Twigg, B.R. Bennett, B.V. Shanabrook, J.R. Waterman*, et al.*, *Interfacial roughness in InAs/GaSb superlattices.* Applied Physics Letters, **64**(25): p. 3476 (1994).

67. R.M. Feenstra, D.A. Collins, D.Z.Y. Ting, M.W. Wang*, et al.*, *Interface roughness and asymmetry in InAs/GaSb superlattices studied by scanning tunneling microscopy.* Physical Review Letters, **72**(17): p. 2749 (1994).

68. Y. Ashuach, Y. Kauffmann, C. Saguy, S. Grossman*, et al.*, *Quantification of atomic intermixing in short-period InAs/GaSb superlattices for infrared photodetectors.* Journal of Applied Physics, **113**(18): p. 184305 (2013).

69. J. Steinshnider, M. Weimer, R. Kaspi, and G.W. Turner, *Visualizing interfacial structure at non-common-atom heterojunctions with cross-sectional scanning tunneling microscopy.* Physical Review Letters, **85**(14): p. 2953 (2000).

70. J.R. Waterman, B.V. Shanabrook, R.J. Wagner, M.J. Yang*, et al.*, *The effect of interface bond type on the structural and optical properties of GaSb/InAs superlattices.* Semiconductor Science and Technology, **8**(1S): p. S106 (1993).

71. G.R. Booker, P.C. Klipstein, M. Lakrimi, S. Lyapin, *et al.*, *Growth of InAsGaSb strained layer superlattices. II.* Journal of Crystal Growth, **146**(1–4): p. 495 (1995).

72. G. Tuttle, H. Kroemer, and J.H. English, *Effects of interface layer sequencing on the transport properties of InAs/AlSb quantum wells: Evidence for antisite donors at the InAs/AlSb interface.* Journal of Applied Physics, **67**(6): p. 3032 (1990).

73. J. Spitzer, A. Höpner, M. Kuball, M. Cardona, *et al.*, *Influence of the interface composition of InAs/AlSb superlattices on their optical and structural properties.* Journal of Applied Physics, **77**(2): p. 811 (1995).

74. S.P. Svensson, D. Donetsky, D. Wang, H. Hier, *et al.*, *Growth of type II strained layer superlattice, bulk InAs and GaSb materials for minority lifetime characterization.* Journal of Crystal Growth, **334**(1): p. 103 (2011).

75. L.M. Murray, K.S. Lokovic, B.V. Olson, A. Yildirim, *et al.*, *Effects of growth rate variations on carrier lifetime and interface structure in InAs/GaSb superlattices.* Journal of Crystal Growth, **386**(0): p. 194 (2014).

76. J.B. Rodriguez, P. Christol, L. Cerutti, F. Chevrier, *et al.*, *MBE growth and characterization of type-II InAs/GaSb superlattices for mid-infrared detection.* Journal of Crystal Growth, **274**(1–2): p. 6 (2005).

77. R. Kaspi, J. Steinshnider, M. Weimer, C. Moeller, *et al.*, *As-soak control of the InAs-on-GaSb interface.* Journal of Crystal Growth, **225**(2–4): p. 544 (2001).

78. A. Bauer, M. Dallner, A. Herrmann, T. Lehnhardt, *et al.*, *Atomic scale interface engineering for strain compensated epitaxially grown InAs/AlSb superlattices.* Nanotechnology, **21**(45): p. 455603 (2010).

79. H.J. Haugan, L. Grazulis, G.J. Brown, K. Mahalingam, *et al.*, *Exploring optimum growth for high quality InAs/GaSb type-II superlattices.* Journal of Crystal Growth, **261**(4): p. 471 (2004).

80. M.J. Yang, W.J. Moore, B.R. Bennett, B.V. Shanabrook, *et al.*, *Optimum growth parameters for type-II infrared lasers.* Journal of Applied Physics, **86**(4): p. 1796 (1999).

81. C.L. Canedy, W.W. Bewley, C.S. Kim, M. Kim, *et al.*, *Dependence of type II "W" mid-infrared photoluminescence and lasing properties on growth conditions.* Journal of Applied Physics, **94**(3): p. 1347 (2003).

82. C.L. Canedy, J. Abell, W.W. Bewley, E.H. Aifer, *et al.*, *Molecular beam epitaxial growth effects on type-II antimonide lasers and photodiodes.* Journal of Vacuum Science & Technology B, **28**(3): p. C3G8 (2010).

83. I.E. Trofimov, C.L. Canedy, C.S. Kim, M. Kim, *et al.*, *Interband cascade lasers with long lifetimes.* Applied Optics, **54**(32): p. 9441 (2015).

84. S.E. Aleksandrov, G.A. Gavrilov, A.A. Kapralov, G.Y. Sotnikova, *et al.*, *Pyrometer unit for GaAs substrate temperature control in an MBE system.* Technical Physics, **49**(1): p. 123 (2004).

85. W. Braun, V.M. Kaganer, B. Jenichen, D.K. Satapathy, *et al.*, *Surface kinetics of GaAs(001), InAs(001) and GaSb(001) during MBE growth studied by in situ surface X-ray diffraction.* Journal of Crystal Growth, **278**(1–4): p. 449 (2005).

86. *Eurotherm Model 2416 PID Controller Installation and Operation Handbook.* (2006).

87. M.L. O'steen, *personal communication*, Dec. 2014.

88. *Veeco Aluminum SUMO Effusoin Cell Dual Filament User Guide.*

89. P. R.Larson, *personal communication*, Feb. 2016.

90. S. Subbanna, J. Gaines, G. Tuttle, H. Kroemer, *et al.*, *Reflection high-energy electron diffraction oscillations during molecular-beam epitaxy growth of gallium antimonide, aluminum antimonide, and indium arsenide.* Journal of Vacuum Science & Technology B, **7**(2): p. 289 (1989).

91. B.R. Bennett, R. Magno, and N. Papanicolaou, *Controlled n-type doping of antimonides and arsenides using GaTe.* Journal of Crystal Growth, **251**(1–4): p. 532 (2003).

92. H. Ye, L. Li, R.T. Hinkey, R.Q. Yang, *et al.*, *MBE growth optimization of InAs (001) homoepitaxy.* Journal of Vacuum Science & Technology B, **31**(3): p. 03C135 (2013).

93. Y.G. Chai and R. Chow, *Source and elimination of oval defects on GaAs films grown by molecular beam epitaxy.* Applied Physics Letters, **38**(10): p. 796 (1981).

94. H. Kawada, S. Shirayone, and K. Takahashi, *Reduction of surface defects in GaAs layers grown by MBE.* Journal of Crystal Growth, **128**(1–4): p. 550 (1993).

95. N.J. Kadhim and D. Mukherjee, *Growth model of oval defect structures in MBE GaAs layers.* Journal of Materials Science Letters, **18**(3): p. 229 (1999).

96. A. Szerling, K. Kosiel, A. Wojcik-Jedlinska, M. Pluska, *et al.*, *Properties and origin of oval defects in epitaxial structures grown by molecular beam epitaxy.* Optica Applicata, **35**(3): p. 537 (2005).

97. K.J. Goldammer, *Molecular beam epitaxy and characterization of InAs/$Al_xIn_{1-x}Sb$ heterostructures*, 1998, University of Oklahoma: Norman.

98. *Sottware for the Materials Research Diffractometer User Guide*. First Edition ed1993: Philips Electronics N.V.

99. D.K. Bowen and B.K. Tanner, *High Resolution X-ray Diffractometry and Topography*. 1998: Taylor & Francis Inc.

100. T.A. Garcia, J. De Jesus, A.P. Ravikumar, C.F. Gmachl, *et al.*, *II–VI quantum cascade emitters in the 6–8 μm range.* physica status solidi (b): p. 1 (2016).

101. J.E. Ayers, *Heteroepitaxy of Semiconductors Theory, Growth, and Characterization*. 2007 Hoboken : Taylor and Francis

102. J.W. Matthews, *Defects associated with the accommodation of misfit between crystals.* Journal of Vacuum Science and Technology, **12**(1): p. 126 (1975).

103. J.W. Matthews and A.E. Blakeslee, *Defects in epitaxial multilayers: I. Misfit dislocations.* Journal of Crystal Growth, **27**: p. 118 (1974).

104. C.J. Hill and R.Q. Yang, *MBE growth optimization of Sb-based interband cascade lasers.* Journal of Crystal Growth, **278**(1–4): p. 167 (2005).

105. R.S. Dhar, L. Li, H. Ye, S.G. Razavipour*, et al.*, *Nanoscopically resolved dynamic charge-carrier distribution in operating interband cascade lasers.* Laser & Photonics Reviews, **9**(2): p. 224 (2015).

106. R. Fuierer, *MFP-3D Procedural Operation 'Manualette'*. 10 ed 2009.

107. *MFP-3D™ Atomic Force Microscope Proprietary Specifications*.

108. P. Cubillas and M.W. Anderson, *Atomic Force Microscopy*, in *Multi Length-Scale Characterisation*, D.W. Bruce, Editor 2014, John Wiley & Sons, Ltd.

109. J.C. Keay, L. Li, D.B. Brunski, E.S. Sanchez*, et al.*, *Suppression of slip-line defect formation in GaSb substrates during thermal desorption of oxide layers*, in *Poster session presented at: 28th North American Molecular Beam Epitaxy* 2011: La Jolla, CA.

110. J. Goldstein, D.E. Newbury, D.C. Joy, C.E. Lyman*, et al.*, *Scanning Electron Microscopy and X-ray Microanalysis*. 2003: Kluwer Academic/Plenum Publishers.

111. http://www.fei.com/introduction-to-electron-microscopy/, *An introduction to electron microscopy*.

112. D. Joy, *http://www.guycox.com/emtutor/monte.htm*, 2004.

113. J.R. Pedrazzani, S. Maimon, and G.W. Wicks, *Use of nBn structures to suppress surface leakage currents in unpassivated InAs infrared photodetectors.* Electronics Letters, **44**(25): p. 1487 (2008).

114. C.H. Kuan, R.M. Lin, S.F. Tang, and T.P. Sun, *Analysis of the dark current in the bulk of InAs diode detectors.* Journal of Applied Physics, **80**(9): p. 5454 (1996).

115. A. Krier, M. Yin, A.R.J. Marshall, and S.E. Krier, *Low bandgap InAs-based thermophotovoltaic cells for heat-electricity conversion.* Journal of Electronic Materials, **45**(6): p. 2826 (2016).

116. K. Nomoto, K. Taira, T. Suzuki, I. Hase*, et al.*, *Diameter dependence of current–voltage characteristics of ultrasmall area AlSb–InAs resonant tunneling diodes with diameters down to 20 nm.* Applied Physics Letters, **70**(15): p. 2025 (1997).

117. S.J. Maddox, W. Sun, Z. Lu, H.P. Nair*, et al.*, *Enhanced low-noise gain from InAs avalanche photodiodes with reduced dark current and background doping.* Applied Physics Letters, **101**(15): p. 151124 (2012).

118. Z. Tian, L. Li, H. Ye, R. Yang, *et al.*, *InAs-based interband cascade lasers with emission wavelength at 10.4 μm.* Electronics Letters, **48**(2): p. 113 (2012).

119. Z. Tian, R.Q. Yang, T.D. Mishima, M.B. Santos, *et al.*, *Plasmon-waveguide interband cascade lasers near 7.5 μm.* IEEE Photonics Technology Letters, **21**(21): p. 1588 (2009).

120. K. Ohtani, K. Fujita, and H. Ohno, *Mid-infrared InAs/AlGaSb superlattice quantum-cascade lasers.* Applied Physics Letters, **87**(21): p. 211113 (2005).

121. R. Teissier, D. Barate, A. Vicet, C. Alibert, *et al.*, *Room temperature operation of InAs/AlSb quantum cascade lasers.* Applied Physics Letters, **85**(2): p. 167 (2004).

122. M. Dallner, S. Hofling, and M. Kamp, *Room-temperature operation of InAs-based interband-cascade-lasers beyond 6 μm.* Electronics Letters, **49**(4): p. 286 (2013).

123. S. Law, D.C. Adams, A.M. Taylor, and D. Wasserman, *Mid-infrared designer metals.* Opt. Express, **20**(11): p. 12155 (2012).

124. R.H. Miwa, R. Miotto, and A.C. Ferraz, *In-rich (4×2) and (2×4) reconstructions of the InAs(001) surface.* Surface Science, **542**(1–2): p. 101 (2003).

125. D.L. Feldwinn, J.B. Clemens, J. Shen, S.R. Bishop, *et al.*, *Anomalous hybridization in the In-rich InAs(001) reconstruction.* Surface Science, **603**(22): p. 3321 (2009).

126. H. Yamaguchi and Y. Horikoshi, *Surface structure transitions on InAs and GaAs (001) surfaces.* Physical Review B, **51**(15): p. 9836 (1995).

127. F. Grosse, W. Barvosa-Carter, J.J. Zinck, and M.F. Gyure, *Microscopic mechanisms of surface phase transitions on InAs(001).* Physical Review B, **66**(7): p. 075321 (2002).

128. W. Barvosa-Carter, R.S. Ross, C. Ratsch, F. Grosse, *et al.*, *Atomic scale structure of InAs(001)-(2×4) steady-state surfaces determined by scanning tunneling microscopy and density functional theory.* Surface Science, **499**(1): p. L129 (2002).

129. G.R. Bell, M. Itoh, T.S. Jones, B.A. Joyce, *et al.*, *Islands and defects on the growing InAs(001)-(2×4) surface.* Surface Science, **433–435**(0): p. 455 (1999).

130. J.B. Babu and K. Yoh, *Evolution of pyramid morphology during InAs(001) homoepitaxy.* Applied Physics Letters, **97**(7): p. 072102 (2010).

131. R. Contreras-Guerrero, S. Wang, M. Edirisooriya, W. Priyantha, *et al.*, *Growth of heterostructures on InAs for high mobility device applications.* Journal of Crystal Growth, **378**: p. 117 (2013).

132. K. Bhatnagar, J. Rojas-Ramirez, M. Caro, R. Contreras, *et al.*, *In-situ monitoring during MBE growth of InAs based heterostructures.* Journal of Crystal Growth, **425**: p. 16 (2015).

133. L.Ö. Olsson, C.B.M. Andersson, M.C. Håkansson, J. Kanski*, et al.*, *Charge Accumulation at InAs Surfaces.* Physical Review Letters, **76**(19): p. 3626 (1996).

134. P.D. Wang, S.N. Holmes, T. Le, R.A. Stradling*, et al.*, *Electrical and magneto-optical of MBE InAs on GaAs.* Semiconductor Science and Technology, **7**(6): p. 767 (1992).

135. R.T. Hinkey, Z. Tian, R.Q. Yang, T.D. Mishima*, et al.*, *Reflectance spectrum of plasmon waveguide interband cascade lasers and observation of the Berreman effect.* Journal of Applied Physics, **110**(4): p. 043113 (2011).

136. J.J.M. Law, A.D. Carter, S. Lee, C.Y. Huang*, et al.*, *Co-doping of InxGa1−xAs with silicon and tellurium for improved ultra-low contact resistance.* Journal of Crystal Growth, **378**: p. 92 (2013).

137. S.H. Lee and G.B. Stringfellow, *Influence of tellurium doping on step bunching of GaAs(001) vicinal surfaces grown by organometallic vapor phase epitaxy.* Applied Physics Letters, **73**(12): p. 1703 (1998).

138. T. Orzali, A. Vert, R.T.P. Lee, A. Norvilas*, et al.*, *Heavily tellurium doped n-type InGaAs grown by MOCVD on 300 mm Si wafers.* Journal of Crystal Growth, **426**: p. 243 (2015).

139. B. Paquette, B. Ilahi, V. Aimez, and R. Arès, *Inhibition of Te surfactant effect on surface morphology of heavily Te-doped GaAs.* Journal of Crystal Growth, **383**: p. 30 (2013).

140. P. Quadbeck, P. Ebert, K. Urban, J. Gebauer*, et al.*, *Effect of dopant atoms on the roughness of III–V semiconductor cleavage surfaces.* Applied Physics Letters, **76**(3): p. 300 (2000).

141. K. Regiński, J. Kaniewski, K. Kosiel, T. Przesławski*, et al.*, *MBE growth and characterization of InAs/GaAs for infrared detectors.* physica status solidi (c), **1**(2): p. 392 (2004).

142. H. Ye, *Optimization of InAs (001) Layers Grown by Molecular Beam Epitaxy*, 2012, University of Oklahoma.

143. K. Ohtani and H. Ohno, *An InAs-based intersubband quantum cascade laser.* Japanese Journal of Applied Physics, **41**: p. L1279 (2002).

144. L.A. Giannuzzi, R. Geurts, and J. Ringnalda, *2 keV Ga+ FIB milling for reducing amorphous damage in silicon.* Microscopy and Microanalysis, **11**(Supplement S02): p. 828 (2005).

145. Z. Tian, Y. Jiang, L. Li, R.T. Hinkey*, et al.*, *InAs-based mid-Infrared interband cascade lasers near 5.3 µm.* IEEE Journal of Quantum Electronics, **48**(7): p. 915 (2012).

146. N.L. Aung, X. Huang, W.O. Charles, N. Yao*, et al.*, *Effect of surface defects on InGaAs/InAlAs Quantum Cascade mesa current–voltage characteristics.* Journal of Crystal Growth, **353**(1): p. 35 (2012).

147. A.S. Bracker, M.J. Yang, B.R. Bennett, J.C. Culbertson, *et al.*, *Surface reconstruction phase diagrams for InAs, AlSb, and GaSb.* Journal of Crystal Growth, **220**: p. 384 (2000).

148. J.R. Meyer, C.A. Hoffman, F.J. Bartoli, and L.R. Ram-Mohan, *Type-II quantum-well lasers for the mid-wavelength infrared.* Applied Physics Letters, **67**(6): p. 757 (1995).

149. R.Q. Yang, *InAs-based quantum cascade lasers with enhanced confinement.* Semiconductor Science and Technology, **30**(10): p. 105023 (2015).

150. M. Zhong, J. Steinshnider, M. Weimer, and R. Kaspi, *Combined x-ray diffraction/scanning tunneling microscopy study of segregation and interfacial bonding in type-II heterostructures.* Journal of Vacuum Science & Technology B, **22**(3): p. 1593 (2004).

151. G.J. Sullivan, A. Ikhlassi, J. Bergman, R.E. DeWames, *et al.*, *Molecular beam epitaxy growth of high quantum efficiency InAs/GaSb superlattice detectors.* Journal of Vacuum Science & Technology B, **23**(3): p. 1144 (2005).

152. H. Kim, Y. Meng, J.-L. Rouviere, D. Isheim, *et al.*, *Atomic resolution mapping of interfacial intermixing and segregation in InAs/GaSb superlattices: A correlative study.* Journal of Applied Physics, **113**(10): p. 103511 (2013).

153. Y. Ashuach, E. Lakin, C. Saguy, Y. Kaufmann, *et al.*, *Atomic intermixing and interface roughness in short-period InAs/GaSb superlattices for infrared photodetectors.* Journal of Applied Physics, **116**(12): p. 124315 (2014).

154. J. Steinshnider, J. Harper, M. Weimer, C.H. Lin, *et al.*, *Origin of antimony segregation in GaInSb/InAs strained-layer superlattices.* Physical Review Letters, **85**(21): p. 4562 (2000).

155. K. Mahalingam, H.J. Haugan, G.J. Brown, and K.G. Eyink, *Quantitative analysis of interfacial strain in InAs/GaSb superlattices by aberration-corrected HRTEM and HAADF-STEM.* Ultramicroscopy, **127**(0): p. 70 (2013).

156. Y. Zhou, J. Chen, Q. Xu, and L. He, *Studies on InAs/GaSb superlattice structural properties by high resolution x-ray diffraction.* Journal of Vacuum Science & Technology B, **30**(5): p. 051203 (2012).

157. N. Bertru, O. Brandt, M. Wassermeier, and K. Ploog, *Growth mode, strain relief, and segregation of (Ga,In)Sb on GaSb(001) grown by molecular beam epitaxy.* Applied Physics Letters, **68**(1): p. 31 (1996).

158. A. Khoshakhlagh, E. Plis, S. Myers, Y.D. Sharma, *et al.*, *Optimization of InAs/GaSb type-II superlattice interfaces for long-wave (~8 μm) infrared detection.* Journal of Crystal Growth, **311**(7): p. 1901 (2009).

159. Y. Wei, W. Ma, Y. Zhang, J. Huang, *et al.*, *High structural quality of type II InAs/GaSb superlattices for very long wavelength infrared detection by interface control.* IEEE Journal of Quantum Electronics, **48**(4): p. 512 (2012).

160. H.J. Haugan, G.J. Brown, and L. Grazulis, *Effect of interfacial formation on the properties of very long wavelength infrared InAs/GaSb superlattices.* Journal of Vacuum Science & Technology B, **29**(3): p. 03C101 (2011).

161. Y. Zhang, W. Ma, Y. Cao, J. Huang*, et al.*, *Long wavelength infrared InAs/GaSb superlattice photodetectors with InSb-like and mixed interfaces.* IEEE Journal of Quantum Electronics, **47**(12): p. 1475 (2011).

162. H. Ye, L. Li, H. Lotfi, L. Lei*, et al.*, *Molecular beam epitaxy of interband cascade structures with InAs/GaSb superlattice absorbers for long-wavelength infrared detection.* Semiconductor Science and Technology, **30**(10): p. 105029 (2015).

163. E. Plis, A. Khoshakhlagh, S. Myers, H.S. Kim*, et al.*, *Molecular beam epitaxy growth and characterization of jour-II InAs/GaSb strained layer superlattices for long-wave infrared detection.* J. Vac. Sci. Technol. B, **28**(3): p. C3G13 (2010).

164. A.Y. Lew, S.L. Zuo, E.T. Yu, and R.H. Miles, *Anisotropy and growth-sequence dependence of atomic-scale interface structure in InAs/$Ga_{1-x}In_xSb$ superlattices.* Applied Physics Letters, **70**(1): p. 75 (1997).

165. P.M. Thibado, B.R. Bennett, M.E. Twigg, B.V. Shanabrook*, et al.*, *Origins of interfacial disorder in GaSb/InAs superlattices.* Applied Physics Letters, **67**(24): p. 3578 (1995).

166. O. Klin, N. Snapi, Y. Cohen, and E. Weiss, *A study of MBE growth-related defects in InAs/GaSb type-II supperlattices for long wavelength infrared detectors.* Journal of Crystal Growth, **425**: p. 54 (2015).

167. R. Kaspi, C. Lu, C. Yang, T.C. Newell*, et al.*, *Desorption mass spectrometry: Revisiting the in-situ calibration technique for mixed group-V alloy MBE growth of ~3.3 μm diode lasers.* Journal of Crystal Growth, **425**: p. 5 (2015).

168. Y. Jiang, L. Li, R.Q. Yang, J.A. Gupta*, et al.*, *Type-I interband cascade lasers near 3.2 μm.* Applied Physics Letters, **106**(4): p. 041117 (2015).

169. J. Nicolai, C. Gatel, B. Warot-Fonrose, R. Teissier*, et al.*, *Elastic strains at interfaces in InAs/AlSb multilayer structures for quantum cascade lasers.* Applied Physics Letters, **104**(3): p. 031907 (2014).

170. R. Weih, M. Kamp, and S. Höfling, *Interband cascade lasers with room temperature threshold current densities below 100 A/cm^2.* Applied Physics Letters, **102**(23) (2013).

171. D. Zuo, P. Qiao, D. Wasserman, and S. Lien Chuang, *Direct observation of minority carrier lifetime improvement in InAs/GaSb type-II superlattice photodiodes via interfacial layer control.* Applied Physics Letters, **102**(14): p. 141107 (2013).

172. E.H. Steenbergen, B.C. Connelly, G.D. Metcalfe, H. Shen*, et al.*, *Significantly improved minority carrier lifetime observed in a long-wavelength infrared III-*

V type-II superlattice comprised of InAs/InAsSb. Applied Physics Letters, **99**(25): p. 251110 (2011).

173. B.V. Olson, E.A. Shaner, J.K. Kim, J.F. Klem*, et al.*, *Time-resolved optical measurements of minority carrier recombination in a mid-wave infrared InAsSb alloy and InAs/InAsSb superlattice.* Applied Physics Letters, **101**(9): p. 092109 (2012).

Appendix: Publication List

1. H. Lotfi, L. Li, L. Lei, H. Ye, S.S. Rassel, Y. Jiang, R.Q. Yang, T.D. Mishima, M.B. Santos, J.A. Gupta, and M.B. Johnson, *High-frequency operation of a mid-infrared interband cascade system at room temperature.* Applied Physics Letters, **108**: p. 201101 (2016).
2. **H. Ye**, L. Li, H. Lotfi, L. Lei, R.Q. Yang, J.C. Keay, T.D. Mishima, M.B. Santos, and M.B. Johnson, *Molecular beam epitaxy of interband cascade structures with InAs/GaSb superlattice absorbers for long-wavelength infrared detection.* Semiconductor Science and Technology, **30**(10): p. 105029 (2015).
3. L. Li, **H. Ye**, Y. Jiang, R.Q. Yang, J.C. Keay, T.D. Mishima, M.B. Santos, and M.B. Johnson, *MBE-grown long-wavelength interband cascade lasers on InAs substrates.* Journal of Crystal Growth, **425**: p. 369 (2015).
4. L. Li, Y. Jiang, **H. Ye**, R.Q. Yang, T.D. Mishima, M.B. Santos, and M.B. Johnson, *Low-threshold InAs-based interband cascade lasers operating at high temperatures.* Applied Physics Letters, **106**(25): p. 251102 (2015).
5. Y. Jiang, L. Li, **H. Ye**, R.Q. Yang, T.D. Mishima, M.B. Santos, M.B. Johnson, D.J.-Y. Feng, and F.-S. Choa, *InAs-based single-mode distributed feedback interband cascade lasers.* IEEE Journal of Quantum Electronics, **51**(9): p. 1 (2015).
6. Y. Jiang, L. Li, **H. Ye**, R. Yang, T.D. Mishima, M.B. Santos, and M.B. Johnson. *Continuous-wave operation of InAs-based interband cascade lasers above room temperature*. in *CLEO: QELS_Fundamental Science*. Optical Society of America, p. JTh5A. 8 (2015).
7. R.S. Dhar, L. Li, **H. Ye**, S.G. Razavipour, X. Wang, R.Q. Yang, and D. Ban, *Nanoscopically resolved dynamic charge-carrier distribution in operating interband cascade lasers.* Laser & Photonics Reviews, **9**(2): p. 224 (2015).
8. **H. Ye**, H. Lotfi, L. Li, R.T. Hinkey, R.Q. Yang, L. Lei, J.C. Keay, M.B. Johnson, T.D. Mıshıma, and M.B. Santos, *Multistage interband cascade photovoltaic devices with a bandgap of 0.23 eV operating above room temperature.* Chinese Science Bulletin, **59**(10): p. 950 (2014).
9. H. Lotfi, L. Li, **H. Ye**, R.T. Hinkey, L. Lei, R.Q. Yang, J.C. Keay, T.D. Mishima, M.B. Santos, and M.B. Johnson, *Interband cascade infrared photodetectors with long and very-long cutoff wavelengths.* Infrared Physics & Technology, **70**: p. 162 (2014).
10. Y. Jiang, L. Li, Z. Tian, **H. Ye**, L. Zhao, R.Q. Yang, T.D. Mishima, M.B. Santos, M.B. Johnson, and K. Mansour, *Electrically widely tunable interband cascade lasers.* Journal of Applied Physics, **115**(11): p. 113101 (2014).
11. R.S. Dhar, C. Xu, D. Ban, L. Li, **H. Ye**, R. Yang, M.B. Johnson, T.D. Mishima, and M. Santos. *Direct observation of non-uniform electric field in the active regions of an interband cascade laser*. in *CLEO: Science and Innovations*. Optical Society of America, p. STh3G. 3 (2014).

12. **H. Ye**, L. Li, R.T. Hinkey, R.Q. Yang, T.D. Mishima, J.C. Keay, M.B. Santos, and M.B. Johnson, *MBE growth optimization of InAs (001) homoepitaxy.* Journal of Vacuum Science & Technology B, **31**(3): p. 03C135 (2013).

13. R.Q. Yang, H. Lotfi, L. Li, R.T. Hinkey, **H. Ye**, J.F. Klem, L. Lei, T. Mishima, J. Keay, and M. Santos. *Quantum-engineered interband cascade photovoltaic devices*. in *SPIE OPTO*. International Society for Optics and Photonics, p. 899310 (2013).

14. R.Q. Yang, L. Li, L. Zhao, Y. Jiang, Z. Tian, **H. Ye**, R. Hinkey, C. Niu, T.D. Mishima, and M.B. Santos. *Recent progress in development of InAs-based interband cascade lasers*. in *SPIE OPTO*. International Society for Optics and Photonics, p. 86400Q (2013).

15. J.F. Klem, R.Q. Yang, H. Lotfi, L. Li, R.T. Hinkey, **H. Ye**, L. Lie, T. Mishima, J. Keay, and M. Santos. *Quantum-engineered interband cascade photovoltaic devices*. in *Proceedings of SPIE*. Sandia National Laboratories (SNL-NM), Albuquerque, NM (United States), p. 493198 (2013).

16. R.T. Hinkey, H. Lotfi, L. Li, **H. Ye**, L. Lei, R.Q. Yang, J.C. Keay, T.D. Mishima, M.B. Santos, and M.B. Johnson. *Interband cascade infrared photodetectors with InAs/GaSb superlattice absorbers*. in *SPIE Optical Engineering+Applications*. International Society for Optics and Photonics, p. 886805 (2013).

17. Z. Tian, L. Li, **H. Ye**, R. Yang, T. Mishima, M. Santos, and M. Johnson, *InAs-based interband cascade lasers with emission wavelength at 10.4 µm.* Electronics Letters, **48**(2): p. 113 (2012).

18. L. Li, Z. Tian, Y. Jiang, **H. Ye**, R.Q. Yang, T.D. Mishima, M.B. Santos, and M.B. Johnson. *Interband cascade lasers at long wavelengths*. in *CLEO: Science and Innovations*. Optical Society of America, p. CF3K. 2 (2012).